



RAMAN RESEARCH INSTITUTE

ASTRONOMY & ASTROPHYSICS GROUP

Ph.D. Dissertation

PROBING THE PHYSICAL MECHANISMS
OF HIGH ENERGY EMISSION FROM BL LACS
WITH MULTI-WAVELENGTH DATA ANALYSIS
AND MODELING

Sandeep Kumar Mondal 

Research Fellow, A&A – RRI
Supervisor: Prof. Nayantara Gupta
Bengaluru 560080, India

April 2024

Thesis Submitted
for the degree of
Doctor of Philosophy



Jawaharlal Nehru University
New Delhi 110067, India

Declaration

I, *Sandeep Kumar Mondal* (Enrolment No.: RRI/18/004), declare that the work reported in this thesis titled '*Probing the Physical Mechanisms of High Energy Emission from BL Lacs with Multi-Wavelength Data Analysis and Modeling*', is entirely original. This thesis is composed independently by me at *Raman Research Institute (RRI)* under the supervision of *Prof. Nayantara Gupta* and is the result of my own work unless otherwise stated. I further declare that the subject matter presented in this thesis has not previously formed the basis for the award of any degree, diploma, membership, associateship, fellowship or any other similar title of any university or institution. I also declare, this thesis has been checked through the plagiarism software DrillBit.

Nayantara Gupta

Signature of Supervisor

Prof. Nayantara Gupta

Professor, RRI

Sandeep Kumar Mondal

Signature of Candidate

Sandeep Kumar Mondal

Research Fellow, RRI

Astronomy & Astrophysics Group

Raman Research Institute (RRI)

Bangalore- 560080

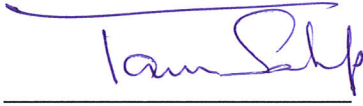
Karnataka, India

Date: *15/04/24*

Place: *Bangalore*

Certificate

This is to certify that the work contained in the thesis titled '*Probing the Physical Mechanisms of High Energy Emission from BL Lacs with Multi-Wavelength Data Analysis and Modeling*', submitted by *Sandeep Kumar Mondal* (Enrolment No.: RRI/18/004) to the Jawaharlal Nehru University for the award of the degree of *Doctor of Philosophy (Ph.D.)* in Physical Sciences, is the bonafide record of original research work carried out by the candidate from August 2018 — April 2024, under my guidance and supervision at Raman Research Institute (RRI), Bengaluru, India. The results embodied in the thesis have not been submitted to any other University or Institute for the award of any degree or diploma.



Signature of Director

Prof. Tarun Souradeep

Director & Professor, RRI



Signature of Supervisor

Prof. Nayantara Gupta

Professor, RRI

Astronomy & Astrophysics Group

Raman Research Institute (RRI)

Bangalore-560080

Karnataka, India

Date: 15.4.2024

Place: Bengaluru

Acknowledgements

Writing this part of the thesis feels tougher than drafting any other section. Along my journey, I've crossed paths with so many incredible individuals, each leaving their mark on me and shaping who I am today. Undoubtedly, this small part of my thesis is inadequate to express gratitude to everyone. My heartfelt gratitude to all of them who have crossed my path and enriched me in all aspects, whether academic or non-academic. While I can't possibly name everyone, I would like to mention a few of them without whom my journey to this point would be incomplete. And if I happen to overlook anyone, please know it's unintentional, and my gratitude extends to all who've touched my life.

I extend my sincere gratitude to Prof. Nayantara Gupta, my PhD supervisor, for her invaluable guidance and unwavering support. She has given me complete freedom to work, which in turn has taught me self-reliance and enhanced my problem-solving abilities. Also, her encouragement and moral support have given me the confidence to learn things on my own and given me ample time to rectify my mistakes. I am truly grateful for her insightful feedback, which has played a key role in shaping the direction of my research and refining my scholarly abilities.

I cannot express enough gratitude to my senior, collaborator, groupmate, blockmate, and dear friend Dr. Saikat Das (Saikat da), for his unconditional support and guidance in my personal and professional life. He plays a major role in shaping my understanding from the most basic concepts to the complexities of my field.

I thank my other collaborators, Dr. Avik Kumar Das (Avik da) and Dr. Raj Prince (Raj), for their academic guidance, which played a pivotal role in learning different skills during my Ph.D. journey.

I wish to express my gratitude to my advisory committee members, Dr. Nirupam Roy and Prof. Andal Narayanan, for their invaluable guidance and support.

Since I joined RRI, the library and its people have held a special place in my heart. RRI library was the place where I spent most of the time during my Ph.D. life. I always admire the peaceful atmosphere, the vast collection of books, and the wonderful facilities of the library. I express my deep gratitude to Manju (KP), Manjunath sir, and Nagaraj Sir for their relentless effort in the maintenance and development of the library.

My Ph.D. heavily relied on computation, and I wholeheartedly thank the RRI IT & Computing section for their invaluable support.

I want to express my sincere thanks to the rest of my past and present group members: Agnibha, Sovan (Boxi), Gunjan, and Aditi, for their support. I also thank my colleagues Anirban, Hemanth, Sanhita di, Tanuman da, and Naren da for their welcoming attitude toward any academic discussion, which helped me nurture and broaden my knowledge in X-ray astronomy and radio astronomy. I want to thank Sayari and Sukanya for their valuable input on my thesis.

I extend my sincere gratitude to the RRI Administration, the departmental secretaries of the Astronomy & Astrophysics group (Harini, Mamtha Bai, & Mahima), the E&B department, the Security & Transport department, and the canteen staff for their invaluable support in ensuring the smooth operation of everything.

I thank my sister, Dwipanwita and my friend & colleague, Sukanya, for making time to proofread my thesis.

I am deeply thankful to Mangalaji and her team for their delicious and nutritious meals, which give a homely feeling.

The guidance of seniors has always played a crucial role in my student life, and it was no exception at RRI. I extend my gratitude to all my seniors, especially Ranita di, Dipak da, Swarnak da, Bapan da, Sukh Veer, Mandira di, and Maheswar da, for their guidance and support.

I extend my sincere appreciation to all my seniors, my friends (Ion, Gokul, Shreya, Bidyut, Abhishek (Sadhu), Gunjan, Manami, Ashwin, Sukanya, Sachidananda, Sourav (Bhadra)) and my fellow juniors (Abhishek (Ghadai), Deepak, Makarand, Vaibhav, Manish, Mukesh, Gourab, Pooja, Sayari, Kinjal, Maitri, Punit, Sayantan, Jasim, Sonali, Soumen, Sovon (Boxi), Vijay, Abhisek (Tamang), Aman, Dipanshu, Raghuveer) who have been a significant part of my life beyond academic pursuits, whether through shared experiences in travel, sports, singing, games, or other activities. I am grateful for the memories we have created together and the friendship you have shown me throughout our shared adventures.

I express my deepest gratitude to my alma mater, Jadavpur University (JU), and to my beloved friends and seniors from JU. I am immensely thankful to Sourav, Mita, Moumita

(Halder), Samata, Arindam da, Jhulik di, and Sumit da for their unwavering support and boundless love. Additionally, I would like to thank my childhood friends Abhishikta, Moumita (Roy), and Dibyendu for their enduring support and affection.

I want to express my sincere thanks to all my teachers whose kind efforts have helped me grow into what I am today, especially Alok sir, Mrinal sir, and Babu sir. In particular, I want to extend my deepest thanks to my physics teacher, Dr. Pradip Kumar Jana, whose exceptional teaching skills made me fall in love with physics.

My heart is forever filled with gratitude for my cousin, Barnali di (Bono di), whose enduring love and pride continue to inspire me, even though she's no longer with us.

Finally, I want to express my heartfelt gratitude to my family for their continuous support throughout this journey. My mother taught me resilience, never to lose hope and always keep fighting; my father taught me honesty and integrity and to always follow my passion with dedication; and my sister has been a source of strength, teaching me how to keep composure in difficult situations and remain focused towards the objectives. I am deeply grateful for their unconditional support, which has been pivotal to my growth and development.

বাবা, মা, বোন
ও
পরিবারকে

Contents

Abstract	xvii
List of Publications	xxi
List of Figures	xxvi
List of Tables	xxvii
1 Introduction	1
1.1 Introduction	1
1.1.1 History of AGN	2
1.1.2 Classification of AGN	4
1.1.3 Components of AGN	9
1.1.4 AGN Unification	11
1.1.5 Study of BL Lacs:	12
1.1.6 Motivation to study BL Lacs:	18
1.1.7 Overview	19
2 Multi-wavelength Observation: Data Analysis & Reduction	21
2.1 Fermi Gamma-Ray Telescope:	21
2.1.1 Introduction:	21
2.1.2 About the Instrument:	21
2.1.3 Gamma-ray detection method:	22
2.1.4 Raw data reduction:	23
2.2 Neil Gehrels Swift observatory	23
2.3 XMM-Newton	25
2.4 Publicly Available Archival Data:	26
2.4.1 MAGIC Data:	26
2.4.2 MOJAVE Data:	26
2.4.3 ATCA Data:	26

3 Spectral Modeling of Flares in Long Term Gamma-Ray Light Curve of PKS 0903-57	27
3.1 Introduction	27
3.2 Data Analysis	29
3.2.1 Fermi-LAT Data Analysis	29
3.2.2 Swift XRT and UVOT Data Analysis	32
3.3 Flaring States of PKS 0903-57	33
3.4 Method of Identification of Different Activity Phases & Temporal Evolution of Gamma-Ray Light Curve during the Flares	34
3.4.1 Detection of Different Activity Phases	34
3.4.2 Study of Temporal Evolution of the γ -ray Flares	36
3.5 Description of Flares	37
3.5.1 Flare-1	37
3.5.2 Flare-2	38
3.5.3 Variability Time	42
3.6 Gamma- Ray Spectral Energy Distribution of different flaring phases	44
3.7 Multi-Wavelength Study of PKS 0903-57	50
3.7.1 Multi-Wavelength Light Curve of PKS 0903-57	51
3.7.2 Multi-Wavelength SED Modeling	52
3.7.3 Physical Constraint for Multi-Wavelength SED Modeling	53
3.7.4 Modeling the SEDs	53
3.8 Summary and Discussion	55
3.9 Conclusion	58
4 Exploring the Emission Mechanisms of Mrk 180 with long term X-ray and γ-ray data	61
4.1 Introduction	61
4.2 Data Analysis	62
4.2.1 Fermi-LAT Data Analysis	62
4.2.2 SWIFT XRT and UVOT Data Analysis	63
4.2.3 XMM-Newton X-ray Data Analysis	64
4.2.4 MOJAVE Data	64
4.2.5 MAGIC Data	64

4.2.6	Archival Data	65
4.3	Fermi-LAT gamma-Ray Light curve Analysis	65
4.4	Multi-Wavelength SED Modeling	65
4.4.1	Leptonic Modeling	66
4.4.2	UHECR interactions	67
4.4.3	pp interactions	68
4.4.4	Jet Power	68
4.5	Results	69
4.5.1	UHECRs from Mrk 180	73
4.6	Discussions	75
4.7	Conclusion	77
5	Summary & Future Prospect	79
5.1	Summary & Future Prospect	79
5.1.1	Thesis Summary	79
5.1.2	Future Prospect	82
	References	87

Introduction:

Active Galactic Nucleus (AGN) is the central core of an active galaxy, which is much brighter than its host galaxy that outshines the entire galaxy ([1]). AGNs are some of the most prominent sources of high-energy γ -rays. It is thought that at the centre of an active galaxy there is a super-massive black hole (SMBH), which accretes matter and forms an accretion disk around the core. AGN emits jet along its polar direction i.e. perpendicular to its accretion disk, which are collimated, narrow beams of highly relativistic particles. The jet transports energy and momentum over large distances.

Depending on the orientations of the jets of AGNs with respect to the observer's line of sight, AGNs have been classified into several classes. If the jet is oriented close to the line of sight of the observer ([1]) then it is called a blazar. Moreover, blazars have two sub-classes: flat-spectrum radio quasars (FSRQs) and BL Lacertae (BL Lac). FSRQs show characteristic spectral lines whereas BL Lacs show featureless continuum spectra or very weak spectral lines. Blazars show high flux variability; their variability time varies from minutes ([2]) to year ([3]) scale across the whole electromagnetic spectrum. Their emission is highly polarized and of non-thermal origin. The broadband spectrum energy distribution (SED) of a blazar covers the entire electromagnetic spectrum, ranging from radio to very high-energy (VHE, $E \gtrsim 30$ GeV) γ -rays. It exhibits two peak emission frequencies. The low-energy peak occurs between radio and soft X-ray energies and can be attributed to synchrotron radiation from a relativistic electron and positron population. The high-energy peak between X-ray and VHE γ -ray energies can arise from various processes. The most prevalent explanation is the inverse Compton scattering of synchrotron photons (synchrotron self-Compton, SSC) or external photons originating from the broad-line region (BLR), the dusty torus (DT), or the accretion disk (AD). In addition, the VHE γ -rays can also come from photo-hadronic ($p\gamma$) or hadronuclear (pp) interactions of accelerated cosmic rays with the ambient radiation or matter in the emission region of the jet or proton synchrotron radiation ([4–6]). They are also found to be the sources of high-energy γ -rays in the universe.

The mechanisms of particle acceleration in jet, the magnetic field structure in jet, the underlying causes of variability in jet emission over short and long time scales are not yet well understood. Multi-wavelength data analysis and modeling of jet

emission are necessary to understand the physics of these objects.

We have studied the temporal and spectral characteristics of two BL Lac sources to understand the underlying physical mechanism in this object using multi-wavelength data.

- **Spectral Modeling of Flares in Long-term Gamma-Ray Light Curve of PKS 0903-57:**

Here, we did a detailed study of a BL Lacertae object, PKS 0903-57, for the first time with 12 year of Fermi Large Area Telescope (Fermi-LAT) data. This source was listed in Fermi's regularly monitored source list and monitored continuously since 2008 August. In 2020, high flaring activity from this source has been detected by different telescopes in different wave bands. Such activity has also been reported before, e.g., in 2015 and 2018;. We have analyzed a 7 day binned γ -ray light curve over the 12 year, which does not show any significant activity around 2015. From that long-term γ -ray light curve, we have identified two bright γ -ray flares in 2018 and 2020. Many substructures were observed during multiple time binning of these flares. We performed a detailed temporal and spectral study on all the substructures separately. The γ -ray SEDs of the substructures have been fitted with Power-Law, Log-Parabola, Broken Power-Law, and Power-Law Exponential Cutoff to find the best-fitted spectral model. We have also calculated the shortest variability time in the γ -ray, which is found to be 1.7 ± 0.9 hr. We have studied the rise time (T_r) and decay time (T_d) by fitting the γ -ray light curve of the flaring phases to check whether they follow any trend or not. Using the available simultaneous multi wavelength data from Swift-XRT, Swift-UVOT, and ATCA, for the four flaring phases, we have constructed the multi-wavelength SEDs. We modeled the multi-wavelength SEDs of these four flaring phases. A single-zone emission model is used for time-dependent leptonic modeling of the four multi-wavelength SEDs. Our estimated values of the magnetic field in the emission region, and the jet power obtained from leptonic modeling of PKS 0903-57 are presented in this work.

- **Exploring the Emission Mechanisms of Mrk 180 with Long-term X-Ray and γ -Ray Data:**

In this work, we have studied a BL Lac object, Markarian (Mrk) 180, located at a redshift of 0.045, which is a potential candidate for high-energy cosmic ray acceleration. For the temporal study, we have analyzed the Fermi-LAT

γ -ray data of Mrk 180 collected over a period of 12.8 years. No γ -ray flux enhancement has been found from this long-term light curve; also the error bars of the high-energy γ -ray data points are too large to carry out a detailed temporal study on this source. To know about the physical processes, we studied the long-term SED of Mrk 180. We analyzed Swift X-ray, ultraviolet & optical, and X-ray Multi-Mirror Mission (XMM-Newton) data to construct the multi-wavelength SED. The SED has been modeled with one-zone pure leptonic and lepto-hadronic scenarios to understand the physical processes that can explain the HBL nature of this source. The pure leptonic model and the two lepto-hadronic models, viz., (i) line-of-sight interactions of ultrahigh-energy cosmic rays (UHECR; $E \gtrsim 10^{17}$ eV) with the cosmic background radiation and (ii) the interactions of relativistic protons with the cold protons in the jet, have been compared in our work. It is found that the pp interaction model is found to give a better fit to the multi-wavelength data than the other two models. Moreover, an earlier study has associated Mrk 180 with the Telescope Array (TA) hotspot of UHECRs at $E > 57$ EeV. This speculation motivates us to check whether ultrahigh energy protons and iron nuclei can reach the earth from Mrk 180. After comparing the results of our simulation with the current observational data, we find that Mrk 180 is unlikely to be a source of the UHECR events contributing to the TA hotspot for conservative strengths of extragalactic magnetic fields.

Summary and Future Prospects:

We have studied two BL Lac objects using multi-wavelength data to understand the underlying physical mechanism of those objects.

For PKS 0903-57, we identified two bright γ -ray flares in 2018 and 2020. Thereafter, we performed a detailed temporal and spectral study on these two flaring events. We fitted the γ -ray SEDs with four different models and it has been found that in most cases the γ -ray SEDs of different phases can be well described by the Log-Parabola model. To explore any trend in the γ -ray light curve, we fitted them with a sum of exponential function and calculated the rise (T_r) and decay (T_d) timings of the flares and found no particular pattern for this source. We modeled the multi-wavelength SEDs of four flaring phases with one-zone leptonic model where we considered a spherical emission region within the blazar jet; but the data was not sufficient for better understanding of the physical processes occurring in this source. Further simultaneous multi-wavelength monitoring of this source is required for further detail study of this source.

For Mrk 180, we could not carry out any detail temporal study due to large error

bars of the high-energy γ -ray data points also we did not find any flux enhancement in the γ -ray waveband. To know about the physical processes, we studied long-term multi-wavelength SED of Mrk 180. We considered a single-zone spherical emission region within the jet. Our study showed that a single-zone pure leptonic model could not explain the multi-wavelength SED of Mrk 180. So, we considered single-zone lepto-hadronic models to obtain better fits to the data. The residuals of the three models are compared and the pp interaction model is found to give a better fit to the multi-wavelength data than the other two models. More observational data covering the radio to VHE γ -ray frequencies would be useful for exploring the emission mechanisms of Mrk 180 and to give a definitive conclusion. We also checked the association of Mrk 180 with the Telescope Array (TA) hotspot of UHECRs at $E > 57$ EeV ([7]). From our study, it can be seen that for optimistic magnetic field values considered, the contribution of this source to the TA hotspot is disfavored unless very high magnetic fields $B_{rms} \sim 1$ nG or higher are considered. Thus, Mrk 180 may not be a plausible UHECR source for explaining the TA hotspot.

For better understanding of the physical processes in blazars, more simultaneous data would be helpful. Future observatories like Large High Altitude Air Shower Observatory (LHAASO; [8]), Cherenkov Telescope Array (CTA), High Energy cosmic Radiation Detection facility (HERD), IceCube-Gen2, Giant Radio Array for Neutrino Detection (GRAND), Baikal-GVD, Cubic Kilometer Neutrino Telescope (KM3NeT), Pacific Ocean Neutrino Experiment (P-ONE; [9]) can provide the information about gamma-rays, cosmic rays and neutrinos for multi-messenger astronomy. Data from these observatories will be helpful to decipher the unexplored or unanswered questions about blazars.

List of Publications

1. *Spectral Modeling of Flares in Long-term Gamma-Ray Light Curve of PKS 0903-57*
Sandeep Kumar Mondal, Raj Prince, Nayantara Gupta, Avik Kumar Das
The Astrophysical Journal **922**, 160 (2021) [[arXiv:2107.02702](#)]
2. *Exploring the Emission Mechanisms of Mrk 180 with long term X-ray and gamma-ray data*
Sandeep Kumar Mondal, Saikat Das, Nayantara Gupta
The Astrophysical Journal **948**, 75 (2023) [[arXiv:2212.07331](#)]

(B) Co-author

3. *Gamma-ray flares and broadband spectral study of PKS 0402-362*
Avik Kumar Das, **Sandeep Kumar Mondal**, Raj Prince
Monthly Notices of the Royal Astronomical Society, stad702 [[arXiv:2303.03039](#)]

(C) Conference Proceedings

4. *Unraveling the Emission Mechanism of the HBL Source Mrk 180 with Multi-Wavelength Data*
Sandeep Kumar Mondal, Saikat Das, Nayantara Gupta
Proceedings of Science **942**, (2023) [[arXiv:2308.16489](#)]

List of Figures

1.1	One of the latest photographs of M87 or NGC 4486 and its jet. (photographed by Hubble Telescope; M87).	2
1.2	Tree chart of AGN classification (Image Credit: Fig. 3 from Tadhunter [19]). Type-3: Lower luminosity AGN; Type-0: AGN shows rapid variability in optical waveband.	4
1.3	The traditional Fanaroff Riley classification of radio galaxies [24]. FR-I galaxies are “centre-bright”, and FR-II galaxies are “edge-brightened” (often with “hotspots” towards the edge).	6
1.4	Multiwavelength SED of Mrk 180. (Image Credit: Mondal et. al, 2023)	7
1.5	A schematic diagram of Accretion Disk around a Black Hole. (Image Credit: Heino Falcke, Lecture notes on “Standard Accretion Disks”, Page 1.)	9
1.6	(1.6a) Schematic representation of the central structure of an AGN. (Image credit: Doré et al. [49]). (1.6b) AGN SED. (Image Credit: Padovani [50]).	10
1.7	(1.7a) Unified model of AGN adapted from Urry and Padovani [1]. The thick arrows represent different viewing angles and the observed object which results from them. (1.7b) Schematic diagram of AGN.	12
1.8	SED of FSRQ, LBL, and HBL (dotted lines). In general, FSRQ and LBL (dashed lines) are more luminous than HBL (dotted lines), so the wavelength of the peak power output correlates with luminosity. (Image Credit: Urry, Caltech)	14
2.1	(2.1a) Structure of LAT (Image Credit: Fermi-LAT Website). (2.1b) Schematic structure of Fermi-LAT (Image Credit: Geant4 Simulation of High Energy Gamma Ray Experiments)	22
3.1	12 years (MJD 54682.0-59220.0) γ -ray light curve of PKS 0903-57 in 7-day binning. Two flaring states Flare-1 & Flare-2 have been identified and highlighted with a pair of vertical red-dotted lines.	34
3.2	‘Flare’ detection with the help of Bayesian Block method during ‘Flare-1’.	35

3.3	'Flare' detection with the help of Bayesian Block method during 'Flare-2'.	35
3.4	γ -ray light curve of PKS 0903-57 during Flare-1 (MJD 58216.5-58230.0) shown in Figure 3.1 . In smaller time binning the different phases of Flare-1 are more prominent. Flare-1 has two phases: Flare-1A & Flare-1B.	37
3.5	Fitted light curve with Equation 3.2 of Flare-1A (MJD 58217.5-58220.0)	38
3.6	Fitted light curve with Equation 3.2 of Flare-1B (MJD 58220.9-58225.3)	38
3.7	γ -ray light curve of PKS 0903-57 during Flare-2 (MJD 58920.0-58976.0). Two sub-structures of Flare-2: Flare-I & Flare-II.	39
3.8	γ -ray light curve of PKS 0903-57 during Flare-I (MJD 58920.0-58961.3), sub-structure of Flare-2 shown in Figure 3.7 . Five phases of Flare-I: Preflare-I, Flare-IA, Flare-IB, Flare-IC & Postflare-I. . . .	39
3.9	γ -ray light curve of PKS 0903-57 during Flare-II (MJD 58961.3-58976.0), sub-structure of Flare-2 shown in Figure 3.7 . Three phases of Flare-II: Preflare-II, Flare-II & Postflare-II.	40
3.10	Fitted light curve with Equation 3.2 of Flare-IA (MJD 58932.5-58941.7)	40
3.11	Fitted light curve with Equation 3.2 of Flare-IB (MJD 58941.7-58947.0)	40
3.12	Fitted light curve with Equation 3.2 of Flare-IC (MJD 58947.0-58957.6)	41
3.13	Fitted light curve with Equation 3.2 of Flare-II (MJD 58962.0-58965.0)	41
3.14	γ -ray SEDs during Flare-1A & Flare-1B of Flare-1 as shown in Figure 3.4 . PowerLaw (PL), LogParabola (LP), BrokenPowerLaw (BPL) and PowerLaw with Exponential Cutoff (PLEC) models used to fit the γ -ray data points.	45
3.15	γ -ray SEDs of five activity phases of Flare-I as shown in Figure 3.8 . SEDs have been fitted with four spectral models mentioned earlier.	46
3.16	γ -ray SEDs of three activity phases of Flare-II as shown in Figure 3.9 . SEDs have been fitted with the four spectral models mentioned earlier.	47
3.17	Multi-Wavelength light curve of PKS 0903-57 during Flare-1. The 'green solid circle' denotes Fermi-LAT data points in 6-hour bin. Others are mentioned in the plots. Ultra-Violet data points are in W1, M2 & W2 bands and Optical data points are in U, V & B bands.	51
3.18	Multi-Wavelength light curve of PKS 0903-57 during Flare-I. Color codes are same as Figure 3.17	52

3.19	Multi-Wavelength SED of Flare-1B. Following are the color codes: 'Grey Square' = Archival data points/ Non-simultaneous data points; 'Red Solid Circle' = Optical (Swift); 'Cyan Triangle' = Ultra-Violet (Swift); 'Green Triangle' = X-ray (Swift); 'Magenta Solid Circle' = γ -Ray (Fermi-LAT).	59
3.20	Multi-Wavelength SED of Flare-IA. The color codes are similar to Figure 3.19 , radio data points denoted by 'Blue inverted-Triangle' (ATCA).	59
3.21	Multi-Wavelength SED of Flare-IB. The color codes are same as Figure 3.19	60
3.22	Multi-Wavelength SED of Flare-IC. The color codes are same as Figure 3.19	60
4.1	Application of Bayesian Block Method on Fermi-LAT γ -Ray Data of Mrk 180 (MJD 54682.65- 59355.67)	65
4.2	Pure leptonic modeling of the multiwavelength SED of Mrk 180 and residual plot corresponding to this modeling. The data color codes are mentioned in the plots.	71
4.3	Distribution of propagated UHECRs as a function of deflection angle in a random turbulent magnetic field.	72
4.4	Leptonic+hadronic (UHECR) modeling of the multiwavelength SED of Mrk 180 and residual plot corresponding to this modeling.	73
4.5	Leptonic+hadronic (pp) modeling of the multiwavelength SED of Mrk 180 and residual plot corresponding to this modeling; the gray shaded region denotes the difference between the attenuated and unattenuated regions of the total SED.	74
4.6	Arrival direction of UHECRs at $E > 57$ EeV from Mrk 180 to Earth. The blue line shows the Galactic plane. The purple point and the purple dotted curve show the TA hotspot center and the 20° region around it. Similarly, the green dotted curve shows the 20° region around Mrk 180. The color bar indicates the energy per nucleon (E/z) of the observed events. From left, the figures correspond to (a) pure proton injection and $B_{\text{rms}} \approx 10^{-3}$ nG; (b) pure proton injection and $B_{\text{rms}} \approx 10^{-5}$ nG; (c) Fe injection and $B_{\text{rms}} \approx 10^{-5}$ nG	76
5.1	(5.1a) Sensitivity plot of different X-ray and gamma-ray instruments (Image Credit: Lucchetta <i>et al.</i> [234]). (5.1b) Projected sensitivities of future neutrino telescopes (All-flavor cosmogenic neutrino flux above PeV energies.) (Image Credit: Huang <i>et al.</i> [235]).	83

5.2	Follow-up observation of IceCube alert IC170922. (Image Courtesy: National Science Foundation (link))	84
-----	---	----

List of Tables

3.1	Table for SWIFT XRT/UVOT observations, used in this paper . . .	33
3.2	Table of average γ -ray flux of different activity states of PKS 0903-57	36
3.3	Table of Rise & Decay time for Flare-1A	38
3.4	Table of Rise & Decay Time for Flare-1B	38
3.5	Table of Rise & Decay Time for Flare-1A	41
3.6	Table of Rise & Decay Time for Flare-1B	42
3.7	Table of Rise & Decay Time for Flare-1C	42
3.8	Table of Rise & Decay Time for Flare-1I	42
3.9	Table for γ -ray flux doubling/halving time ($T_{d/h}$) for each flare . . .	43
3.10	Results of Fermi-LAT SEDs of Flare-1, fitted with different spectral model e.g. PL, LP, BPL and PLEC	48
3.11	Results of Fermi-LAT SEDs of Flare-I, fitted with different spectral model e.g. PL, LP, BPL and PLEC	49
3.12	Results of Fermi-LAT SEDs of Flare-II, fitted with different spectral model e.g. PL, LP, BPL, PLEC	50
3.13	Results of multi-wavelength SED modeling shown in the Figure 3.19 to Figure 3.22	56
3.14	Table for total jet power for each flaring event	56
4.1	Results of multi-wavelength SED modeling shown in the Figure 4.2 , Figure 4.4 , and Figure 4.5	75

1.1 Introduction

Humans have always been curious about Nature. This curiosity has propelled the human race to reach its present state. In ancient eras, people were astonished by every natural phenomenon. Humans neither have any technical support nor any prior information like today, so anything observable piqued their curiosity, from flickering fire to the little twinkling dots in the dark sky or the big bright light in the sky. Historical references, e.g. ancient cave paintings and artefacts, provide evidence of their innate curiosity about the night sky and celestial bodies, which they only observed in the Stone Age. As time passed, people could understand the celestial phenomena, develop instruments and gather theoretical knowledge. This was the moment when people became interested in scientific explanations and predictions of celestial events rather than only observation. As knowledge increased, so did the curiosity to know more, leading the human beings to further quench their thirst for the unknown. This can be seen through the contribution of Mesopotamian, Egyptian, and Greek civilizations to astronomy. Astronomy further flourished between the 8th and 15th centuries during the Islamic age [10] under the astronomers Al-Battani, Al-Biruni, and Ibn al-Haytham, Ulugh Beg. Around the same period, Indian astronomers Aryabhata, Varahamihira, and Bhaskaracharya (also known as Bhaskara II) made significant contributions to astronomy. After this, the Renaissance and Industrial Revolution began a new era in astronomy under the guidance of famous astronomers Copernicus, Galileo, and Kepler. Besides rigorous observation, scientists developed new theories to explain astronomical phenomena. Slowly, astrophysics emerged as a new subject where scientists mainly focused on the physics, related to astronomical objects or events. As time progresses, the questions we ask and the methods we employ evolve. Now, we are curious to know beyond our solar system even beyond our own Milky Way and so on. Scientific and technological developments in radio and X-ray physics have opened up multi-wavelength observation, which unravels another picture of our Universe. Highly sophisticated ground-based telescopes and space-based observatories have been developed, enabling scientists to detect extragalactic objects across the electromagnetic spectrum. Active Galactic Nuclei or AGN is one such extragalactic object, first detected in the 20th century. Even

today, in the 21st century, there are so many open questions about AGN. In this thesis, I will provide a brief introduction to AGN, followed by an exploration of two of our works related to understanding these objects.

1.1.1 History of AGN

AGN was discovered at the beginning of the 20th century. The first spectroscopic detection from an AGN was reported by Edward Arthur Fath in 1908 at Lick Observatory [11]. The detected broad emission lines from the nebula NGC 1068 were strong and different from the usual absorption spectra of normal galaxies. In 1918, Heber Doust Curtis studied 762 nebulae photographed with Crossley reflector at the Lick Observatory. He detected a jet-like structure from the centre of M87 or NGC 4486, which he called a “curious straight ray” [12].

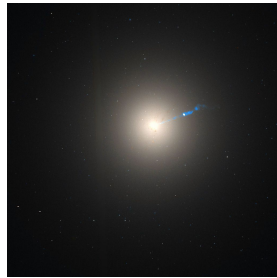


Figure 1.1. One of the latest photographs of M87 or NGC 4486 and its jet. (photographed by Hubble Telescope; [M87](#)).

Before these, in 1900, Vesto Melvin Slipher, an American astronomer, detected large redshifts in some galaxies. Later, in 1943, Carl Seyfert observed bright nuclei and strong, broad emission lines in the optical spectra of six spiral galaxies, now known as the ‘Seyfert Galaxy’, a class of AGN [13].

On the other side, radio astronomy began to flourish at the same time. In 1930, an engineer at Bell Telephone Laboratories named Karl Jansky discovered radio signals from the Milky Way. Over the next 20 years, there were huge technological advancements in radio astronomy, and World War II greatly impacted this development. Two separate radio surveys were conducted in the 1950s. One was by Martin Ryle and his colleague at Cavendish Lab, known as Cambridge Northern Cross Survey, and the other was by John Bolton and his colleagues at Parkes Observatory, which led to the discovery of many new celestial objects. Around 1959 - 1960, the Third Cambridge Catalogue (3C) of radio sources was published, containing radio-emitting sources.

The spectrum of 3C 273 was investigated by Hazard et al. [14] in 1963 by the lunar occultation method and observed the broad emission line. This source is listed in the 3C catalogue. By studying the optical spectra of 3C 273, Schmidt reported that the spectral lines were red-shifted spectral lines of hydrogen and

other elements. He, then concluded that the source was an extra-galactic radio source at redshift, $z = 0.158$. Additionally, he observed that the star-like radio source 3C 273 is the central region of a galaxy that is much brighter than the host galaxy. So, it was named as ‘Quasi-Stellar Object’ (QSO) or ‘Quasar’. This term ‘Quasi-Stellar’ was first used by Maarten Schmidt, while ‘Quasar’ was coined by Chinese-born astrophysicist Hong-Yee Chiu in the 1960s [15].

Till now, observations of AGN were primarily conducted in optical and radio wavebands. However, in the late 1970s, the Einstein Observatory, the first imaging X-ray telescope, provided detailed imaging and spectral observation in X-ray bands from AGN. Subsequently, a series of X-ray telescopes, including ROSAT (ROentgen SATellite, 1990), ASCA (Advanced Satellite for Cosmology and Astrophysics, 1993), Chandra (1999), XMM-Newton (X-ray Multi-Mirror, 1999), and NuSTAR (Nuclear Spectroscopic Telescope Array, 2012), have made substantial contributions to the field of AGN astronomy.

In 1970, Eric Persson and Maarten Schmidt proposed the ‘Unified model of AGN’, explaining that different classes of AGN primarily arise from the orientation of the jet relative to the observer’s line of sight. This marked a significant development in AGN astronomy, ushering in a new research era, which will be discussed further in [subsection 1.1.4](#).

In 1987, the Hubble Space Telescope (HST) provided a high-resolution image of AGN in optical waveband, greatly aiding detailed observations. By around 1990, scientists were able to conduct multi-wavelength observations of AGN using data from several telescopes operating in different wavebands. This progress took a significant leap in 1997 when the Compton Gamma Ray Observatory (CGRO) detected the first gamma-ray emission from a Seyfert Galaxy, NGC 4151. The Fermi Gamma-ray Telescope further revolutionized observation in gamma-ray bands. It detected numerous gamma-ray sources playing an important role in AGN study.

As technology and observational capabilities continue to advance, AGN astronomy remains a dynamic field with ongoing research to unravel the complexities of these powerful cosmic objects and their influence on the broader universe. The journey, which began with optical observations, has expanded into multi-wavelength investigations and is now venturing into the realm of multi-messenger observations; including the detection of cosmic rays and neutrinos. Despite the considerable progress made, numerous unresolved questions about AGN persist, offering exciting prospects for resolution in the near future.

1.1.2 Classification of AGN

AGNs can be divided into classes and sub-classes based on several observational aspects, e.g. radio loudness, spectral feature, luminosity, and variability.

On the basis of radio loudness, AGNs are classified into two classes: Radio-Loud (RL) and Radio-Quiet (RQ). Sramek and Weedman [16] first introduced the radio loudness parameter, R , which is the ratio of radio (5 GHz) to the optical (2500 Å) flux density. Later, different scientists ([17], [18]) calculated the value of R considering the following definition (Equation 1.1) for several AGN sources and determined the value of R . $R=10$ was accepted as a dividing line between radio-loud and radio-quiet AGNs.

$$\text{Radio Loudness, } R = \frac{L_{\text{Radio}}(5 \text{ GHz})}{L_{\text{Optical}}(2500 \text{ Å})} \quad (1.1)$$

Hence, if $R > 10$, that AGN will be denoted as radio-loud AGN (this is also called 'Kellermann's radio loudness ratio (R_K)); if $R \leq 10$, then that AGN will be denoted as radio-quiet AGN.

AGNs are classified into Type-1 and Type-2 based on the width of their emission lines (W). If $W > 1000$ km/s then that AGN will be denoted as Type-1; for Type-2 AGN, $W < 1000$ km/s. Type-1 AGN exhibits both broad and narrow emission lines, whereas Type-2 AGN exhibits narrow emission lines.

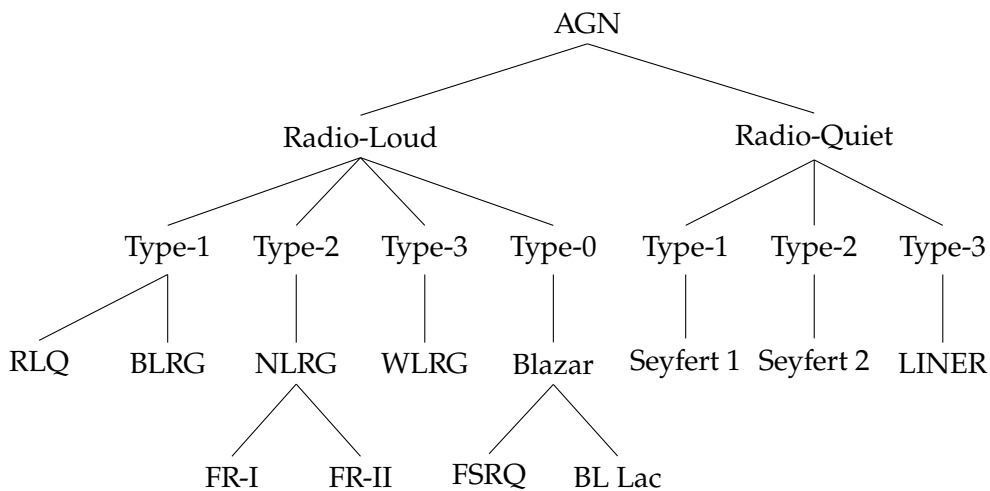


Figure 1.2. Tree chart of AGN classification (Image Credit: Fig. 3 from Tadhunter [19]). Type-3: Lower luminosity AGN; Type-0: AGN shows rapid variability in optical waveband.

1. Radio-Loud (RL):

As mentioned before, AGNs with $R > 10$ are classified as radio-loud AGNs.

They show strong emissions in the radio band. It has been found that almost 10-20% of the total AGN population is radio-loud. Produce large-scale radio jets, prefer elliptical hosts. Based on the width of the emission spectra lines and other properties, e.g. variability, the AGNs can be classified into the following sub-classes:

(a) **Radio-Loud Quasar (RLQ):**

It is a Type-1 radio-loud AGN ([Figure 1.2](#)), one of the most luminous subclasses of AGNs, with nuclear magnitudes $M_B < -21.5 + 5 \log h_0$ [20], where h_0 is the Hubble constant in 100 km/s/Mpc.

(b) **Broad-Line Radio Galaxy (BLRG):**

Broad-line radio galaxies (BLRGs) are Type-1 AGN with higher luminosity than narrow-line radio galaxies (NLRGs) and can be observed at higher redshift. Almost one-third of the observed radio galaxy belong to this group. They are strong radio emitters and exhibit broad emission lines in optical spectra, specifically Balmer lines (such as H_α line). Example: [PKS 2349-01](#), [3C 120](#) [21], [3C 227](#) [22].

(c) **Narrow-Line Radio Galaxy (NLRG):**

It is a Type-2 radio-loud AGN with narrow emission lines and powerful radio jets. They have weaker emission lines compared to the other AGNs, viz. Quasars. NLRGs are predominantly found in elliptical host galaxy, indicating an older stellar population and less dust surrounding them. Bernard Fanaroff and Julia Riley further classified them into two groups based on the radio morphology. They defined a parameter R_{FR} , which is the ratio of the distance between the regions with the highest surface brightness on the opposite sides of the central engine to the total extent of the source up to the lowest brightness contour in the radio images [23]. Sources with $R_{FR} < 0.5$ were placed in FR-I, whereas sources with $R_{FR} > 0.5$ were placed in FR-II. The luminosity boundary between these two classes is not very sharp, and there is some overlap in the luminosities of these two kinds of sources; at high frequencies, the luminosity overlap can be as much as two orders of magnitude.

(i) **Fanaroff-Riley type I (FR-I):** FR-I shows diffused and less collimated radio emission. The radio emission is brightest towards the centre and shows a characteristic 'edge-darkened' structure. This kind of AGN is often found in elliptical or lenticular galaxies.

(ii) **Fanaroff-Riley type II (FR-II):** FR-II shows more collimated and powerful radio jets, extending to a larger distance over 100 kpc to

Mpc. The radio emission is brightest at the end, creating an ‘edge-brightened’ structure. This kind of AGNs are commonly found in giant elliptical galaxies.

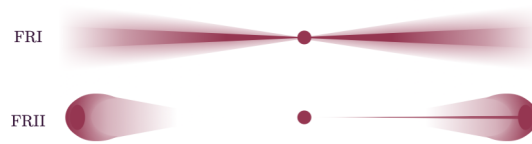


Figure 1.3. The traditional Fanaroff Riley classification of radio galaxies [24]. FR-I galaxies are “centre-bright”, and FR-II galaxies are “edge-brightened” (often with “hotspots” towards the edge).

(d) **Weak-Lined Radio Galaxy (WLRG):**

Weak-Lined Radio Galaxies (WLRG) are characterized by their weak emission lines in their optical spectra and powerful radio emission, which is why they are classified as ‘Type-3 AGN’ (Figure 1.2). They exhibit much weaker emission lines in their optical spectra compared to Seyfert and Quasar but exhibit strong radio emission. They mostly have elliptical or lenticular host galaxies with radio lobes extending to millions of light-years.

(e) **Blazar:**

This type of AGN is characterized by its extreme variability over the whole electromagnetic spectrum [25], high & variable polarization in different wavebands [26, 27], and superluminal motion. If the jet is oriented to the observer’s line-of-sight, then those kinds of AGNs are called ‘Blazars’. As the angle between the jet and the observer’s line-of-sight is nearly ‘0’ degree, this class of AGN is called ‘Type-0’ AGN (Figure 1.2). The term ‘Blazar’ was given by Ed Spiegel [25], combining the names of its two subclasses: BL Lac objects and Quasars.

Compared to the other classes of AGN, blazars show rapid variability across the whole electromagnetic spectrum. They also exhibit high and variable polarization in radio, optical, and X-ray wavebands.

Blazar spectral energy distribution (SED) typically display a characteristic double-hump structure (Figure 1.4). The low-energy peak occurs between infrared (IR) and X-ray energy ranges, and the high-energy peak occurs between X-ray and very high-energy (VHE) gamma-ray energy regimes. It is hypothesized that the low-energy hump is attributed to synchrotron radiation of the relativistic electron in the magnetic field

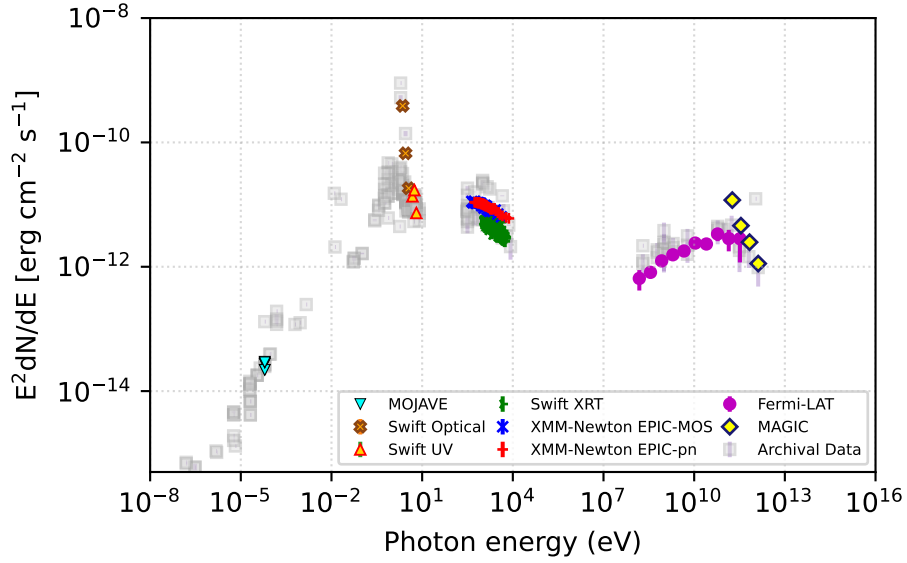


Figure 1.4. Multiwavelength SED of Mrk 180. ([Image Credit: Mondal et. al, 2023](#))

of the emission region, On the other hand, the high-energy hump is attributed to inverse-Compton (IC) radiation, either from the synchrotron photons themselves (Synchrotron-self Compton, SSC) or from external photons (External Compton, EC). The SED, within the region between ultra-violet (UV) to optical waveband, has a characteristic bump known as ‘the big blue bump (bbb)’. From the multi-wavelength spectral energy distribution (MWSED) perspective, it is found that the heights of the two humps are almost equal in the case of BL Lacertae (BL Lac), while for Flat-Spectrum Radio Quasars (FSRQs), the high-energy hump is higher than the low-energy hump. Based on the spectral features, Blazars are classified into two sub-classes: FSRQ & BL Lac.

(i) **Flat-spectrum Radio Quasar (FSRQ):**

FSRQ or Flat-spectrum Radio Quasar is a subclass of Blazar with broad emission lines (the equivalent width (EW) of the emission line is $>5 \text{ \AA}$ [28]) in the optical spectrum. They are more luminous than BL Lacs [29]. The main feature is the broad emission line from the ionized cloud surrounding the supermassive black hole (SMBH). It is found that FSRQs have higher redshift compared to the BL Lacs.

(ii) **BL Lacertae (BL Lac):**

BL Lac or BL Lacertae is a sub-class of Blazar with very weak or featureless emission spectra (typically, the width of the weak emission lines is found to be $<5 \text{ \AA}$). From the spectral feature, it is found that the spectrum of the BL Lacs does not have any broad or narrow line

emission. As a result, BL Lac does not have any BLR or NLR region. We have discussed about BL Lac in more detail in [subsection 1.1.5](#) in page no. [12](#).

2. Radio-Quiet (RQ):

This class of AGNs are almost 1000 times fainter than radio-loud AGNs. A majority of AGN belongs to this class [\[30, 31\]](#). Radio-quiet (RQ) AGNs are weak radio emitters, mostly found in spiral host galaxies [\[32\]](#).

(a) Seyfert Galaxy:

Seyfert galaxies were first discovered by an American astronomer Carl Seyfert in 1943 [\[13\]](#). They are low-luminous AGN with nuclear magnitude, $M_B > -21.51 + 5 \log h_0$ [\[33\]](#). Morphologically, the Seyfert galaxies are defined as a spiral galaxy with a bright star at the centre. This kind of galaxy has a quasar-like nucleus at the centre; its luminosity is so low that it does not outshine the host galaxy like blazars. Spectroscopically, the Seyfert galaxy can be identified with strong and highly ionised emission lines in its spectra.

Based on the presence or absence of the broad emission lines in the optical spectra [\[34, 35\]](#), there are two types of Seyfert galaxies: Seyfert 1 & Seyfert 2.

(i) Seyfert 1:

Seyfert 1 galaxies exhibit both broad and narrow emission lines in their optical spectra, and they are more luminous in UV and X-ray bands. The broad emission lines are associated with the allowed transitions (e.g. hydrogen, helium), whereas the narrow emission lines are associated with forbidden transitions (e.g. O[III]).

(ii) Seyfert 2:

Seyfert 2 galaxies are Type-2 radio-quiet AGNs characterized by the presence of only narrow emission lines in their spectra.

Based on the appearance of the broad emission lines in the optical spectra, Seyfert galaxies have been classified into other different classes: Seyfert 1.5, Seyfert 1.8, Seyfert 1.9 [\[36, 37\]](#). In this classification, Seyfert galaxies with higher numbers exhibit weaker broad emission lines compared to the narrow emission lines in the optical spectra.

(b) Low-Ionization Nuclear Emission-Line Region (LINER) :

Low-Ionization Nuclear Emission-Line Region (LINER) is characterised

by the presence of low-ionisation emission lines in their spectra, which was first identified by Heckman [38]. Spectroscopically, the spectrum of LINERs resembles the spectrum of Seyfert 2 galaxy except for the low-ionization lines, which is comparatively strong in the case of LINERs. LINERs are very common in spiral galaxies and can be easily identified [39]. There are several studies on the nature of different LINER sources, e.g. NGC 4293 and UGC 4805. It was found the central part of LINER has stellar origin rather than an AGN [40] whereas Márquez *et al.* [41] discussed the AGN nature of LINER. Therefore, this subclass of AGN serves as a potential link between normal galaxies and active galaxies [41].

1.1.3 Components of AGN

Accretion Disk

The cold and diffuse matter surrounding the black hole spirals inward toward the AGN core, forming a flat, disk-shaped structure known as ‘Accretion Disk’ (AD) [20, 42, 43]. In terms of low and high accretion rates, different models of the accretion disk were proposed in the past. The most widely accepted model was proposed by Shakura and Sunyaev [44], which suggests that the accretion disk is geometrically thin and optically thick. The matter within the accretion disk is in thermal state, resulting in black-body radiation emission in the UV [45]. The accretion disk plays a crucial role in explaining the variability observed in X-ray or optical/UV emissions from AGNs [46].

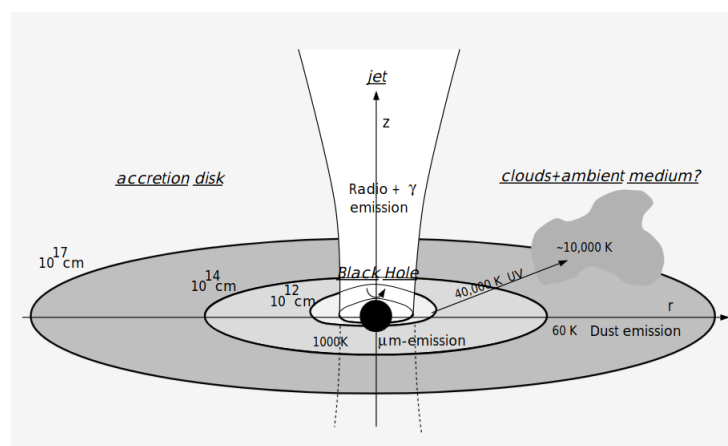


Figure 1.5. A schematic diagram of Accretion Disk around a Black Hole. (Image Credit: Heino Falcke, Lecture notes on “Standard Accretion Disks”, Page 1.)

Broad-line Region (BLR)

The Broad-line Region (BLR) lies on both sides of the accretion disk (see [Figure 1.7a](#)), situated close to the black hole (BH) and typically within about 1 light-year from the BH itself. This part is responsible for characteristic broad-line emission ([Figure 1.6a](#)), observed in the AGN spectrum. It is thought that this region is made up of dense clouds of gas and dust. These broad lines originate from the high velocity (velocity sometimes reaches up to 10,000km/s due to the strong gravitational pull of the BH and radiation pressure) gas cloud of BLR. It is difficult to measure the temperature of the BLR region directly; still, from the spectrum, it appears to be $\sim 10^4$ K. This region is spatially unresolved even in the nearest AGN, e.g. Cen A. Its size and properties can vary significantly depending on the specific source and its activity states [47]. The broad emission lines emitted from this region can be utilized to measure the mass of the SMBH [48].

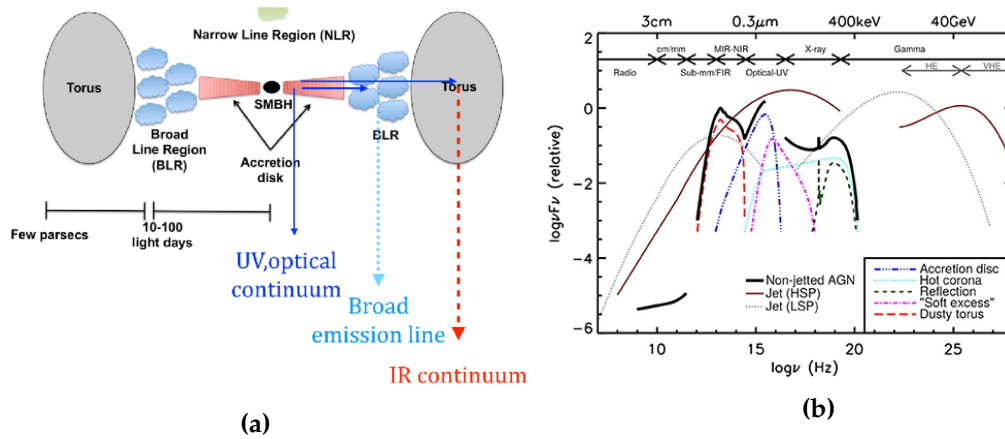


Figure 1.6. (1.6a) Schematic representation of the central structure of an AGN. (Image credit: Doré *et al.* [49]). (1.6b) AGN SED. (Image Credit: Padovani [50]).

Narrow-Line Region (NLR)

The Narrow-Line Region (NLR) in AGN is an ionised gas region outside the Broad-Line Region (BLR). It is characterized by the presence of narrow emission lines with Doppler widths usually less than around 500 km/s. Unlike the BLR, NLR is partially resolved in some of the nearest AGNs. From spectral observations, it is evident that the NLR consists of low-density gas extending over a wide region. The NLR is kinematically composite, with the "narrow components" having lower Doppler widths and arising in relatively low-density gas, while the "broad components" have higher Doppler widths and arise in a more compact, high-density region. The NLR is an crucial component of the AGN structure and serves as an important tool for studying the physical conditions and kinematics of the gas near the central supermassive black hole.

Dusty Torus (DT)

Dusty torus (DT) is a toroidal, optically thick [51–53] structure around the SMBH, made of dust and gas. It obscures the accretion disk from an observer, sitting at the edge on position (Figure 1.7a) and absorbs the emission from the accretion disk (which is in UV waveband) and re-emits to lower energy (in IR-band; Figure 1.6a). The emission from the dusty torus contributes a significant fraction of the whole IR luminosity of the AGN [54]. Furthermore, dusty torus plays an important role in ‘AGN Unification Model’ (discussed in subsection 1.1.4) to understand the physical structure of different types of AGN and the dependency on the orientation angle of the AGN jet to the observer’s line-of-sight.

Central Jet

In the perpendicular or polar direction of the accretion disk (AD), a bipolar jet is emitted from the black hole. The jet is a collimated, narrow beam of highly relativistic particles extending to kpc- Mpc scale [55]. In the case of radio-loud AGNs (discussed in item 1 of subsection 1.1.2), the luminosity released by the jet outshines the total luminosity of the host galaxy [56]. The jet is a hot magnetized plasma consisting of leptons (electrons & positrons) and protons [57], whose radiation ranges over a broad range of the electromagnetic spectrum, from radio to gamma-rays. The visibility of the AGN jet depends on several factors, e.g. the orientation angle of the AGN jet to the observer’s line-of-sight, observational wavelength etc. Radio wavelength can penetrate the dust and give a better picture of the scenario behind the obscuration caused by dust in the interstellar medium; besides, multiple space-based and ground-based telescopes in different wavebands, viz. Very Long Baseline Interferometry (VLBI) unravels great detail about the jet to the scientific community. The interaction between the long extended AGN jet with the inter-galactic medium (IGM) outside the host galaxy can trigger star formation in nearby galaxies and regulate the growth of the galaxy. This phenomenon known as ‘AGN Feedback’ [58, 59].

1.1.4 AGN Unification

In subsection 1.1.2, we discussed different classes of AGN. According to the ‘AGN Unification Model’, the different kinds of AGN are nothing but the same AGN, observed from different orientation angles based on the orientation of the AGN jet to the observer’s line of sight [1, 60] (as can be seen in Figure 1.7).

Suppose two observers: observer-1 & observer-2, are looking at an AGN from two different orientations (can be seen in Figure 1.7b). Suppose, observer-1 is looking towards the AGN from the face-on position, and observer-2 is on the

edge-on position perpendicular to the AGN jet. Now, observer-1 can see both the broad emission lines and narrow emission lines from BLR and NLR, respectively. Also, observer-1 can see the bright nucleus of the active galaxy. All these are the properties of 'Type-1 AGN'. Whereas the dusty torus obscures the central part of the AGN from observer-2, so observer-2 can only see the narrow emission lines from the NLR region. Other radiation (from AD & BLR) gets absorbed by the torus [61] and remitted to different wavebands. Also, the luminosity of the AGN is comparatively less and the bright core is not directly visible from this position. These are the characteristics of 'Type-2 AGN'. So, based on the orientation of the AGN jet and the observer's line of sight, the same AGN shows different properties, leading to different sub-classes of AGN.

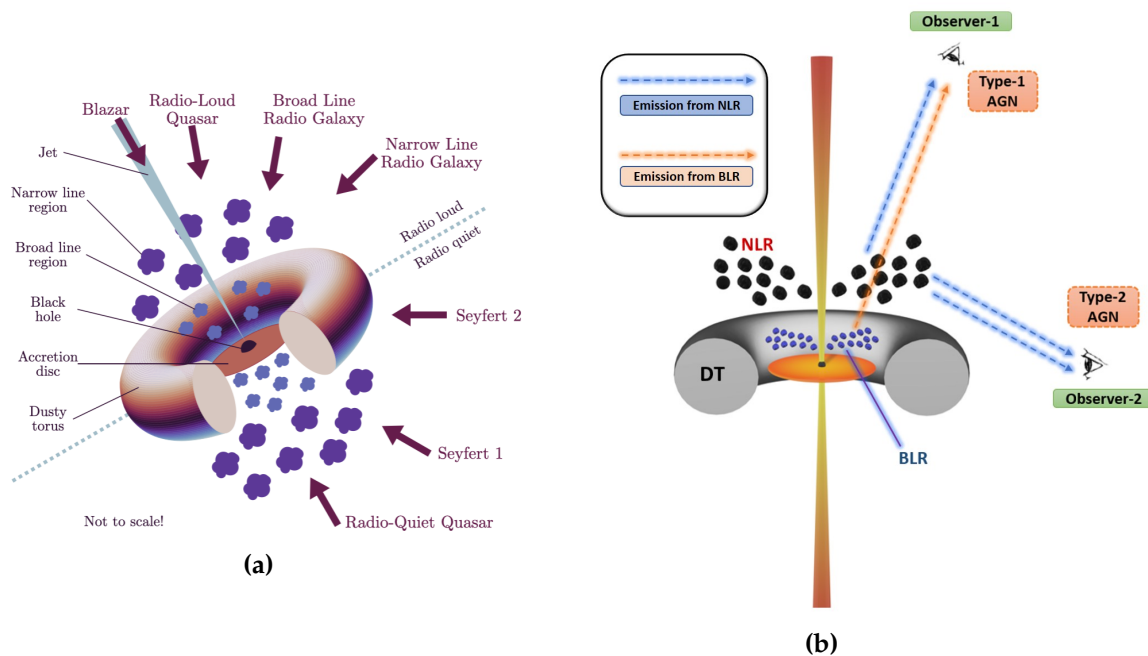


Figure 1.7. (1.7a) Unified model of AGN adapted from Urry and Padovani [1]. The thick arrows represent different viewing angles and the observed object which results from them. (1.7b) Schematic diagram of AGN.

1.1.5 Study of BL Lacs:

"Twinkle, twinkle quasi-star
 Biggest puzzle from afar
 How unlike the other ones
 Brighter than a billion suns
 Twinkle, twinkle, quasi-star
 How I wonder what you are."

- George Gamow, "Quasar" 1964.

Historically, Cuno Hoffmeister discovered the first BL Lac object between 1928-

1929 [62] at Sonnenberg. In 1965 Macleod detected a radio source, VRO 42.22.01, at the Vermillion River Observatory [63]. In the beginning, it was thought, this kind of object is actually a ‘Variable Star’. From the intensity variation of the object, it was found that the intensity varies in an irregular way. Further analysis of the optical spectrum revealed the absence of emission lines and absorption lines; in a word, the spectrum was ‘featureless’ [64, 65]. In 1972, Peter Albert Strittmatter proposed this class of object [66].

SED of BL Lac:

The SED of the BL Lac shows a double-hump structure, whose first hump is attributed to the synchrotron radiation of the relativistic electrons or positrons and the second hump is attributed to the inverse-Compton emission of synchrotron photons, where the synchrotron photons are upscattered by the synchrotron electrons to high-energy photons, known as ‘Synchrotron Self-Compton (SSC)’. For BL Lacs, it is found that the height of the two humps of the MWSED is almost the same. They show rapid variability in their luminosity [67], ranging from minute-scale [68–70] to day-scale [71] variability. As previously discussed, their emission is highly polarised with the degree of polarization being notably higher compared to FSRQ sources.

Different Classes of BL Lacs:

Depending on the position of the synchrotron peak or the low-energy peak of the MWSED of BL Lac, the BL Lacs are primarily categorized into two classes [72, 73]: low-frequency peaked BL Lac (LBL) and high-frequency peaked BL Lac (HBL). They are referred to as low-synchrotron peaked BL Lac (LSP BL Lac) and high-synchrotron peaked BL Lac (HSP BL Lac).

If the synchrotron peak lies below 10^{14} Hz, then the BL Lac is called ‘LBL’. Conversely, if the synchrotron peak lies above 10^{15} Hz, then the BL Lac is called ‘HBL’. HBLs are predominantly detected in X-rays; previously, they were called as ‘XBL’ or X-ray BL Lac. On the other hand, LBLs were primarily detected in the radio band and formerly referred to as ‘RBL’. Thus, in the case of LBL, the synchrotron radiation peaks at submillimeter to IR wavelengths, while high-energy radiation peaks at GeV energy. In the case of HBL, the synchrotron radiation peaks at UV to X-ray wavelengths with high-energy radiation peaking at TeV energy (Figure 1.8). Additionally, there is a class of HBLs known as extreme high-frequency peaked BL Lac (EHBL) [74], where the synchrotron emission peaks at hard X-ray or higher energy bands. Besides these, there is another type of BL Lac, known as ‘Intermediate-frequency peaked BL Lac’ (IBL) characterized by a synchrotron peak lying between 10^{14} Hz to 10^{15} Hz.

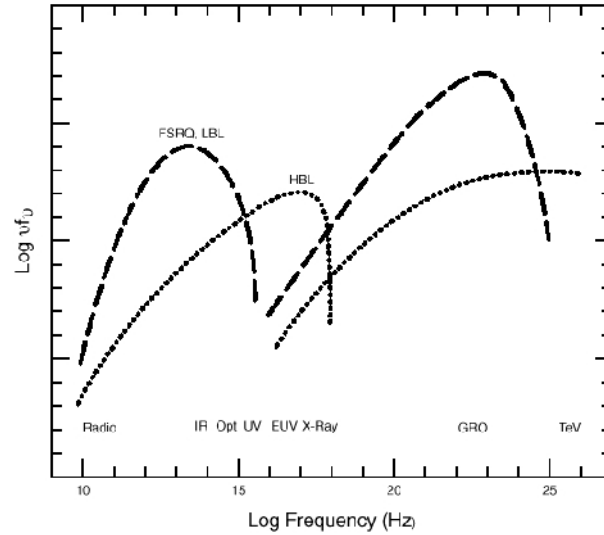


Figure 1.8. SED of FSRQ, LBL, and HBL (dotted lines). In general, FSRQ and LBL (dashed lines) are more luminous than HBL (dotted lines), so the wavelength of the peak power output correlates with luminosity. ([Image Credit: Urry, Caltech](#))

Observational Characteristics of BL Lac:

1. Doppler Boosting:

In the case of BL Lacs, the jet is oriented towards the observer's line of sight. The emission region within the BL Lac jet moves towards the observer's line of sight with relativistic velocity. For this reason, the emission region appears to move faster than its actual velocity [75]. This phenomenon is known as 'Superluminal motion'. Due to this effect, the radiation is beamed into a cone of opening angle ($\sim \frac{1}{\Gamma}$, where Γ is the bulk Lorentz factor) along the direction of the motion of the emission region. This amplifies the intensity of radiation along the direction of motion, known as the 'Doppler factor (δ)'. Due to this relativistic effect, the observed flux density from the moving emission region is higher than the actual emitted flux density. This is known as 'Doppler boosting' or 'Relativistic Beaming'. This can be calculated by multiplying a factor $\delta^{(3+\alpha)}$ to the emitted flux density [76], where α is the photon spectral index.

2. Flux Variability:

BL Lac shows rapid and high variability in their flux, observed across different wavebands. The variability time ranges from minute scale [69, 70, 77] to day scale [71]. Several research groups are investigating the reasons for this flux variability [70, 78, 79]. The variability time (t_{var}) in any specific wavelength gives a rough estimate of the size of the emission region responsible for emitting that particular waveband. The following equation can be used

to estimate the size of the emission region:

$$R < \frac{ct_{var}\delta}{1+z} \quad (1.2)$$

where R is the size of the emission region, c is the speed of light in vacuum, δ is the Doppler factor, and z is the redshift of the source. However, it just gives a rough estimation of the size of the emission region. Other factors also contribute to determining the size of the emission region within the jet [80].

3. Polarization:

Another key feature of BL Lac objects is their high degree of polarization, primarily attributed to synchrotron emission. The degree of polarization is in between 5-70% for the BL Lac objects [81–84]. This area remains open for further research, which can help to understand the jet’s magnetic field structure, the variability and the emission process. With better data accumulation with the future telescope, e.g. Square Kilometer Array (SKA) and the Extremely Large Telescope (ELT), scientists are hopeful for a deeper understanding of the underlying questions.

Emission Mechanism in BL Lac:

We mentioned in point 1e on page no. 6 that blazar SED has a characteristic double-hump structure. Blazar emission is mostly dominated by non-thermal radiation. Synchrotron emission contributes to the low-energy hump, and inverse-Compton (IC) contributes to the high-energy hump. In this section, we will give a brief description of the synchrotron emission and IC.

1. Pure Leptonic Model:

In a pure-leptonic model, only electrons or leptons are considered as relativistically accelerated particles in the jet. We maintain the charge neutrality condition within the blazar jet. So, there are non-relativistic protons or cold protons in the jet. The electrons take part in the synchrotron emission, and the same electron population contributes to the synchrotron self-Compton emission (discussed in item 1b).

(a) Synchrotron Emission:

Charged particles, moving at relativistic velocities within a magnetic field, emit radiation known as ‘Synchrotron Emission’. It is a non-thermal radiation, covering a broad range of wavelengths from radio to X-rays in the electromagnetic spectrum. Within the jet’s magnetic field, particles particularly electrons, are accelerated to relativistic

speeds and follow a spiral trajectory, resulting in the emission of synchrotron radiation [1].

(b) **Inverse-Compton (IC) Emission:**

Inverse-Compton (IC) emission is a process in which high-energy electrons upscatter low-energy photons to high-energy photons. In this process, the high-energy electron loses energy, and the photon gains energy which is just the opposite of the Compton scattering [85]; that is why this process is called 'Inverse-Compton (IC) emission' [76, 86]. Depending on the source of the target photon field, IC can be divided into two types: (i) synchrotron self-Compton (SSC) and (ii) external Compton (EC). In the external Compton process, high-energy electrons interact with external photons that are not part of the synchrotron radiation produced by the same electron population. It has been observed that in BL Lac objects, synchrotron self-Compton (SSC) contributes predominantly to the high-energy hump rather than external Compton (EC) [77, 87]. Hence, I have focused on SSC in this discussion.

- **Synchrotron-Self Compton (SSC):**

From the spectral analysis of the optical spectra of BL Lac objects, it was found that BL Lacs have a scarcity of low-energy photons for external Compton (EC) scattering. The synchrotron photons, originating from the synchrotron process, act as seed photons in the inverse-Compton (IC) process. This is known as 'Synchrotron Self-Compton (SSC)'. In this process, the high-energy synchrotron electron population responsible for synchrotron radiation, scatter the same synchrotron photons to high-energy photons. As this process involves the scattering of synchrotron photons by the same population of electrons responsible for producing those synchrotron photons, this is called 'Synchrotron Self-Compton (SSC)'. The scattered photons gain energy and contribute to the high-energy hump in the MWSED.

2. Hadronic Model:

In the hadronic model, alongside leptons, the protons are also considered to be relativistically accelerated. In some cases, it is found that the pure leptonic model is not sufficient to describe the MWSED, especially in the high-energy regime. So, along with the pure leptonic model, the hadronic contributions are taken into consideration to explain the MWSED [88]. As the hadronic models are used in conjunction with the leptonic models, they are collectively referred to as the 'lepto-hadronic model'. There are various

types of hadronic models:

(a) **$p\gamma$ interaction:**

The high-energy protons interact with the photons. The interaction channels are the following:

$$p + \gamma \rightarrow \begin{cases} n + \pi^+ \\ p + \pi^0 \end{cases} \quad (1.3)$$

The neutral pions decay to gamma photons ($\pi^0 \rightarrow \gamma\gamma$) and the charged pions decay to neutrino ($\pi^+ \rightarrow \mu^+ + \nu_\mu \rightarrow e^+ + \nu_e + \bar{\nu}_\mu + \nu_\mu$).

In this process, the seed photon may come from any external radiation field or the high-energy proton can escape the emission region and interact with the background photon field, i.e. cosmic microwave background (CMB) and extragalactic background light (EBL) initiating a cascade interaction. On the other hand, the photo-pion interaction can occur within the jet and produce charged & neutral pions. The neutral pion decays into gamma-rays, whereas the charged pions decay into leptons and photons [89].

(b) **pp interaction:**

An alternative scenario is when the relativistic protons have much lower energy than ultra-high-energy cosmic rays (UHECRs), these protons interact with the cold protons within the emission region as they are trapped in the magnetic field of the emission region. The proton-proton interactions result in the production of both neutral and charged pions. These pions decay into secondary particles, e.g. electrons/ positrons, neutrinos and γ -rays. The proton-proton interaction channels can be presented as follows:

$$p + p \rightarrow \begin{cases} \pi^0 \rightarrow \gamma + \gamma \\ \pi^+ \rightarrow \nu_\mu + \mu^+ \rightarrow \nu_\mu + e^+ + \nu_e + \bar{\nu}_\mu \\ \pi^- \rightarrow \bar{\nu}_\mu + \mu^- \rightarrow \bar{\nu}_\mu + e^- + \bar{\nu}_e + \nu_\mu \end{cases} \quad (1.4)$$

(c) **Proton Synchrotron model:**

In this model [90–92], protons take part in the synchrotron emission. For this to occur, a very high magnetic field (~ 100 G) is required. It has been found that these models can explain ‘TeV’ spectra and the emission of neutrinos from any BL Lacs. However, they are unable to account for the rapid variability observed in X-ray and gamma-ray wavebands.

1.1.6 Motivation to study BL Lacs:

- Over the last few decades, scientists have been trying to understand the emission mechanism [93, 94], the structure of the magnetic field, and the reasons for flux variability in blazars [95, 96]. Yet the mechanisms are not well understood.
- *Possible source of high-energy neutrino emission* : On 22nd September 2017, a very-high-energy neutrino ($E \sim 290$ TeV) was detected (with $\sim 3\sigma$ confidence level) for the first time by IceCube ([GCN Circular 21916](#), [AMON 50579430_130033](#)). This detection coincided directionally and temporally with a gamma-ray flare from a BL Lac TXS 0506+056 [97]. This suggests a hadronic scenario within the BL Lac object, TXS 0506+056. This detection implies that BL Lac is one of the prime candidates for the source of the extra-galactic neutrino and cosmic rays. Different blazar groups have carried out several studies in order to explain the neutrino emission associated with the gamma-ray flare of this source [98–100].
- *Possible source of UHECR*: On 27 May 2021, the Telescope Array (TA) reported the detection of a cosmic ray event of energy $\sim 244 \pm 29$ (stat.) $^{+51}_{-76}$ (syst.) EeV [101]. It is thought that high-energy cosmic rays are emitted from nearby active galaxies. Murase *et al.* [102] showed that TeV BL Lacs are possibly the site of UHECR acceleration. In another study, Toomey *et al.* [103] considered 566 AGNs at redshift (z) >0.2 from the 2WHSP catalogue of high synchrotron peaked BL Lac objects. From their analysis, they detected 160 sources with a significance above approximately 5σ ($TS \geq 25$) within the energy range of 1-300 GeV as a potential UHECR emitter.

With time, new BL Lac sources have been identified and included in the latest Fermi 4FGL catalogue. The present understanding of the particle acceleration mechanism within the jet, the emission mechanism, and the flux variability is not sufficient to explain their physical behaviour completely. It is anticipated that the new generation telescopes with better sensitivity and large field of view will yield significant insights. Our study focuses on two BL Lac sources: PKS 0903-57 and Markarian 180 (also known as Mrk 180 or Mkn 180), which have been less explored.

- ◆ On 22nd June 2015, Fermi-LAT reported the detection of gamma-ray flare from PKS 0903-57 [104]. The daily average flux was 30 times higher than its average flux in the 3FGL catalogue. Fermi-LAT detected two more gamma-ray flares on May 2018 [105] and in March 2020 [106], respectively. The latter

one was the highest gamma-ray flux ever detected from this source, with daily average gamma-ray flux about 60 times higher than the average flux reported in the 4FGL catalogue [107]. This flare was also reported in LAT GCN 1585493148 ([GCN 1585493148](#)). On 1st April 2020, AGILE reported enhanced gamma-ray activity from this source [108]. Despite multiple flaring activities, we found that this source had not been studied before at that time. However, later Shah *et al.* [109] studied this source during its brightest flare in 2020. So, we were motivated to study the underlying mechanism of emission of this source due to its multiple high gamma-ray flux enhancement reported by Fermi-LAT, AGILE etc.

- ◆ Another source, Markarian 180 (Mrk 180), is a High-frequency BL Lac (HBL) object at a redshift of 0.045. An earlier study by He *et al.* [110] showed this is a potential candidate for UHECR acceleration contributing to the Telescope Array (TA) hotspot above energy 57 EeV [110]. The underlying physics of its emission at TeV energies was not well understood. Both these factors motivated us to study the emission mechanism of Mrk 180 and to investigate the association of UHECR with Mrk 180.

1.1.7 Overview

In this thesis, we mainly focused on investigating two BL Lac sources: PKS 0903-57 & Markarian 180 (Mrk 180). We conducted a detailed spectral and temporal study to explore the physical properties of BL Lacs, e.g. emission mechanism, flux variability etc. We analysed and modelled the data in an attempt to understand the underlying physical explanations. This thesis is organized into the following chapters:

- In **chapter 1**, I have briefly described Active Galactic Nuclei (AGN) and BL Lacertae objects (BL Lacs).
- In **chapter 2**, I have discussed about those astronomical facilities whose data have been used in our work and described the data reduction and analysis procedure of Fermi-LAT, SWIFT, and XMM-Newton.
- In **chapter 3**, I talked about the detailed temporal and spectral study of the flaring states of PKS 0903-57 with the multi-wavelength data analysis and modeling.
- In **chapter 4**, I discussed our work on another BL Lac object, Markarian 180.
- In **chapter 5**, We summarize the findings from our work and discuss future prospects in this field.

Multi-wavelength Observation: Data Analysis & Reduction

BL Lacs radiate over a wide range of the electromagnetic spectrum, from radio-band to very-high-energy (VHE) gamma-rays. To study these sources, multi-wavelength data is required. For our work, we have analysed Fermi-LAT gamma-ray data, SWIFT XRT & UVOT data, and XMM-Newton data and compiled archival data from MAGIC, MOJAVE, and ATCA. In this chapter, I will briefly introduce those astronomical facilities, data analysis, and data reduction methods.

2.1 Fermi Gamma-Ray Telescope:

2.1.1 Introduction:

In 1995, the National Aeronautics and Space Administration (NASA) formed the Gamma-Ray Astronomy Program Working Group (GRAPWG), a governing body to recommend the future directions of NASA's gamma-ray astronomy program. In 1997, the working group submitted a report on the future gamma-ray astronomy program. Among all the projects, the 'Gamma-ray Large Area Telescope' (GLAST) was at the top of the priority list; later, it was renamed to 'Fermi Gamma-ray Space Telescope' (FGST), in honour of the eminent physicist Enrico Fermi. The planning of FGST began in 1996 [111] with a detailed design of the GLAST tower structure. In November 1999, a detailed 'Flight Investigation' proposal was submitted to the NASA office, which contained the instrument design, i.e. the design of the GLAST facility, instrument capability, and its scientific goals [112].

2.1.2 About the Instrument:

FGST carries two instruments onboard: (i) Fermi Large Area Telescope (Fermi-LAT), and (ii) Fermi Gamma-ray Burst Monitor (Fermi-GBM). The LAT is Fermi's primary instrument, and GBM is the secondary instrument. The main focus of Fermi-GBM is to detect any sudden enhancement in gamma-ray flux from any transient source within the energy range of 8 keV and 40 MeV. This is an imaging, pair-conversion, wide-field-of-view, high-energy gamma-ray telescope that can detect photons of energy 20 MeV to more than 300 GeV with a field of view of 2.7 sr at 1 GeV and above [113, 114]. At any moment, it can observe approximately 20% of the sky. In survey mode, it covers the whole sky in two orbits around the

Earth (Fermi's orbital period is ~ 96 minutes), which takes about 3 hours. Fermi was launched in the near-earth orbit on 11th June 2008 and is still in operation.

Fermi-LAT consists of a segmented Anticoincidence shield (ACD), an array of 16 tracker (TKR) modules, and 16 calorimeter (CAL) modules (Figure 2.1a). The ACD comprises 89 plastic scintillator tiles (the anticoincidence shield in Figure 2.1b). The TKR and CAL modules are mounted to the instrument's central structure. Each TKR module consists of 18 XY tracker planes which have an array of silicon-strip tracking detectors (SSDs) to track the charged particle ('particle tracking detectors' in Figure 2.1b). There are tungsten plates in front of the SSDs that act as a converter. But, just in front of the calorimeter, there is no converter. Each CAL module consists of 96 Cesium Iodide, activated with Thallium (CsI(Tl)) crystals. The LAT calorimeter is a total absorption calorimeter.

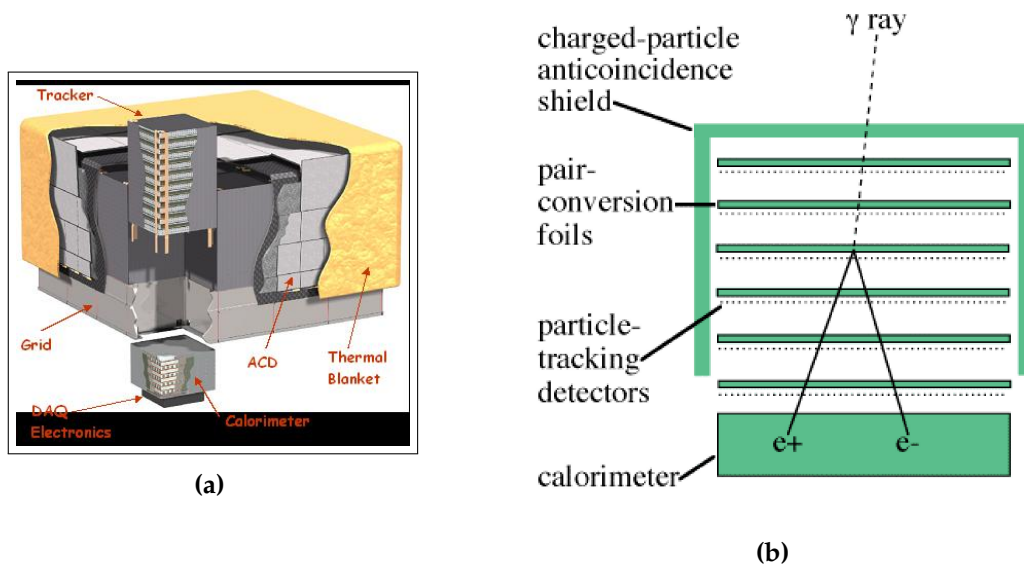


Figure 2.1. (2.1a) Structure of LAT (Image Credit: Fermi-LAT Website). (2.1b) Schematic structure of Fermi-LAT (Image Credit: Geant4 Simulation of High Energy Gamma Ray Experiments)

2.1.3 Gamma-ray detection method:

Fermi-LAT detects gamma-rays by pair-conversion technique. When a gamma-ray photon penetrates the detector, it interacts with the TKR's tungsten and converts the incident photon into an electron and positron pair. The SSD track this electron-positron pair. As the energy of the incident gamma-ray photon is much larger than the rest mass energy of the electron and positron, both continue to move predominantly in the direction of the incident photon. In this way, these particles continue to hit another deeper layer of tungsten, each creating further particles. The direction of the incoming gamma-ray is determined by tracking the direction of these cascading particles back to their source using high-precision SSDs [115].

The CAL is thick enough to adequately measure the energy of the pairs in the LAT energy band. The total energy of the particles created depends on the energy of the incident gamma-ray; counting up the total energy determines the energy of that gamma-ray.

2.1.4 Raw data reduction:

There are two types of Fermi-LAT datafile:

1. Event file: This file contains information about the photons and time of observation. There are two kinds of event files: Photon file and Extended file. Photon files contain all the SOURCE classes and are usable for most analyses, whereas the Extended files contain the same events as the photon files. They also include additional information that can be useful to characterise the quality of a specific signal [116].
2. Spacecraft file: The spacecraft file contains all the information about the satellite, e.g. its position in the orbit, its pointing direction etc. It also contains information about the satellite passing over the South Atlantic Anomaly (SAA), where Earth's inner Van Allen radiation belt comes closest to Earth's surface. This leads to an increased flux of energetic particles in this region. Fermi-LAT does not collect any data when it flies over SAA.

We collected Fermi-LAT data from [Fermi-LAT Data Server](#). After that, we used two tools for data reduction and analysis. For our first work, i.e. for studying PKS 0903-57, we used 'Fermi Science Tools', and for our second work, i.e. for Mrk 180, we used 'Fermipy', which was optimised for faster operation. I have mentioned the data reduction and analysis procedure with 'Fermi Science Tools' in [subsection 3.2.1](#) and 'Fermipy' in [subsection 4.2.1](#).

2.2 Neil Gehrels Swift observatory

Neil Gehrels Swift observatory is a multi-wavelength space-based observatory with three instruments onboard: Burst Alert Telescope (BAT; 15.0- 150.0 keV), X-Ray Telescope (XRT; 0.3- 10.0 keV) and Ultraviolet and Optical Telescope (UVOT; 170- 600 nm) [117]. It was primarily designed to study Gamma-ray Bursts (GRBs) [118]. It observes the sky in hard X-ray, soft X-ray, ultraviolet, and optical wavebands. Swift provides simultaneous data of any transient activity in all wavebands ranging from X-ray to optical.

- The BAT instrument is used as a transient monitor with a field of view of ~ 2 sr. This instrument works between 15- 150 keV [119], i.e. in the hard X-ray regime.

- The XRT works between 0.3-10.0 keV. It is a focusing X-ray telescope with a 110 cm^2 effective area at 1.5 keV, 23.6×23.6 arcmin FOV, 18 arcsec resolution (half-power diameter). This instrument uses a grazing incidence Wolter I telescope to focus X-rays onto the CCD. Depending on the brightness of the source, XRT can operate in any of the following modes:
 1. Imaging mode (IM): This mode is only used to obtain 1st X-ray position of a new GRB.
 2. Photo-Diode mode (PD): It is a fast timing mode with a time resolution of 0.14 milliseconds. This mode has been turned off since May 2005.
 3. Windowed Timing mode (WT): This mode is generally used for extremely bright sources. In this mode, the time resolution is 1.8 milliseconds.
 4. Photon Counting mode (PC): This is the primary mode of XRT. In this mode, the time resolution is 2.5 seconds, but this mode retains full imaging and spectroscopic resolution. This mode is preferable for observing a very low flux source ($< 1 \text{ mCrab}$).

We collected the SWIFT data from [Heasarc data archive](#). We obtained the Level 2 data files running a task 'xrtpipeline' (version 0.13.5) on the Level 1 data [120].

In the case of Swift-XRT data, we used the clean event files corresponding to Photon-Count mode (PC mode), which we obtained from the previous step. The standard data reduction procedure [121] was followed to extract the source and background region. The calibration file (CALDB; version 20190910) and other standard screening criteria were applied to the cleaned data. A radius of interest (ROI) of 20-30 pixels was considered to mark the source region (here, it was a circular region around the source), the radius of the background region was also the same, but it was far away from the source region. With the help of the 'xselect' tool [122], we selected the source and background regions and saved the corresponding regions' spectrum files. Then 'xrtmkarf' [123] and 'grppha' [124] tools were used to generate ancillary response files (arfs) and group the spectrum files with the corresponding response matrix file (rmf); thereafter 'addspec' [125] and 'mathpha' [126] were used to obtain the source and background spectrum respectively. Thus, we obtained the spectrum. The spectrum was modelled with xspec (v12.11.0; [127]) tools and obtained the Spectral Energy Distribution (SED) and flux.

Swift UVOT monitors with all six filters: U(3465 Å), V (5468 Å), B (4392 Å), UVW1 (2600 Å), UVM2 (2246 Å) and UVW2 (1928 Å). In our analysis, the source region was extracted from a region of 5" around the source, keeping the source at the centre of the circle. The background region has been taken ~ 3 times larger than the source region and is far away from the source region. We extracted the source magnitude using the ‘uvotsource’ [128] tool. This magnitude did not include the galactic absorption, so it was corrected. A python module ‘extinction’ [129] was used to get the extinction values corresponding to all the Swift-UVOT filters. We considered Fitzpatrick (1999) [130] dust extinction function for $R_V=3.1$, where R_V is a dimensionless quantity, which is the slope of the extinction curve. For diffused interstellar medium (ISM), the mean value of R_V is 3.1 [131–133]. We obtained the corrected magnitude, which was then converted into flux using zero point correction [134] and conversion factors [135]. For SED, we combined the image files of all the observation IDs of any particular UVOT filter with ‘uvotimsum’ [136]. The output of ‘uvotimsum’ was used as the input in ‘uvotsource’ to obtain the magnitudes, which were then corrected and converted to the flux in the previous manner, and then we calculated the SED.

2.3 XMM-Newton

XMM-Newton is a space-borne X-ray observatory consisting of three imaging X-ray cameras (European Photon Imaging Camera or EPIC), two grating X-ray spectrometers (Reflection Grating Spectrometer or RGS) and one optical monitor (OM). It was launched on December 10, 1999. Because of its great capacity to detect X-rays, it was formally known as the High Throughput X-ray Spectroscopy Mission. Now it is called XMM because of its multi-mirror design. The three EPIC cameras are the primary instrument aboard XMM-Newton; two are MOS-CCD cameras, and the other is a pn-CCD camera. The energy range of EPIC is about 0.15 keV- 15.0 keV. The MOS-CCD cameras are used to detect low-energy X-rays, whereas the pn-CCD camera is used to detect high-energy X-rays. RGS operates from 0.35 keV to 2.1 keV. OM covers from 170 nm to 650 nm.

We have followed standard data reduction procedure [137] to extract the SED. We extracted SED points from MOS1 and MOS2; we got the SED points from MOS. Also, we extracted SED points from the pn detector. Thereafter, we used xspec (v12.11.0; [127]) to model these spectra and obtained the SED. Other than X-ray data, we have also analyzed OM image mode data. Following the same data reduction procedure, we prepared the data and used ‘omichain’ for further analysis. We followed ‘omichain’ instruction for the last step. By ‘om2pha’ command, we extracted the spectrum file to analyze in xspec. The required OM

response files have been copied from [OMResponseFile](#) for this step.

2.4 Publicly Available Archival Data:

2.4.1 MAGIC Data:

MAGIC, or Major Atmospheric Gamma Imaging Cherenkov telescope, started operating to observe the very-high-energy (VHE) gamma-rays in 2005. It is a ground-based facility situated at a height of 2400m on the hilly top of La Palma, one of the Canary Islands. It was built at the Roque de los Muchachos Observatory, where High-Energy-Gamma-Ray Astronomy(HEGRA) was previously installed (1987-2002) [138]. MAGIC is a system of two Imaging Atmospheric Cherenkov Telescopes (IACT). Very-high-energy (VHE) γ -rays impinging the Earth's upper atmosphere initiate cascade interactions, producing a shower of secondary particles, mainly electrons and positrons. Electrons and positrons moving faster than the phase velocity of light in the atmosphere emit Cherenkov radiation, mainly in the UV-blue band, for a few nanoseconds. MAGIC collects the Cherenkov light and focuses it onto a pixelised camera comprising 576 photomultipliers (PMTs). Using dedicated image reconstruction algorithms, the energy and incoming direction of the primary γ -rays are calculated [139]. This telescope can detect γ -rays of energy 30 GeV to 100 TeV.

2.4.2 MOJAVE Data:

MOJAVE (Monitoring Of Jets in Active galactic nuclei with VLBA Experiments) is a long-term program to monitor radio brightness and polarization variation in jets associated with active galaxies visible in the northern sky [140]. MOJAVE observes at three wavelengths, 7 mm, 1.3 cm, and 2 cm, to obtain a full polarization image with an angular resolution better than 1 millisecond.

2.4.3 ATCA Data:

The Australia Telescope Compact Array (ATCA) [141] is a radio telescope at the Paul Wild Observatory near Narrabri in New South Wales, Australia. It is an array of six identical 22-m antennas used for radio astronomy. The antennas are positioned along a broad gauge rail track so that they can be moved into different arrangements to get the best possible images of the sky for different kinds of observations.

Spectral Modeling of Flares in Long Term Gamma-Ray Light Curve of PKS 0903-57

3.1 Introduction

PKS 0903-57 is a BL Lac [142] type object also known as 3FGL J0904.8-5734 or 4FGL J0904.9-5734, located at redshift $z = 0.695$ [143] with RA= 136.222 deg or 09h04m53.1790s & DEC=-57.5849 deg or -57d35m05.783s [144].

PKS 0903-57 was studied for the first time in 1987 [145] and classified as a quasar by FST (Fleurs Synthesis Telescope). In 1990 based on the optical brightness, 37 PKS sources (detected by the Parkes Observatory, Parkes 2700 MHz survey) were observed and PKS 0903-57 was one of them; mentioned as '0903-573'. They classified it as 'Seyfert I'. As they were not sure about the classification, it was listed among the 'misidentified sources'. Later, in both of the Fermi 3FGL [146] & 4FGL [147] catalogs, this source has been classified as 'BCU' ('Blazar candidates of uncertain type'). In 'Simbad' it is classified as 'BL Lac type object' as suggested by [142] . In the period between August 2008 to the beginning of 2020, two enhanced γ -ray activity states were reported, though they were much dimmer compared to the flares detected during March-April of 2020. Along with Fermi Large Area Telescope (Fermi-LAT) other observatories like ATCA (Australia Telescope Compact Array), Swift, AGILE (Astrorivelatore Gamma ad Immagini LEggero), DAMPE (Dark Matter Particle Explorer), HESS (High Energy Stereoscopic System) also observed this source during March-April 2020. Following are the details of the alerts, from where we get a brief history of its activity.

On 22nd June 2015, Fermi-LAT detected γ -ray flare from this source [148] with daily average flux $(1.2 \pm 0.3) \times 10^{-6}$ ph cm $^{-2}$ s $^{-1}$ above 100 MeV, which was 30 times higher than its average flux in 3FGL catalog.

Again, Fermi-LAT detected GeV γ -ray flare from this source on 14th May 2018 [149] with daily average flux $(2.2 \pm 0.2) \times 10^{-6}$ ph cm $^{-2}$ s $^{-1}$ above 100 MeV, about 55 times higher than its flux reported in the 3FGL catalog.

In 2020, very high γ -ray flux was detected by Fermi-LAT; this is the highest γ -ray flux ever detected from this source. On 28th March 2020, an elevated γ -ray flux with two GeV photons ($E > 10$ GeV) with daily average flux $(3.8 \pm 0.4) \times 10^{-6}$ ph cm $^{-2}$ s $^{-1}$ above 100 MeV was observed [106]. This time the γ -ray flux was about

60 times higher than the average flux reported in the 4FGL catalog. This was the third time Fermi-LAT detected such enhanced γ -ray activity from this source. This flare was also reported in the LAT GCN 1585493148.

AGILE reported enhanced γ -ray activity from the same source on 1st April 2020 [150].

Fermi-LAT also reported very-high energy γ -ray emission from PKS 0903-57 on 1st April 2020 [151]. Preliminary analysis of Fermi-LAT data reported several high-energy (>10 GeV) photons which were positionally consistent with this source. It was found that the association of those high-energy photons with this source was highly probable. Amongst them a 106 GeV photon was detected on 31st March 2020 at 13:56:27.000 UTC. This was the first evidence of VHE (Very-High Energy) γ -ray emission from PKS 0903-57 by Fermi-LAT.

On 13th April 2020, first time HESS reported the detection of very-high energy γ -ray during a follow-up observation from the intermediate BL Lacertae object PKS 0903-57 [152].

ATCA monitored this source periodically. On 15th April 2020, ATCA released a report on the recent activity of this source [153]. They observed this source on 2nd April 2020 in six radio bands with a duration of 10 mins in each band and reported the fluxes in each band.

DAMPE reported about the detection of GeV γ -rays from the source PKS 0903-57 on 17th April 2020 [154] with daily average flux $\sim(5.9\pm 2.3)\times 10^{-7}$ ph cm $^{-2}$ s $^{-1}$.

The underlying mechanism of flux variability of the blazars is still unknown to the community. Many models have been proposed to explain the variability in short time scale but the models are highly flare-dependent and in some cases also source dependent.

In our 12 years long Fermi-LAT γ -ray data analysis we have identified two flares: Flare-1 & Flare-2. Further smaller binning of the γ -ray light curve reveals the sub-structures prominently. Flare-1 has one sub-structure, consisting of two phases. Flare-2 has two sub-structures: Flare-I and Flare-II; the first one has five phases and the later one has three phases. These phases consist of preflare, flares and postflare states. The flaring phases have been fitted with a sum of exponential equations to calculate the rising & decay time of the peaks of the phases. Thereafter, we have calculated the γ -ray variability time which is found to be hour scale. We have fitted the γ -ray SEDs of different phases with different models, PowerLaw (PL), LogParabola (LP), BrokenPowerLaw (BPL) and PowerLaw Exponential Cutoff (PLEC) to find out the model which represents the data best. We do not find any specific hardening or softening pattern in the fitted spectrum. On the basis of the maximum likelihood analysis, LogParabola is the best-fitted model

which we have used in modeling the multi-wavelength SED with the help of a time-dependent code. Our results show that one zone leptonic model is sufficient to model the multi-wavelength SED. For better understanding of the physical processes more simultaneous multi-wavelength data is required.

In this work, we have studied the γ -ray data from 4th August 2008 to 6th January 2021. After identifying significant flares in the γ -ray data, we have included the multi-wavelength data from several instruments and modeled the flaring phases. In [section 3.2](#), we have discussed the multi-wavelength data analysis; in [section 3.3](#) we have identified the flares and their sub-structures from the γ -ray light curve. In [section 3.4](#), we have discussed the method of identification of different phases of the flares & the fitting of the γ -ray light curve with a functional form to compute the rising and decay timescale of the flaring phases. In [section 3.5](#), we have discussed about the γ -ray flares, their sub-structures & phases in detail. In [section 3.6](#), we have discussed the fitting of the γ -ray SEDs with different functional forms e.g. PowerLaw (PL), LogParabola (LP), BrokenPowerLaw (BPL) and PowerLaw with Exponential Cutoff (PLEC). In [section 3.7](#), we have done time-dependent modeling of the multi-wavelength SEDs with ‘GAMERA’ and calculated the total jet power required in our model. We have discussed our results in [section 3.8](#) and the conclusion is given in [section 3.9](#).

3.2 Data Analysis

3.2.1 Fermi-LAT Data Analysis

PKS 0903-57 has been continuously monitored by Fermi-LAT from 4th August 2008, 15:43:36 UTC and this source is listed in their regularly monitored source-list [[155](#)].

The Pass 8 Fermi-LAT γ -ray data of PKS 0903-57 was extracted from Fermi-LAT data server [[156](#)] for a period of more than 12 years (August 2008 to January 2021), and the analysis has been done with Fermi Science Tools software package (version v11r5p3; [[157](#)]), following the ‘Unbinned Likelihood analysis’ method.

- It is recommended that during analyzing a point source, one should include those events having higher probability of being photons. To prepare the data for analysis, we have used the ‘gtselect’ command in the Fermi Science Tools software package. We have used Pass 8 data where the photon-like events are classified as evclass=128 (the Fermi-LAT collaboration recommended to use the ‘SOURCE’ event class for relatively small regions of interest ($<25^\circ$) [[158](#)]. We have used ‘P8R3_SOURCE’ event class for which ‘evclass’ has to be set to a value 128) [[159](#)] and evtype=3 (each event class includes different event types which allows us to select events based on different criteria. The

standard value of 'evtype' is 3, which includes all types of events i.e. front and back sections of the tracker (denoted by FRONT+BACK), for a given class.). We have extracted the Fermi-LAT Gamma-Ray data from Fermi Science Support Center (FSSC) considering a search radius of 20° around the source PKS 0903-57. During the data preparation we have selected 'Region of Interest (ROI)' of 10° , as suggested in Fermi's Data Preparation page [160]. We have also selected the maximum and minimum energy range and maximum zenith angle cut, which was 90° . This zenith-angle cut is chosen to avoid any background gamma-rays produced from the Earth's limb.

- After this, we have used 'gtmktime' to select those time intervals when Fermi-LAT was working in standard data collection mode, and the data quality was good. These time intervals are also called. 'good time intervals' (GTIs). After this step, we have checked the maximum energy of the photon in our prepared data sample. This is just to ensure that the prepared data has enough photons at higher energies otherwise, the likelihood fit will fail. We opened the GTI-corrected output file with the 'fv' command and clicked the 'Hist' button under the 'EVENTS' extension, followed by selecting the 'ENERGY' column along the X-axis. Here, we checked the 'Data Max'. The value of 'Data Max' is of the same order as the maximum energy that we applied during the data preparation with 'gtselect', so we proceed for further analysis. If the value of 'Data Max' is much smaller than the maximum energy used in 'gtselect', the maximum energy has to be lowered to make a tighter energy cut to ensure enough photon statistics at higher energies.
- In the next step, we have created 'livetime cube' with 'gtltcube' command. Fermi-LAT collects data in survey mode. So, the angle between the direction of the source and the instrument's Z-axis changes with time. This angle is called, 'inclination angle' or 'off-axis angle'. The Fermi-LAT instrument response function also depends on this 'off-axis angle'. The number of counts from any particular source or from any region of the sky depends on the amount of time that any source spends at any particular inclination angle during the observation. The 'livetime' is the time that Fermi-LAT observes any particular position in the sky at a particular inclination angle. The array of these livetimes at all the points in the sky is called, 'livetime cube'. The command 'gtltcube' calculates the livetime cube.
- Thereafter, we have calculated the exposure map by the command 'gt-expmap' and for this we needed to give the GTI output file, the spacecraft file, and the 'livetime cube' output file as input. This is required for the

prediction of the number of photons within a given Region-of-Interest (ROI) for diffuse components in our source model. Most importantly, this is used only for unbinned likelihood analysis. Here, the exposure is an integral of the total response over the entire ROI.

Moreover, we have used Fermi-LAT fourth source catalog (4FGL) [147], the galactic diffuse emission model (gll_iem_v07.fits), and extra-galactic isotropic diffuse emission model (iso_P8R3_SOURCE_V2_v1.txt) to build the model XML file. We used a GUI tool, ‘model editor’ to create the model xml file. The model XML file would have many sources within the ROI, and the likelihood analysis optimizes the spectral parameters of all the sources. The model XML file also has sources outside the ROI, which are generally fixed to their 4FGL catalog values. After the selection of the events, good time interval, livetime, and exposure map the diffuse response of the instrument has been computed eventually with the command ‘gtdiffrsp’. The diffuse response depends on the instrument response function (IRF), in this case, it was ‘P8R3_SOURCE_V2_v1’. In this step, an extra column adds up to the event data file.

Now, we have used ‘gtlike’ command to perform unbinned likelihood analysis to obtain best-fit model parameters between the observed data and the given input model. There are five optimizers, we have chosen the ‘NEWMINUIT’. The NEWMINUIT should be converged. We have followed the steps mentioned in Fermi data analysis manual and finally NewMinuit has converged for ROI=7°. Further study is done for considering the photons from a ROI of 7° around the source.

For localization of the source a quantity, ‘Test Statistics’ (TS) is generally computed, defined as,

$$TS = -2 \log \frac{L_0}{L_1} \quad (3.1)$$

where, L_0 and L_1 are the maximum likelihood value for a model without (null hypothesis) and with a point like source at the position of the source respectively. Larger is the TS value; higher is the probability of the presence of the source.

To generate the light curve, we have fixed all the parameters of all the sources in our radius of interest (ROI) except our source of interest from the fourth Fermi-LAT catalog (4FGL). Using pyLike, UnbinnedAnalysis modules we have generated γ -ray light curve in five different time bins: 7-day, 1-day, 12-hour, 6-hour, and 3-hour and subsequently generated SEDs of different activity periods using the user contribution tool (likeSED.py) [161].

3.2.2 Swift XRT and UVOT Data Analysis

PKS 0903-57 was monitored by Swift during its flaring states. The details of the observations are tabulated in [Table 3.1](#). Nearly, 15 observations are found corresponding to the detected γ -ray flares.

In Swift XRT data, we have used clean event files corresponding to Photon-Count mode (PC mode), which we obtained using a task ‘xrtpipeline’ version 0.13.5. Calibration file (CALDB), version 20190910 and other standard screening criteria have been applied to the cleaned data. A radius of interest (ROI) of 20-30 pixel has been considered to mark the source region, the radius of the background region is also the same, but it is far away from the source region. With the help of ‘xselect’ tool, we have selected source region & background region and saved the spectrum files of the corresponding region. Then ‘xrtmkarf’ and ‘grppha’ tools have been used to generate ancillary response file and group the spectrum file with the corresponding response matrix file; thereafter ‘addspec’ and ‘mathpha’ have been used. The SEDs corresponding to different flaring phases have been obtained. Thereafter, the spectra have been modeled with xspec [162] (Version 12.11.0) tools. During fitting, we have considered neutral hydrogen column density, $n_{\text{H}}=2.6 \times 10^{21} \text{ cm}^{-2}$ [163]. These X-ray SEDs have been shown in the multi-wavelength SEDs corresponding to their flaring phases.

PKS 0903-57 was also monitored by Swift UVOT (Ultraviolet/Optical Telescope) in all six filters: U (3465 Å), V (5468 Å), B (4392 Å), UVW1 (2600 Å), UVM2 (2246 Å) and UVW2 (1928 Å). The source region has been extracted from a region of 5 arcsec around the source, keeping the source at the centre of the circle. The background region has been taken ~ 3 times larger than the source region far away from the source region. Using ‘uvotsource’ tool, we have extracted the source magnitude. This magnitude doesn’t consider the galactic absorption, so it has been corrected. As there is no documentation from where we can collect the extinction value for this source, we have used the extinction value using a python module ‘extinction’ [129] corresponding to all the Swift UVOT filters for this source. We have considered Fitzpatrick [164] dust extinction function for $R_{\text{V}}=3.1$. Following are the values of the extinction coefficients of different Swift UVOT wavebands that have been used here; V: 0.986, B: 1.311, U: 1.591, UVW1: 2.126, UVM2: 2.958, UVW2: 2.614. Subsequently, the corrected magnitudes have been converted into flux by using zero point correction [134] and conversion factors [135].

Table 3.1: Table for SWIFT XRT/UVOT observations, used in this paper

Sr. No.	Instrument	Observation ID	Starting Time (MJD)	XRT Exposure (ks)	UVOT Exposure (ks)
1	SWIFT XRT/UVOT	00033856003	58221.739	1.9	1.9
2	SWIFT XRT/UVOT	00033856004	58222.872	1.7	1.7
3	SWIFT XRT/UVOT	00033856005	58223.133	1.3	1.3
4	SWIFT XRT/UVOT	00033856009	58937.110	1.9	1.9
5	SWIFT XRT/UVOT	00033856010	58938.176	1.9	1.9
6	SWIFT XRT/UVOT	00033856011	58941.496	1.7	1.7
7	SWIFT XRT/UVOT	00033856012	58944.154	2.2	2.1
8	SWIFT XRT/UVOT	00033856014	58945.890	1.9	1.9
9	SWIFT XRT/UVOT	00033856015	58946.817	1.9	1.9
10	SWIFT XRT/UVOT	00033856013	58947.474	0.6	0.5
11	SWIFT XRT/UVOT	00033856016	58951.978	1.9	1.9
12	SWIFT XRT/UVOT	00033856017	58953.051	1.9	1.9
13	SWIFT XRT/UVOT	00033856018	58954.436	0.7	0.7
14	SWIFT XRT/UVOT	00033856019	58955.171	2.0	1.9
15	SWIFT XRT/UVOT	00033856020	58956.360	1.9	1.9

3.3 Flaring States of PKS 0903-57

We have analyzed the γ -ray light curve of PKS 0903-57 observed over 12 years in different time bins. [Figure 3.1](#) shows 7-day binning of γ -ray light curve of this source, which was observed by Fermi-LAT from MJD 54682.65 (4th August 2008; 15:43:36 UTC) to 59220 (6th January 2021; 00:00:00 UTC). From [Figure 3.1](#), we have identified two flaring states (denoted by a pair of vertical red-dotted lines for each flaring states). We have indicated these two flaring states as Flare-1 and Flare-2, which were observed between MJD 58216.5 to 58230 and MJD 58920 to 58976 respectively. Our work is focused on the flaring states; hence a detailed analysis has been carried out on the flaring states only. Within a larger flare, there are smaller flares with preflare and postflare states before and after them. A sub-structure consists of multiple phases of flare, preflare and postflare. We have studied the flares in 1-day time bin to detect their sub-structures and different phases, thereafter we have analyzed them in 12-hour, 6-hour and 3-hour time bin to detect the sub-structures and phases more precisely. Flare-1 has only one sub-structure ([Figure 3.4](#)) whereas Flare-2 has two sub-structures ([Figure 3.7](#)), labeled as: Flare-I & Flare-II.

For some phases, the error bars on the data points in their 3-hour binned γ -ray light curves are larger compared to those in their 6-hour binned γ -ray light curves. However, in their 6-hour binned γ -ray light curves, the flaring segments have comparatively fewer data points compared to those in their 3-hour binned

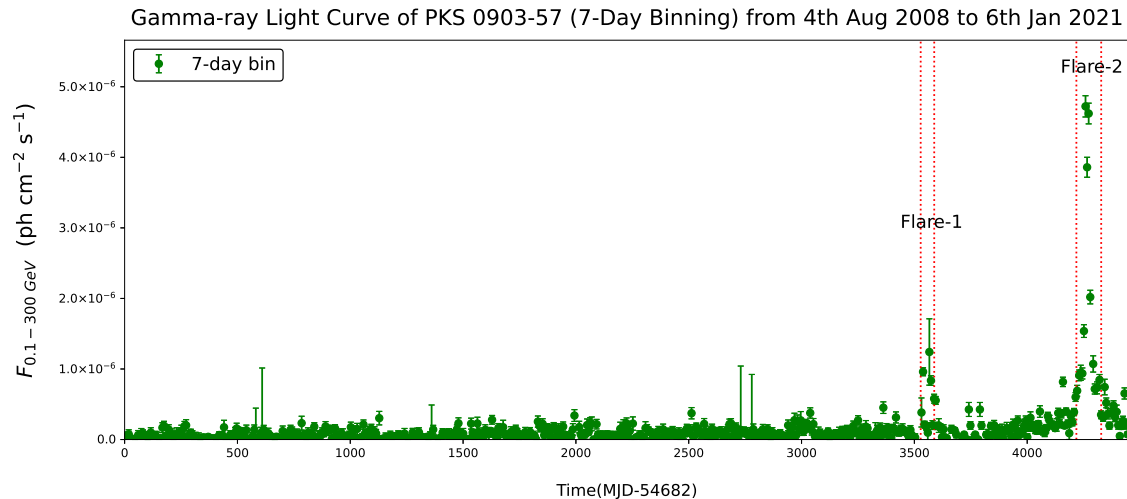


Figure 3.1. 12 years (MJD 54682.0-59220.0) γ -ray light curve of PKS 0903-57 in 7-day binning. Two flaring states Flare-1 & Flare-2 have been identified and highlighted with a pair of vertical red-dotted lines.

γ -ray light curves. If the number of data points is not sufficient it is hard to determine the position of the peak in the light curve during a flare. Hence, we have used the 3-hour binned γ -ray light curves in our study, although their data points have comparatively larger error bars in some cases.

Throughout the paper, the γ -ray fluxes have been reported in 10^{-6} $\text{ph cm}^{-2} \text{s}^{-1}$ unit (in the text; in case of figures we have mentioned the unit in the bracket).

3.4 Method of Identification of Different Activity Phases & Temporal Evolution of Gamma-Ray Light Curve during the Flares

3.4.1 Detection of Different Activity Phases

We have studied each flare and its activity states or phases (e.g. preflare, flare and postflare) separately as shown in [Figure 3.4](#), [Figure 3.8](#) & [Figure 3.9](#) for Flare-1, Flare-I & Flare-II respectively. There are several methods to define the different phases of a source. We have discussed the following two methods to define the different phases of a source.

- We have used ‘Bayesian Blocks’ method [[165](#)] to determine the flaring phases. We have applied this method to ‘Flare-1’ & ‘Flare-2’ (shown in [Figure 3.1](#); the application of this method on both of the flares has been shown separately in [Figure 3.2](#) & [Figure 3.3](#) respectively). In every case, a segment can be called ‘Flare’ when the flux value is above 5σ about the mean flux.
- Estimation of each phase’s average flux (preflare, flare, etc.) and compare

their values. If the average flux of a particular phase is more than 3-4 times of the average flux during preflare or postflare, that particular phase can be defined as ‘Flare’. We have tabulated the average γ -ray flux of different phases in Table 3.2, where we can see the average γ -ray flux of the flaring phases are 3-4 times higher than the ‘preflare’ or ‘postflare’ states.

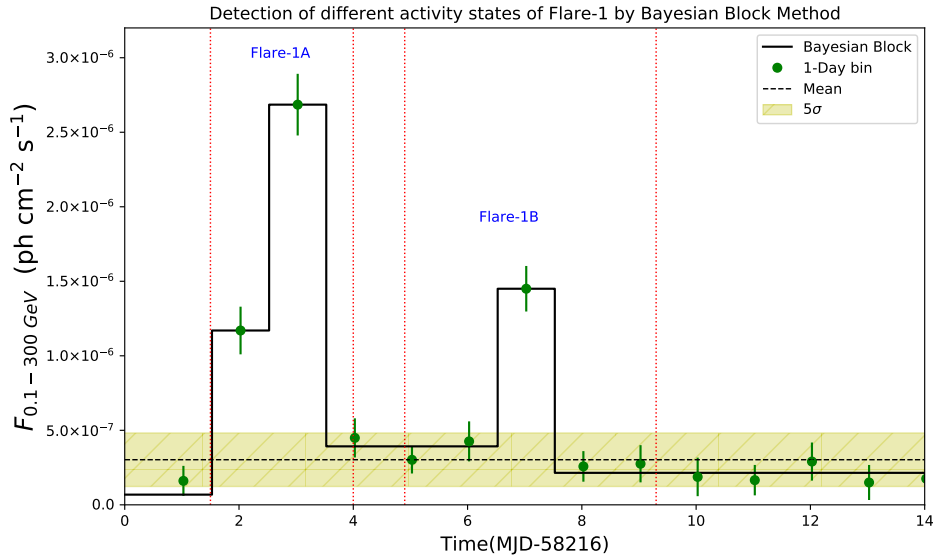


Figure 3.2. ‘Flare’ detection with the help of Bayesian Block method during ‘Flare-1’.

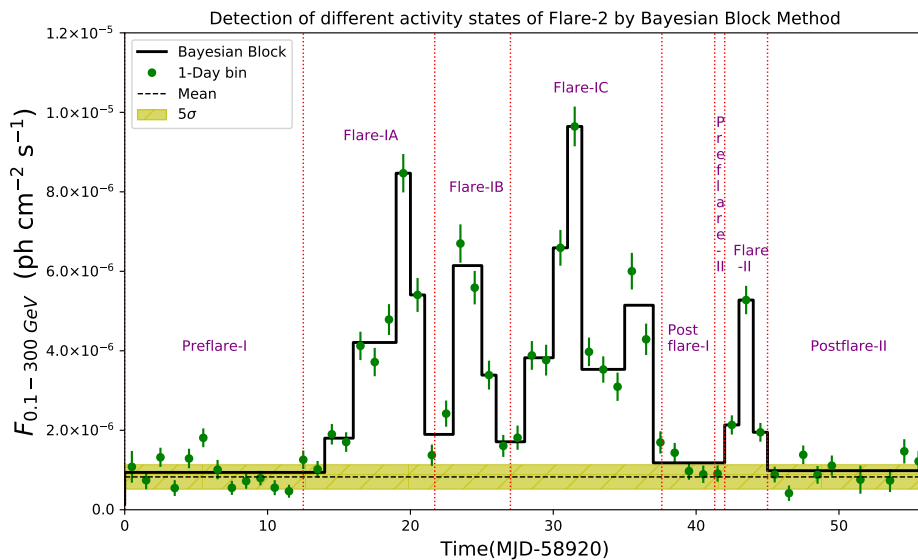


Figure 3.3. ‘Flare’ detection with the help of Bayesian Block method during ‘Flare-2’.

Table 3.2: Table of average γ -ray flux of different activity states of PKS 0903-57

Activity	Period (MJD)	Average Gamma-Ray Flux (10^{-6} ph cm $^{-2}$ s $^{-1}$)
Flare-1A	58217.5-58220.0	1.8 \pm 0.5
Flare-1B	58220.9-58225.3	0.6 \pm 0.4
Preflare-I	58920.0-58932.5	0.9 \pm 0.6
Flare-IA	58932.5-58941.7	3.6 \pm 1.0
Flare-IB	58941.7-58947.0	3.9 \pm 1.2
Flare-IC	58947.0-58957.6	4.6 \pm 1.2
Postflare-I	58957.6-58961.3	1.1 \pm 0.7
Preflare-II	58961.3-58962.0	1.2 \pm 0.6
Flare-II	58962.0-58965.0	4.6 \pm 1.0
Postflare-II	58965.0-58976.0	1.1 \pm 0.7

3.4.2 Study of Temporal Evolution of the γ -ray Flares

We have studied the temporal evolution of each flaring phases separately. Each flaring phases consists of one or more peaks and there are rising and decay time corresponding to each peak. The data points below the detection limit of 3σ ($TS < 9$) have been rejected for the temporal study. We have fitted the 3-hour binned γ -ray light curve of each flaring phases with a sum of exponential function. The functional form is given below [166]

$$F(t) = 2F_0 \left[\exp\left(\frac{t_0 - t}{T_r}\right) + \exp\left(\frac{t - t_0}{T_d}\right) \right]^{-1} \quad (3.2)$$

where, t_0 is the peak time when the γ -ray flux is highest within a specific period, F_0 is the flux observed at time t_0 also called as 'peak flux', T_r is rising time and T_d is decay time of the peak. Each of the figures (Figure 3.5, Figure 3.6, Figure 3.10, Figure 3.11, Figure 3.12, and Figure 3.13) consists of three panels; the upper panel shows the γ -ray light curve fitted with Equation 3.2, middle one shows the residual plot and the lower panel shows the TS (Test-Statistics) plot of the data points. A horizontal dark-orchid line in the upper panel has been shown in Figure 3.5, Figure 3.6, Figure 3.10, Figure 3.11, Figure 3.12, and Figure 3.13 is the baseline flux. In a few cases the light curve fittings seem to be over-fitted due to the following reasons: if the peak that we defined during a flaring phase, consists of a single data point then it is very difficult to fit that peak. Also, if the points include large error bars then the fit may be over-fitted. Both of which are true in our case. We have showed a residual plot corresponding to each fitted light curve where we have plotted time vs residue to show the quality of fitting. The

residue is defined as the ratio of the difference between model and observed flux to the flux error. It can be seen that the residual calculated for each data point is confined within $\pm 3\sigma$ confidence level. There are only very few points which are out of this zone. In case of the TS plot, we have drawn a baseline of $TS=9$ to show that the TS value of the data points are much higher than 9 i.e. they are detected with much higher confidence level, so their detection is highly significant.

3.5 Description of Flares

In this section, we have discussed about the flares in details.

3.5.1 Flare-1

Figure 3.4 shows the γ -ray light curve of Flare-1 in time bins of 1-day, 12-hour, 6-hour and 3-hour corresponding to the flaring activity of PKS 0903-57 between MJD 58216.5 to 58230. Only one sub-structure has been detected. Also phases, which can be seen in **Figure 3.4**, are prominently visible in 12-hour, 6-hour and 3-hour time bin. The flaring activity of Flare-1 can be divided into two phases: Flare-1A and Flare-1B. The γ -ray flux before Flare-1A and after Flare-1B are too low for analysis, so we have not considered any of the two regions as Preflare or Postflare. This activity was observed by Fermi-LAT [149] in May 2018.

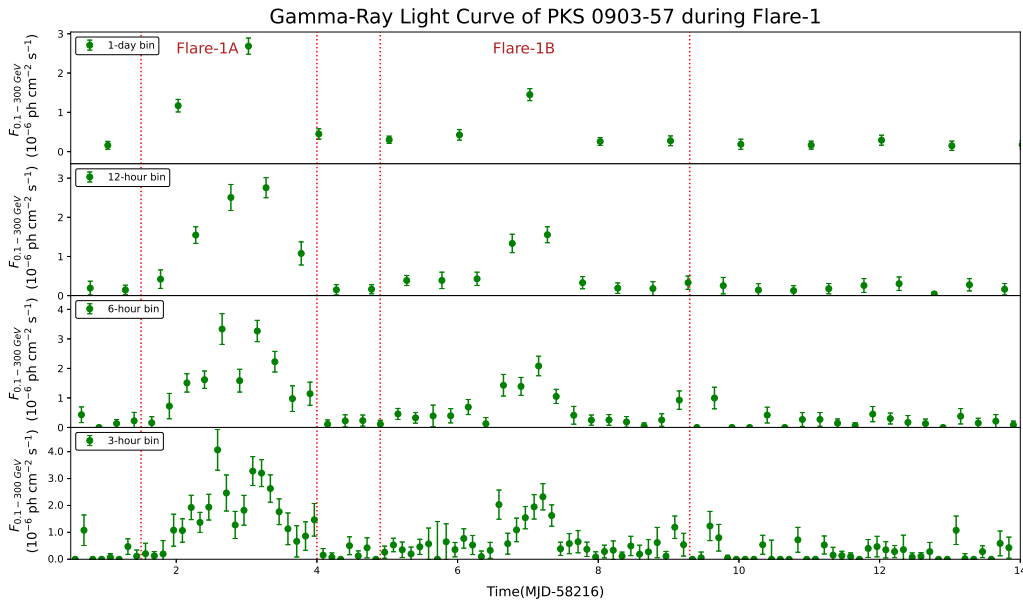


Figure 3.4. γ -ray light curve of PKS 0903-57 during Flare-1 (MJD 58216.5-58230.0) shown in **Figure 3.1**. In smaller time binning the different phases of Flare-1 are more prominent. Flare-1 has two phases: Flare-1A & Flare-1B.

We have used ‘Bayesian Block’ method to detect different activity phases as shown in **Figure 3.2**.

Flare-1A was observed between MJD 58217.5 to 58220.0, persisted for ~ 3 days.

Figure 3.5 shows the temporal evolution of γ -ray flux during Flare-1A, where we can see two major peaks: P_1 and P_2 around MJD 58218.59 and MJD 58219.08 with flux 4.06 ± 0.75 & 3.27 ± 0.53 respectively. The average γ -ray flux during this flare is 1.8 ± 0.5 . Similarly, Figure 3.6 shows the temporal evolution of γ -ray flux during Flare-1B which was observed between MJD 58220.9 to 58225.3, where we can see a single peak, P_1 at MJD 58223.28 with flux 2.32 ± 0.48 . And the average flux during this period is 0.6 ± 0.4 .

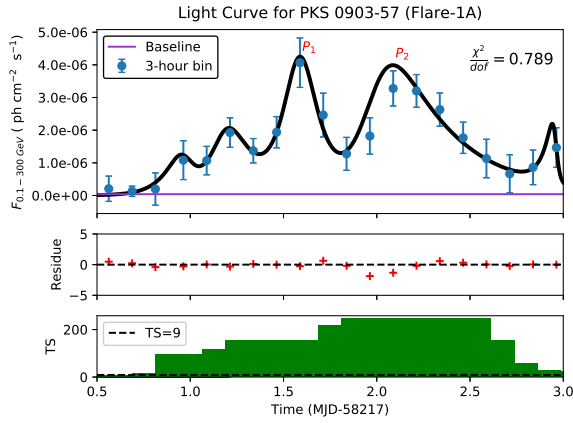


Figure 3.5. Fitted light curve with Equation 3.2 of Flare-1A (MJD 58217.5-58220.0)

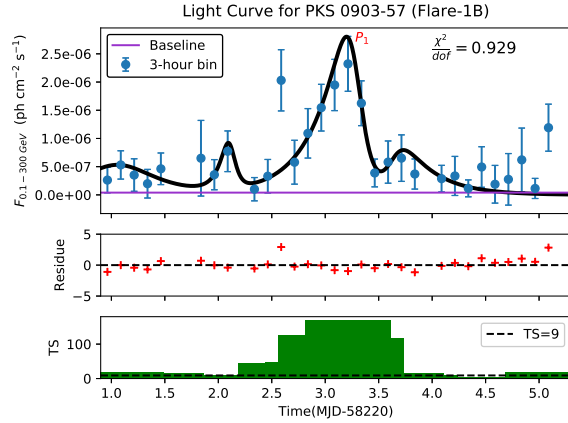


Figure 3.6. Fitted light curve with Equation 3.2 of Flare-1B (MJD 58220.9-58225.3)

The flares have been fitted with Equation 3.2. The decay time and the rising time of the peaks are tabulated in Table 3.3 and Table 3.4 for Flare-1A & Flare-1B respectively.

Table 3.3: Table of Rise & Decay time for Flare-1A

Peak	t_o (MJD)	F_o (10^{-6} ph cm $^{-2}$ s $^{-1}$)	T_r (hr)	T_d (hr)
P_1	58218.59	4.06 ± 0.75	1.8 ± 0.4	2.1 ± 0.5
P_2	58219.08	3.27 ± 0.53	2.0 ± 0.6	8.0 ± 0.7

Table 3.4: Table of Rise & Decay Time for Flare-1B

Peak	t_o (MJD)	F_o (10^{-6} ph cm $^{-2}$ s $^{-1}$)	T_r (hr)	T_d (hr)
P_1	58223.28	2.32 ± 0.48	7.0 ± 0.9	1.8 ± 0.7

3.5.2 Flare-2

From MJD 58920 to MJD 58976, another flaring activity, Flare-2, of PKS 0903-57 has been observed as shown in Figure 3.1. In shorter time binning, we have found that Flare-2 has two sub-structures, shown in Figure 3.7, denoted by Flare-I &

Flare-II. In a shorter time bin, the phases of Flare-I & Flare-II are more prominent which are shown in [Figure 3.8](#) & [Figure 3.9](#) respectively.

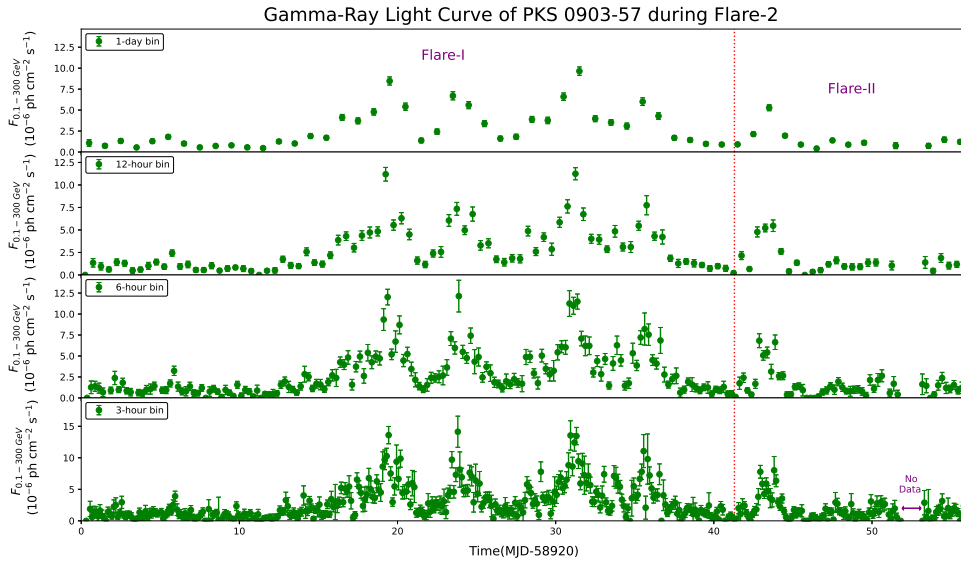


Figure 3.7. γ -ray light curve of PKS 0903-57 during Flare-2 (MJD 58920.0-58976.0). Two sub-structures of Flare-2: Flare-I & Flare-II.

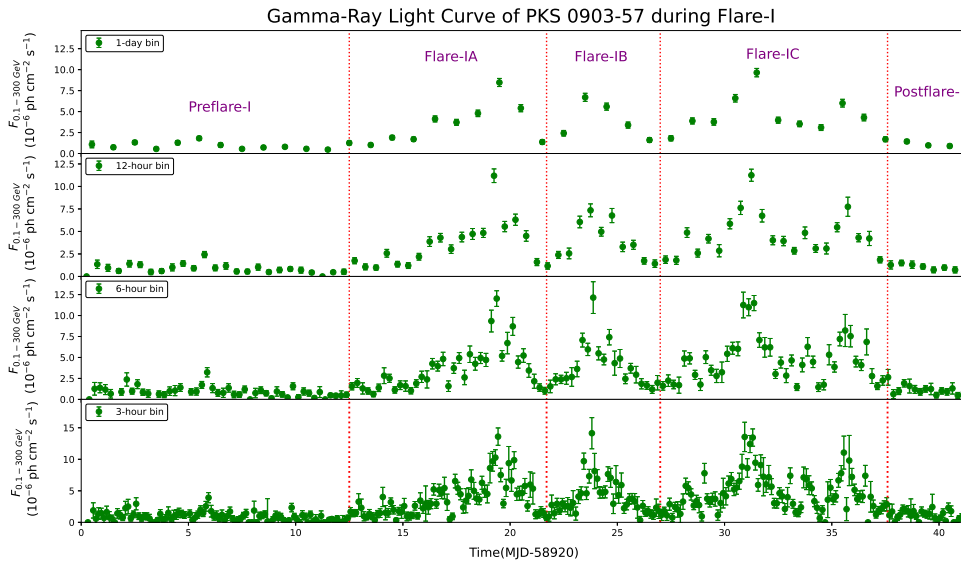


Figure 3.8. γ -ray light curve of PKS 0903-57 during Flare-I (MJD 58920.0-58961.3), sub-structure of Flare-2 shown in [Figure 3.7](#). Five phases of Flare-I: Preflare-I, Flare-IA, Flare-IB, Flare-IC & Postflare-I.

This flaring activity of PKS 0903-57 was reported (between end of March 2020 to April 2020) by Fermi-LAT [106] [151], AGILE [150], HESS [152] and DAMPE [154]. This was reported as the brightest flare ever detected by Fermi-LAT from this source.

In [Figure 3.3](#), we have shown the application of the ‘Bayesian Block’ method to detect different activity phases of Flare-2.

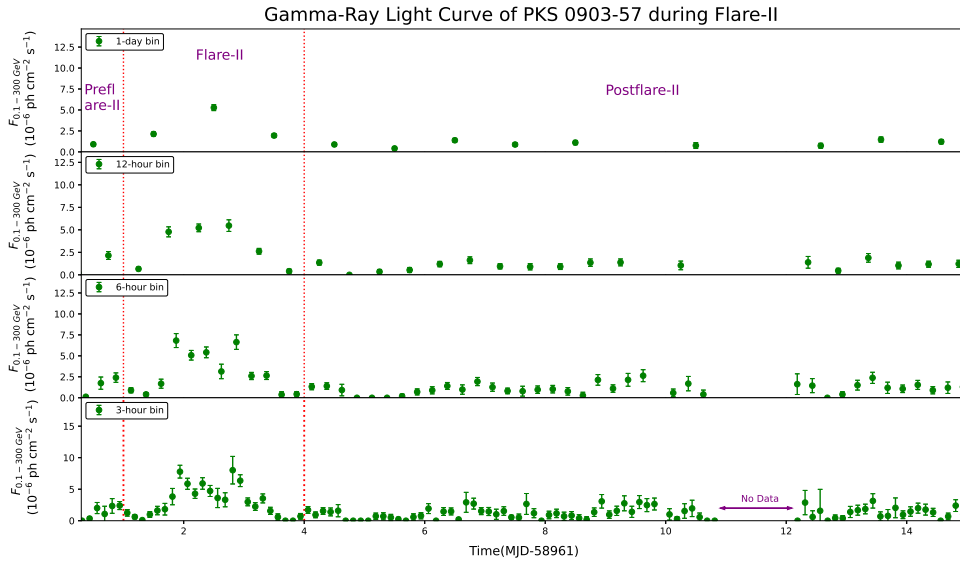


Figure 3.9. γ -ray light curve of PKS 0903-57 during Flare-II (MJD 58961.3-58976.0), sub-structure of Flare-2 shown in Figure 3.7. Three phases of Flare-II: Preflare-II, Flare-II & Postflare-II.

Flare-I has five distinct phases: Preflare-I, Flare-IA, Flare-IB, Flare-IC & Postflare-I, shown in Figure 3.8. Each region is prominently visible in the γ -ray light curve in shorter time bins.

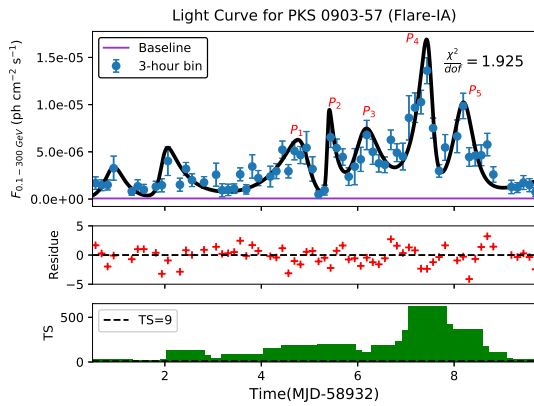


Figure 3.10. Fitted light curve with Equation 3.2 of Flare-IA (MJD 58932.5-58941.7)

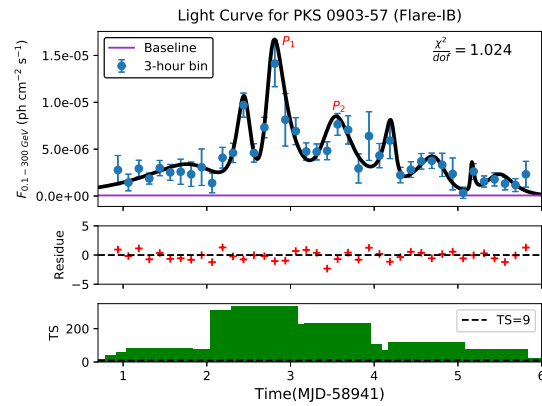


Figure 3.11. Fitted light curve with Equation 3.2 of Flare-IB (MJD 58941.7-58947.0)

Preflare-I has been observed from MJD 58920 to 58932.5, over 12 days where the γ -ray flux is very low; after this phase, a rise in the γ -ray flux has been observed. The average flux during this period is 0.9 ± 0.6 .

Preflare-I is followed by three flaring phases. These three flaring segments are Flare-IA, Flare-IB and Flare-IC respectively. Flare-IA was observed from MJD 58932.5 to 58941.7, which persisted almost for 9 days. In Figure 3.10, we can see five peaks P_1 , P_2 , P_3 , P_4 and P_5 at MJD 58936.90, 58937.38, 58938.10, 58939.50

and 58940.22 respectively and the corresponding fluxes are 5.10 ± 0.95 , 6.54 ± 1.08 , 6.77 ± 1.55 , 13.59 ± 1.37 , 9.86 ± 1.34 respectively. In [Figure 3.10](#) we have shown, fitted light curve with [Equation 3.2](#) and the decay and rising time are reported in [Table 3.5](#). The average γ -ray flux during this period is 3.6 ± 1.0 .

Flare-IB has been observed between MJD 58941.7 to 58947.0. The temporal evolution of Flare-IB has been shown in [Figure 3.11](#) with two peaks. The highest peak occurred at MJD 58943.76 with the flux 14.13 ± 2.46 , denoted as P_1 and the second peak, P_2 is observed at MJD 58944.50 with flux 7.64 ± 1.16 . The decay and rise time corresponding to P_1 and P_2 are mentioned in [Table 3.6](#). The average γ -ray flux during this period is 3.9 ± 1.2 .

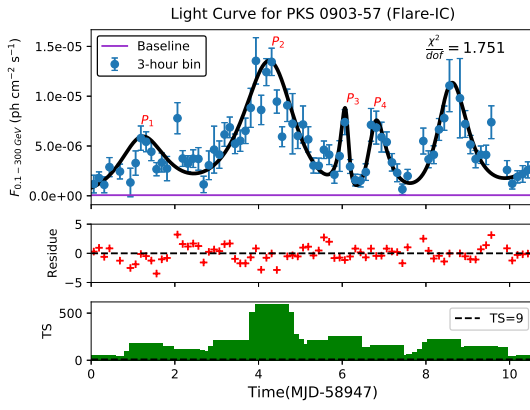


Figure 3.12. Fitted light curve with [Equation 3.2](#) of Flare-IC (MJD 58947.0-58957.6)

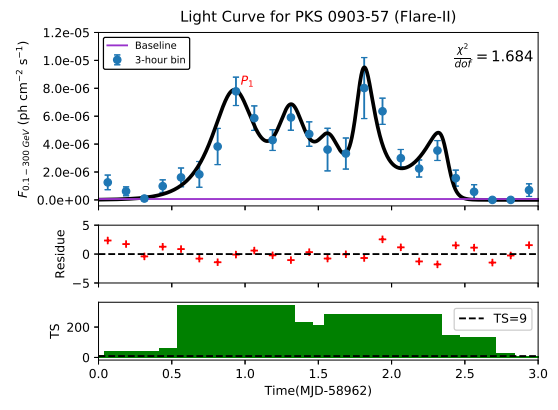


Figure 3.13. Fitted light curve with [Equation 3.2](#) of Flare-II (MJD 58962.0-58965.0)

Flare-IC has been observed between MJD 58947.0 to 58957.6. This phase persisted almost for 10 days. [Figure 3.12](#) shows four peaks P_1, P_2, P_3 and P_4 at MJD 58948.19, 58951.31, 58953.10 and 58953.75 respectively and corresponding γ -ray fluxes are 5.78 ± 1.22 , 13.44 ± 1.37 , 7.39 ± 1.25 and 6.84 ± 1.65 respectively. The decay and rise time are tabulated in the [Table 3.7](#). The average γ -ray flux in this phase is 4.6 ± 1.2 .

Table 3.5: Table of Rise & Decay Time for Flare-IA

Peak	t_o (MJD)	F_o (10^{-6} ph cm $^{-2}$ s $^{-1}$)	T_r (hr)	T_d (hr)
P_1	58936.90	5.10 ± 0.95	13.4 ± 1.8	3.0 ± 0.9
P_2	58937.38	6.54 ± 1.08	0.5 ± 0.3	3.9 ± 1.5
P_3	58938.10	6.77 ± 1.55	3.8 ± 2.0	8.2 ± 1.9
P_4	58939.50	13.59 ± 1.37	5.8 ± 1.1	1.6 ± 0.4
P_5	58940.22	9.86 ± 1.34	5.0 ± 2.0	4.3 ± 1.8

A postflare phase (Postflare-I) is observed between MJD 58957.6 to 58961.3 with the average flux 1.1 ± 0.7 . Just after the Postflare-I, a rise in the γ -ray flux

Table 3.6: Table of Rise & Decay Time for Flare-IB

Peak	t_o (MJD)	F_o (10^{-6} ph cm $^{-2}$ s $^{-1}$)	T_r (hr)	T_d (hr)
P_1	58943.76	14.13±2.46	1.4±0.3	4.4±0.6
P_2	58944.50	7.64±1.16	2.8±0.8	5.4±1.4

Table 3.7: Table of Rise & Decay Time for Flare-IC

Peak	t_o (MJD)	F_o (10^{-6} ph cm $^{-2}$ s $^{-1}$)	T_r (hr)	T_d (hr)
P_1	58948.19	5.78±1.22	7.7±1.5	9.2±1.8
P_2	58951.31	13.44±1.37	15.2±1.3	11.8±1.2
P_3	58953.10	7.39±1.25	3.0±1.0	1.3±0.4
P_4	58953.75	6.84±1.65	2.9±0.8	6.7±1.1

Table 3.8: Table of Rise & Decay Time for Flare-II

Peak	t_o (MJD)	F_o (10^{-6} ph cm $^{-2}$ s $^{-1}$)	T_r (hr)	T_d (hr)
P_1	58962.94	7.78±1.01	3.2±0.5	3.0±1.4

is seen between MJD 58961.3 to 58976.0. This state is defined as Flare-II and the corresponding γ -ray light curve is shown in [Figure 3.9](#). The γ -ray light curves in 1-day, 12-hour, 6-hour and 3-hour time bin have been shown here. This flare consists of three phases: Preflare-II, Flare-II and Postflare-II. The preflare phase lasted for only 1.3 days (MJD 58961.3 to 58962.0); during this period, the average γ -ray flux is found to be 1.2 ± 0.6 . Preflare-II is followed by a flaring phase (Flare-II; MJD 58962.0 to 58965.0) which is also very short (~ 2 days). In [Figure 3.13](#), we have shown the flare in 3-hour time bin, with a single peak P_1 observed at MJD 58962.94 with flux value 7.78 ± 1.01 . The decay and rise time are mentioned in [Table 3.8](#). The average γ -ray flux during this period is 4.6 ± 1.0 .

After the flaring phase, Postflare-II is observed between MJD 58965.0 to 58976.0 with an average flux 1.1 ± 0.7 .

3.5.3 Variability Time

Variability time is a measure of the time scale of flux variation during flares.

$$F(t_2) = F(t_1)2^{\frac{t_2-t_1}{T_{d/h}}} \quad (3.3)$$

where, $F(t_1)$ and $F(t_2)$ are the fluxes measured at two consecutive time instants t_1 and t_2 respectively, $T_{d/h}$ denotes flux doubling or halving time which is tabulated in [Table 3.9](#) ('positive' and 'negative' value of $T_{d/h}$ in the table denotes doubling and halving time respectively). Two criteria have been kept in mind during the

Table 3.9: Table for γ -ray flux doubling/halving time ($T_{d/h}$) for each flare

$T_{\text{start}}(t_1)$ (MJD)	$T_{\text{stop}}(t_2)$ (MJD)	$\text{Flux}_{\text{start}}[F(t_1)]$ (10^{-6} ph cm $^{-2}$ s $^{-1}$)	$\text{Flux}_{\text{stop}}[F(t_2)]$ (10^{-6} ph cm $^{-2}$ s $^{-1}$)	$T_{d/h}$ (hr)	$\Delta t_{d/h}$ (hr)	Rise/ Decay
Flare-1						
58218.463	58218.588	1.93±0.47	4.06±0.75	2.8±1.2	1.6±0.7	R
Flare-I						
58922.438	58922.563	1.26±0.53	2.94±0.95	2.5±1.6	1.5±0.9	R
58934.313	58934.438	1.51±0.68	3.19±0.67	2.8±1.9	1.6±1.1	R
58935.563	58935.688	2.61±0.68	1.02±0.50	-2.2±1.3	-1.3±0.8	D
58935.688	58935.813	1.02±0.50	3.45±1.23	1.7±0.9	1.0±0.5	R
58939.563	58939.688	7.50±1.07	2.97±0.66	-2.2±0.6	-1.3±0.4	D
58940.188	58940.313	9.86±1.34	4.45±0.98	-2.6±0.8	-1.5±0.5	D
58940.688	58940.813	5.77±1.18	2.60±0.82	-2.6±1.2	-1.5±0.7	D
58940.813	58940.938	2.60±0.82	5.98±2.01	2.5±1.4	1.5±0.8	R
58943.313	58943.438	4.60±1.03	9.69±1.28	2.8±1.0	1.6±0.6	R
58943.438	58943.563	9.69±1.28	4.60±0.98	-2.8±0.9	-1.6±0.6	D
58945.188	58945.313	5.91±1.91	2.23±0.82	-2.1±1.1	-1.3±0.6	D
58949.063	58949.188	7.78±1.56	3.74±0.79	-2.8±1.1	-1.7±0.7	D
58953.063	58953.188	7.39±1.25	2.94±0.69	-2.2±0.7	-1.3±0.4	D
58953.563	58953.688	2.37±0.83	7.12±1.64	1.9±0.7	1.1±0.4	R
Flare-II						
58962.688	58962.813	1.82±0.92	3.82±1.29	2.8±2.3	1.7±1.4	R
58962.813	58962.938	3.82±1.29	7.78±1.01	2.9±1.5	1.7±0.9	R
58963.688	58963.813	3.32±1.11	8.01±2.18	2.4±1.2	1.4±0.7	R
58963.938	58964.063	6.35±0.93	2.99±0.62	-2.8±0.9	-1.6±0.6	D
58964.313	58964.438	3.53±0.71	1.56±0.57	-2.5±1.3	-1.5±0.8	D

Notes: $\Delta t_{d/h}$ is redshift corrected doubling/halving time. 'R' denotes 'rising part' & 'D' denotes 'decay part'.

scanning of the γ -ray light curve [167] :

- Only those consecutive time instants will be considered which have $TS > 25$ ($> 5\sigma$ detection; [168]).
- The flux ratio between these two time instants should be greater than two (rising part) or less than half (decaying part).

There are several consecutive time instants with flux ratio more than two or less than half but the TS value of those observations are less than 25, we have not included these cases.

In our 12 years γ -ray light curve study, the shortest γ -ray flux doubling/halving

time ($T_{d/h}$) is found to be 1.7 ± 0.9 hour (highlighted in '*italic*' font in [Table 3.9](#), during Flare-I for MJD 58935.688 & 58935.813).

3.6 Gamma- Ray Spectral Energy Distribution of different flaring phases

We have fitted different phases (e.g. preflare, flare, postflare) of the activity periods with four different spectral models. The details about the models are the following:

1. PowerLaw (PL) :

The functional form of the powerlaw is the following,

$$\frac{dN}{dE} = N_0 \left(\frac{E}{E_0} \right)^{-\Gamma} \quad (3.4)$$

where, N_0 is the prefactor, Γ is the powerlaw index and E_0 is the scaling factor or pivot energy. We have kept a fixed value of E_0 which is 1155.4126 MeV [147] for all the γ -ray SEDs of this source.

2. LogParabola (LP) :

The functional form of the logparabola is the following,

$$\frac{dN}{dE} = N_0 \left(\frac{E}{E_0} \right)^{-(\alpha + \beta \log(E/E_0))} \quad (3.5)$$

where, N_0 is the prefactor, α is photon index, β is curvature index. Scaling factor (E_0) is fixed to 1155.4126 MeV similar to the powerlaw function.

3. BrokenPowerLaw (BPL) :

The functional form of the brokenpowerlaw is the following,

$$\frac{dN}{dE} = N_0 \begin{cases} \left(\frac{E}{E_b} \right)^{-\Gamma_1}, & \text{for } E < E_b \\ \left(\frac{E}{E_b} \right)^{-\Gamma_2}, & \text{otherwise} \end{cases} \quad (3.6)$$

where, N_0 is prefactor, Γ_1 and Γ_2 are spectral indices, E_b is the break energy.

4. PowerLaw with Exponential Cutoff (PLEC) :

The functional form of the PLEC is the following,

$$\frac{dN}{dE} = N_0 \left(\frac{E}{E_0} \right)^{-\Gamma_{PLEC}} \exp\left(- \left(\frac{E}{E_c} \right) \right) \quad (3.7)$$

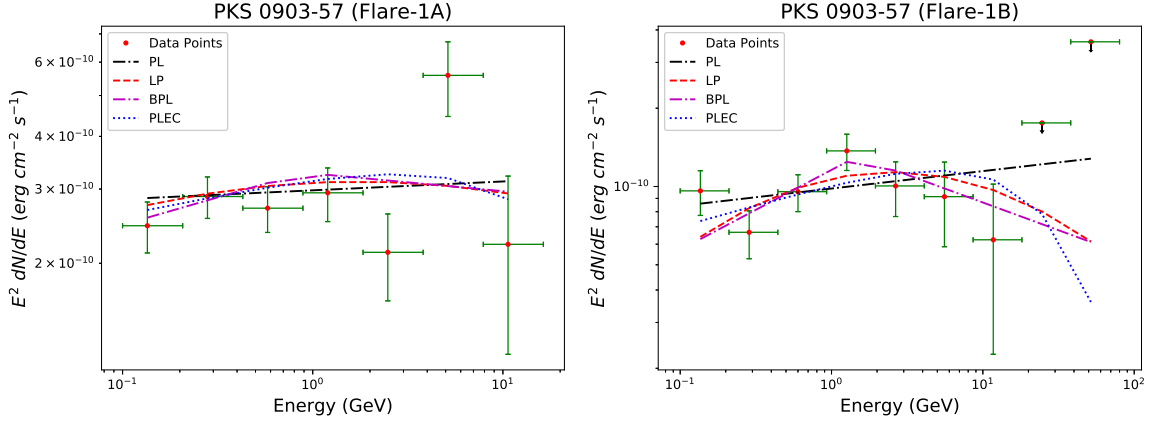


Figure 3.14. γ -ray SEDs during Flare-1A & Flare-1B of Flare-1 as shown in [Figure 3.4](#). PowerLaw (PL), LogParabola (LP), BrokenPowerLaw (BPL) and PowerLaw with Exponential Cutoff (PLEC) models used to fit the γ -ray data points.

where, N_0 is prefactor, Γ_{PLEC} is the PLEC index, E_0 is pivot energy which is fixed at 1155.4126 MeV similar to powerlaw and E_c is cutoff energy.

We have used the maximum likelihood fitting to determine the best-fit model. In [Figure 3.14](#), we have shown Fermi-LAT SEDs of Flare-1 for its two sub-structures: Flare-1A & Flare-1B. Both the SEDs have been fitted with four spectral models: PowerLaw (PL), LogParabola(LP), BrokenPowerLaw(BPL) & PowerLaw with Exponential Cutoff (PLEC). Black, red, magenta & blue color have been used to denote the fitting of the spectral points with PL, LP, BPL & PLEC respectively.

[Table 3.10](#) contains all the parameter values that have been used to fit the Fermi-LAT γ -ray spectral points of Flare-1A & Flare-1B with the above mentioned spectral models. In this table, we have mentioned the fitted flux, spectral indices, TS and $-\log(\text{Likelihood})$ values.

We have also calculated the $\Delta\log(\text{Likelihood})$ value [169] which is defined as $\Delta\log(\text{Likelihood}) = (-\log(\text{Likelihood})_{LP/BPL/PLEC}) - (-\log(\text{Likelihood})_{PL})$.

In [Figure 3.15](#), we have shown Fermi-LAT γ -ray SEDs of the five phases of Flare-I. Similarly, all the SEDs have been fitted with the same four spectral models and the fitted parameter values are tabulated in [Table 3.11](#).

In [Figure 3.16](#), SEDs of three activity phases of Flare-II have been shown, which are fitted with the same four spectral models i.e. PL, LP, BPL & PLEC and [Table 3.12](#) contains all the fitted parameter values.

In case of Flare-1, as the source transits from Flare-1A ($\Gamma=1.98\pm0.05$) to Flare-1B ($\Gamma=1.93\pm0.07$), the γ -ray spectral index remains almost constant.

Flare-I shows spectral hardening when the source transits from Preflare-I ($\Gamma=2.08\pm0.06$) to Flare-IA ($\Gamma=1.91\pm0.02$) which can be seen from [Table 3.11](#). However, during the transition from Flare-IA ($\Gamma=1.91\pm0.02$) to Flare-IB ($\Gamma=1.94\pm0.03$)

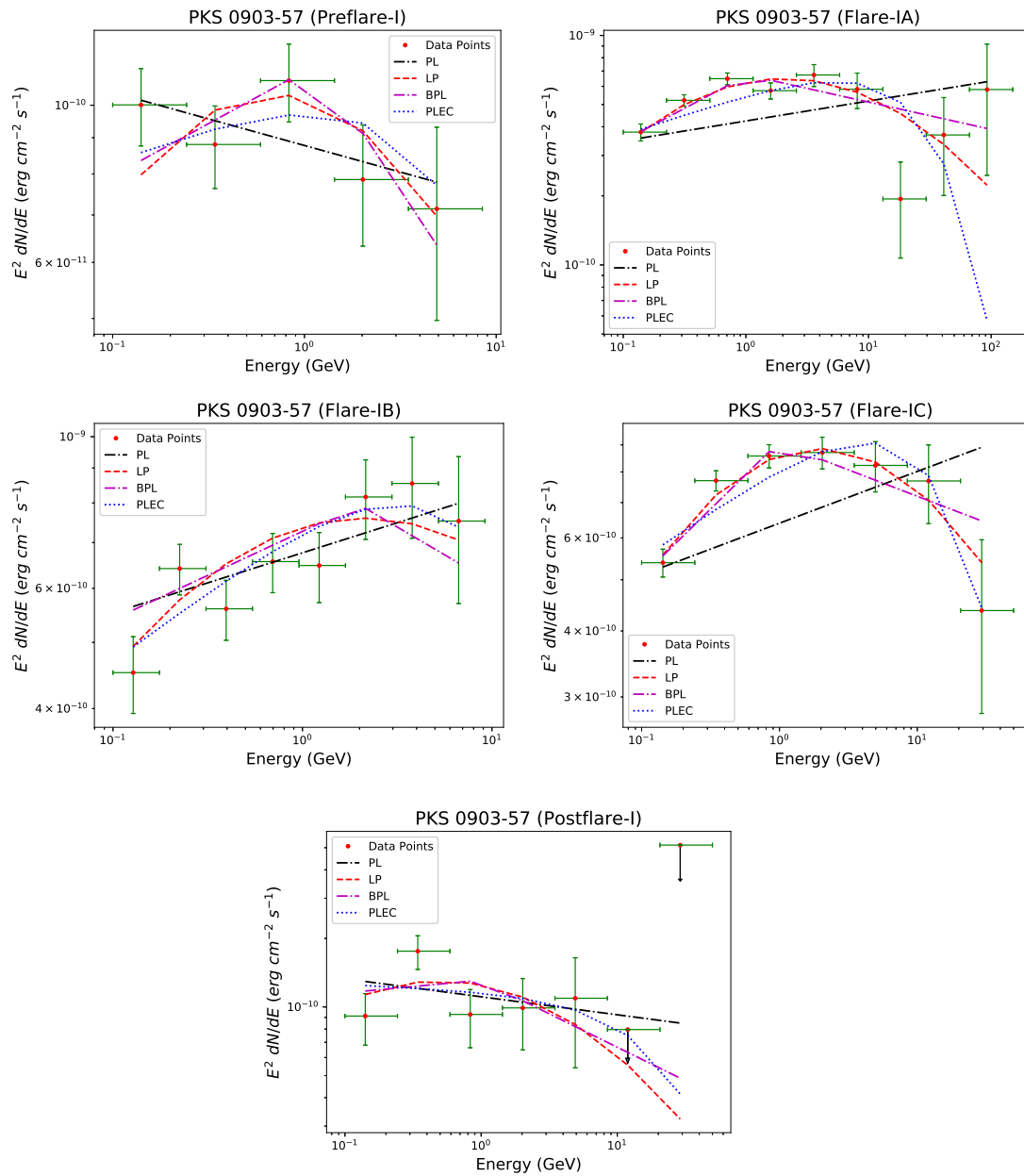


Figure 3.15. γ -ray SEDs of five activity phases of Flare-I as shown in Figure 3.8. SEDs have been fitted with four spectral models mentioned earlier.

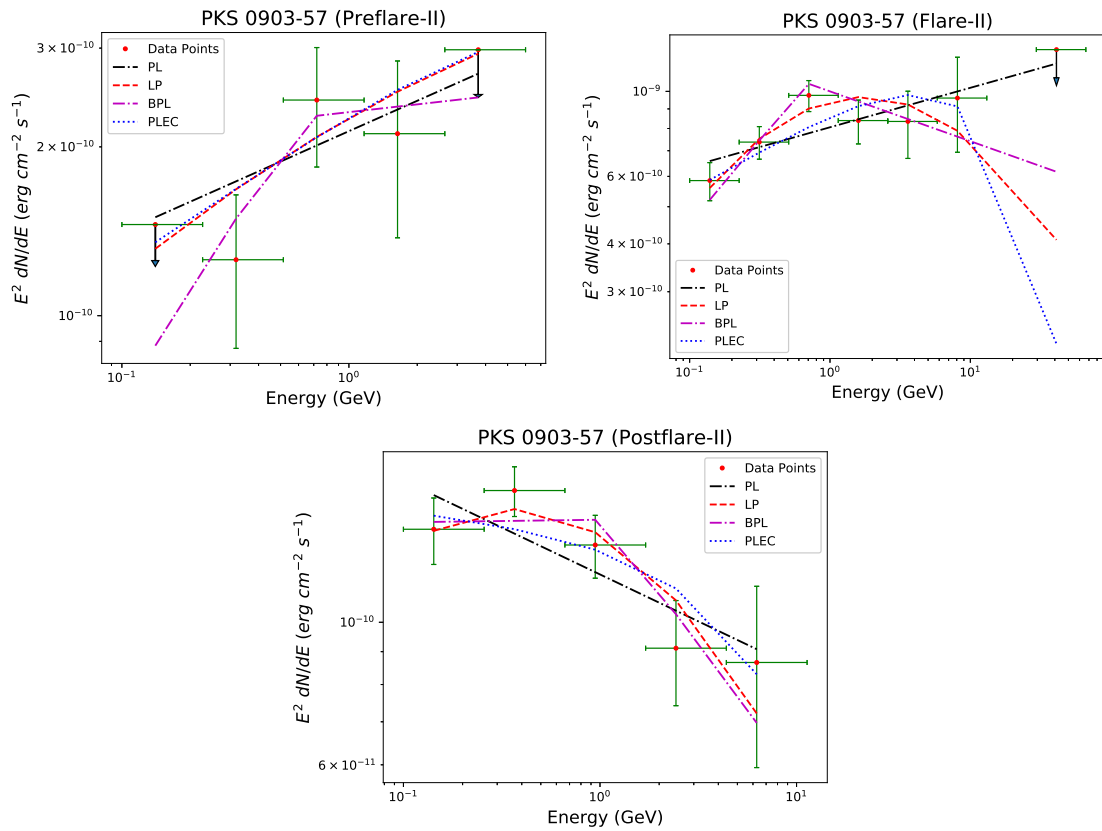


Figure 3.16. γ -ray SEDs of three activity phases of Flare-II as shown in Figure 3.9. SEDs have been fitted with the four spectral models mentioned earlier.

Table 3.10: Results of Fermi-LAT SEDs of Flare-1, fitted with different spectral model e.g. PL, LP, BPL and PLEC

PowerLaw (PL)						
Activity	$F_{0.1-300 \text{ GeV}}$ ($10^{-6} \text{ ph cm}^{-2} \text{ s}^{-1}$)	Index (Γ)	TS	-log(Likelihood)		
Flare-1A	1.76±0.12	1.98±0.05	1288.42	14395.21		
Flare-1B	0.56±0.06	1.93±0.07	661.70	34126.0		

LogParabola (LP)						
Activity	$F_{0.1-300 \text{ GeV}}$ ($10^{-6} \text{ ph cm}^{-2} \text{ s}^{-1}$)	α	β	TS	-log(Likelihood)	$\Delta \log(\text{Likelihood})$
Flare-1A	1.73±0.14	1.98±0.05	0.04± 0.02	1285.61	14394.96	-0.25
Flare-1B	0.48±0.08	1.90±0.08	0.07±0.05	652.83	34124.99	-1.02

BrokenPowerLaw (BPL)							
Activity	$F_{0.1-300 \text{ GeV}}$ ($10^{-6} \text{ ph cm}^{-2} \text{ s}^{-1}$)	Γ_1	Γ_2	E_b (GeV)	TS	-log(Likelihood)	$\Delta \log(\text{Likelihood})$
<i>Flare-1A</i>	<i>1.65±0.11</i>	<i>1.87±0.05</i>	<i>2.04±0.07</i>	<i>0.90±0.02</i>	<i>1292.18</i>	<i>14386.14</i>	<i>-9.07</i>
<i>Flare-1B</i>	<i>0.48±0.16</i>	<i>1.69±0.34</i>	<i>2.21±0.23</i>	<i>1.47±0.76</i>	<i>654.10</i>	<i>34123.84</i>	<i>-2.17</i>

PL Exp Cutoff (PLEC)						
Activity	$F_{0.1-300 \text{ GeV}}$ ($10^{-6} \text{ ph cm}^{-2} \text{ s}^{-1}$)	Γ_{PLEC}	E_c (GeV)	TS	-log(Likelihood)	$\Delta \log(\text{Likelihood})$
Flare-1A	1.71±0.13	1.91±0.06	29.88±12.97	1284.82	14394.00	-1.21
Flare-1B	0.52±0.06	1.83±0.07	29.99±0.76	656.28	34125.73	-0.28

Notes: Here we have mentioned the fitted flux and spectral indices. We have also mentioned the goodness of unbinned fits by $-\log(\text{Likelihood})$ value and evaluate $\Delta \log(\text{Likelihood})$ value, where $\Delta \log(\text{Likelihood}) = (-\log(\text{Likelihood})_{LP/BPL/PLEC}) - (-\log(\text{Likelihood})_{PL})$. The best-fitted models are highlighted in ‘*italic*’ font.

& Flare-IB ($\Gamma=1.94\pm 0.03$) to Flare-IC ($\Gamma=1.90\pm 0.02$), the spectral index remains almost constant. The spectrum softens when the source transits from Flare-IC ($\Gamma=1.90\pm 0.02$) to Postflare-I ($\Gamma=2.08\pm 0.10$). For Flare-II, the spectrum softens as the source transits from Preflare-II ($\Gamma=1.80\pm 0.10$) to Flare-II ($\Gamma=1.92\pm 0.03$).

From the above γ -ray SED analysis of the source PKS 0903-57, we can see that the γ -ray spectrum may harden or soften or remain almost unchanged during transition from one phase to another. Earlier, Das *et al.* [170] found spectral hardening as an important feature of the source 3C 454.3. However, we observed all the possibilities for the source PKS 0503-57, in some cases we saw “brighter-when-harder”, in some cases “brighter-when-softer” scenario, and in some other cases spectral index remains almost unchanged.

From the maximum likelihood analysis using different spectral models during the different activity phases, we find that BPL is the best-fit model for Flare-1 & Flare-II, whereas LP is the best-fit model for Flare-I. We have multi-wavelength data for only these four phases: Flare-1B, Flare-1A, Flare-1B & Flare-1C. For three

Table 3.11: Results of Fermi-LAT SEDs of Flare-I, fitted with different spectral model e.g. PL, LP, BPL and PLEC

PowerLaw (PL)						
Activity	$F_{0.1-300 \text{ GeV}}$ ($10^{-6} \text{ ph cm}^{-2} \text{ s}^{-1}$)	Index (Γ)	TS	-log(Likelihood)		
Preflare-I	0.56 ± 0.05	2.08 ± 0.06	690.73	47426.03		
Flare-IA	3.02 ± 0.11	1.91 ± 0.02	4980.58	30625.17		
Flare-IB	3.86 ± 0.16	1.94 ± 0.03	3196.55	19383.86		
Flare-IC	4.34 ± 0.12	1.90 ± 0.02	8505.55	43270.09		
Postflare-I	0.77 ± 0.11	2.08 ± 0.10	258.35	11551.58		

LogParabola (LP)						
Activity	$F_{0.1-300 \text{ GeV}}$ ($10^{-6} \text{ ph cm}^{-2} \text{ s}^{-1}$)	α	β	TS	-log(Likelihood)	$\Delta \log(\text{Likelihood})$
Preflare-I	0.50 ± 0.01	2.11 ± 0.00	0.11 ± 0.00	712.46	47412.73	-13.30
Flare-IA	2.78 ± 0.12	1.91 ± 0.03	0.07 ± 0.02	4956.73	30613.75	-11.42
Flare-IB	3.51 ± 0.17	1.93 ± 0.04	0.06 ± 0.02	3055.13	19372.94	-10.92
Flare-IC	4.12 ± 0.12	1.93 ± 0.02	0.07 ± 0.01	8478.70	43257.17	-12.92
Postflare-I	0.72 ± 0.12	2.14 ± 0.12	0.08 ± 0.07	259.05	11550.82	-0.76

BrokenPowerLaw (BPL)							
Activity	$F_{0.1-300 \text{ GeV}}$ ($10^{-6} \text{ ph cm}^{-2} \text{ s}^{-1}$)	Γ_1	Γ_2	E_b (GeV)	TS	-log(Likelihood)	$\Delta \log(\text{Likelihood})$
Preflare-I	0.50 ± 0.14	1.85 ± 0.32	2.41 ± 0.22	1.16 ± 0.49	686.42	47423.08	-2.95
Flare-IA	2.80 ± 0.15	1.72 ± 0.06	2.12 ± 0.06	1.03 ± 0.18	4954.03	30614.38	-10.79
Flare-IB	3.78 ± 0.17	1.87 ± 0.04	2.16 ± 0.11	2.00 ± 0.00	3201.32	19381.47	-2.39
Flare-IC	4.14 ± 0.12	1.74 ± 0.04	2.10 ± 0.05	0.98 ± 0.09	8481.95	43257.18	-12.91
Postflare-I	0.74 ± 0.25	1.94 ± 0.43	2.29 ± 0.30	1.00 ± 0.68	258.46	11551.07	-0.31

PL Exp Cutoff (PLEC)						
Activity	$F_{0.1-300 \text{ GeV}}$ ($10^{-6} \text{ ph cm}^{-2} \text{ s}^{-1}$)	Γ_{PLEC}	E_c (GeV)	TS	-log(Likelihood)	$\Delta \log(\text{Likelihood})$
Preflare-I	0.52 ± 0.03	1.89 ± 0.03	9.64 ± 1.78	712.33	47416.66	-9.37
Flare-IA	2.90 ± 0.11	1.82 ± 0.03	30.00 ± 0.03	4961.45	30620.54	-4.63
Flare-IB	3.75 ± 0.16	1.84 ± 0.05	17.98 ± 7.06	3205.43	19379.42	-4.44
Flare-IC	4.22 ± 0.12	1.82 ± 0.03	23.38 ± 6.20	8494.66	43261.78	-8.31
Postflare-I	0.76 ± 0.11	2.02 ± 0.10	30.00 ± 1.83	258.11	11551.48	-0.10

Table 3.12: Results of Fermi-LAT SEDs of Flare-II, fitted with different spectral model e.g. PL, LP, BPL, PLEC

PowerLaw (PL)							
Activity	$F_{0.1-300 \text{ GeV}}$ ($10^{-6} \text{ ph cm}^{-2} \text{ s}^{-1}$)	Index (Γ)	TS	-log(Likelihood)			
Preflare-II	0.92±0.15	1.82±0.10	232.32	10495.42			
Flare-II	3.19±0.16	1.92±0.03	2288.81	15193.42			
Postflare-II	0.91±0.06	2.15±0.05	1166.98	49385.92			

LogParabola (LP)						
Activity	$F_{0.1-300 \text{ GeV}}$ ($10^{-6} \text{ ph cm}^{-2} \text{ s}^{-1}$)	α	β	TS	-log(Likelihood)	$\Delta \log(\text{Likelihood})$
Preflare-II	0.85 ± 0.02	1.78±0.01	0.02±0.01	244.00	10450.08	-45.34
Flare-II	3.01±0.16	1.94±0.04	0.08±0.02	2302.13	15186.76	-6.66
Postflare-II	0.84±0.07	2.21±0.06	0.09±0.04	1156.62	49376.90	-9.02

BrokenPowerLaw (BPL)							
Activity	$F_{0.1-300 \text{ GeV}}$ ($10^{-6} \text{ ph cm}^{-2} \text{ s}^{-1}$)	Γ_1	Γ_2	E_b (GeV)	TS	-log(Likelihood)	$\Delta \log(\text{Likelihood})$
Preflare-II	0.78±0.00	1.36±0.00	1.95±0.00	0.61±0.00	244.93	10449.71	-45.71
Flare-II	2.99±0.16	1.62±0.11	2.13±0.08	0.65±0.20	2304.57	15185.54	-7.88
Postflare-II	0.86±0.07	2.00±0.08	2.41±0.13	1.07±0.11	1158.88	49377.54	-8.38

PL Exp Cutoff (PLEC)						
Activity	$F_{0.1-300 \text{ GeV}}$ ($10^{-6} \text{ ph cm}^{-2} \text{ s}^{-1}$)	Γ_{PLEC}	E_c (GeV)	TS	-log(Likelihood)	$\Delta \log(\text{Likelihood})$
Preflare-II	0.88±0.15	1.72±0.11	30.00±0.03	228.14	10497.51	2.09
Flare-II	3.11±0.16	1.83±0.05	26.53±12.49	2296.64	15189.51	-3.91
Postflare-II	0.87±0.06	2.03±0.08	13.94±8.04	1163.43	49377.84	-8.08

of them (Flare-IA, Flare-IB & Flare-IC) LP is the best-fit model. However, in case of Flare-1B the $\Delta \log(\text{Likelihood})$ values for LP and BPL are very close to each other (see Table 3.10). Hence both models are preferred. Therefore, we have used LP model to fit the multi-wavelength SEDs of all the four phases in this work.

3.7 Multi-Wavelength Study of PKS 0903-57

In this section, we have discussed multi-wavelength study of the source PKS 0903-57. From the γ -ray light curve we have detected different phases of the source. Then we have searched for multi-wavelength data for this source. Here, we have used X-ray, ultraviolet (UV) and optical data from Swift XRT and UVOT (Ultraviolet/Optical telescope) respectively and radio data collected by ATCA [153]. Only Flare-1B, Flare-IA, Flare-IB and Flare-IC have simultaneous multi-waveband data corresponding to their γ -ray flaring activity which only spans 4.4 days, 9.2 days, 5.3 days and 10.6 days respectively. Moreover, the number of observations is few in Swift XRT and Swift UVOT.

3.7.1 Multi-Wavelength Light Curve of PKS 0903-57

Figure 3.17 shows the multi-wavelength light curve of the source PKS 0903-57 during Flare-1. Simultaneous multi-wavelength data is only available for Flare-1B, one of the phases of Flare-1, corresponding to MJD 58220.9 to 58225.3 with a period of 4.4 days. In the same plot, We can see that there is no multi-wavelength data corresponding to the γ -ray light curve of Flare-1A. In the uppermost panel of the plot, 6-hour binned γ -ray data has been plotted. X-ray, Optical and UV data have been shown in the following panels i.e. in the second, third and fourth panels respectively. We could not get radio data or any data in other wavebands from any other instruments corresponding to Flare-1B. The number of observations in X-ray to Optical is very low to fit the X-ray to Optical light curve and calculate the variability time in X-ray to Optical wavebands.

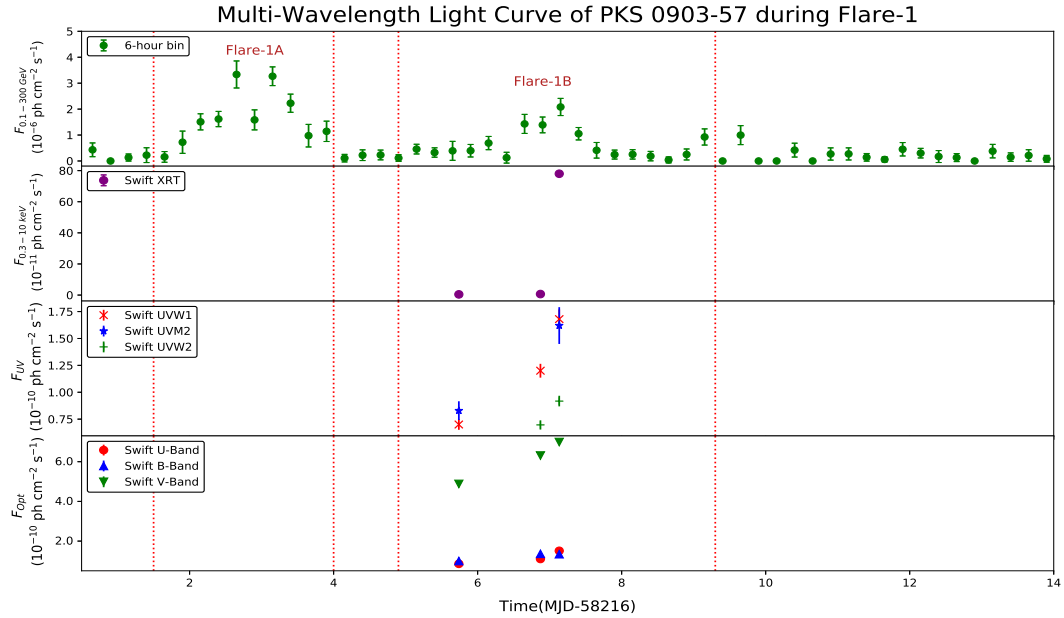


Figure 3.17. Multi-Wavelength light curve of PKS 0903-57 during Flare-1. The ‘green solid circle’ denotes Fermi-LAT data points in 6-hour bin. Others are mentioned in the plots. Ultra-Violet data points are in W1, M2 & W2 bands and Optical data points are in U, V & B bands.

In **Figure 3.18**, we have shown multi-wavelength light curve for Flare-I (MJD 58920.0-58961.3). We have simultaneous multi-wavelength data corresponding to Flare-IA, Flare-IB and Flare-IC i.e. MJD 58932.5-58957.6. Similarly, 6-hour binned γ -ray light curve has been shown in the uppermost panel of the plot, followed by X-ray, Optical and UV data in the following panels.

In Swift XRT/UVOT we get 15 simultaneous observations corresponding to the flaring states observed in γ -ray. Out of 15; 3 observations correspond to Flare-1B, 3 observations correspond to Flare-IA, another 3 observations correspond to

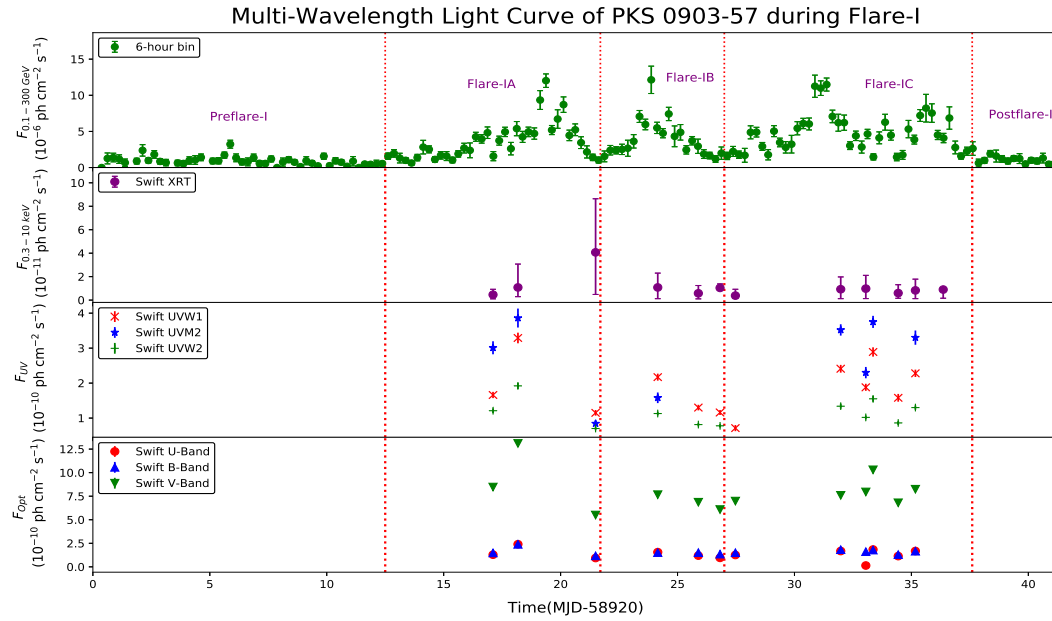


Figure 3.18. Multi-Wavelength light curve of PKS 0903-57 during Flare-I. Color codes are same as [Figure 3.17](#).

Flare-IB and the rest of the 6 observations correspond to Flare-IC.

As we mentioned earlier, the number of observations in X-ray to Optical wavebands is very low; hence it is not possible to do any detail analysis of light curve from X-ray to Optical waveband, only the γ -ray light curve has been modeled in detail.

3.7.2 Multi-Wavelength SED Modeling

We have modeled the multi-wavelength SEDs with a code ‘GAMERA’ [171]. It is publicly available on github [172]. The code solves time-dependent transport equation. It estimates the propagated electron spectrum $N(E,t)$ for an input injected electron spectrum and further it uses the propagated spectrum to calculate the Synchrotron and Inverse-Compton (IC) emissions. The transport equation used in GAMERA is defined as:

$$\frac{\partial N(E,t)}{\partial t} = Q(E,t) - \frac{\partial}{\partial E}(b(E,t)N(E,t)) - \frac{N(E,t)}{\tau_{\text{esc}}(E,t)} \quad (3.8)$$

where, $Q(E,t)$ is the input electron spectrum and $b(E,t)$ corresponds to the energy loss rate by Synchrotron and IC and can be defined as $(\frac{dE}{dt})$. In the last term $\tau_{\text{esc}}(E,t)$ denotes the escape time of electrons from the emission region.

Following Massaro *et al.* [173], a LP photon spectrum can be produced by the radiative losses of a LP electron spectrum. We have considered LP form of injection spectrum. The functional form of the electron spectrum is

$$Q(E) = L_0 \left(\frac{E}{E_0} \right)^{-(\alpha + \beta \log(\frac{E}{E_0}))} \quad (3.9)$$

where L_0 is the normalization constant and E_0 is the scaling factor. This code uses ‘Klein-Nishina’ cross-section to compute Inverse-Compton emission [174].

3.7.3 Physical Constraint for Multi-Wavelength SED Modeling

We have used Synchrotron and SSC (Synchrotron Self-Compton) emission to model the SEDs. The size of the emission region (R) can be constrained from the causality relation

$$R \leq \frac{ct_{\text{var}}\delta}{1+z} \quad (3.10)$$

where, t_{var} is the observed variability time, δ is the Doppler factor of the blob or emission region and z represents the redshift of the source. We could not find any estimate of Doppler factor (δ) for PKS 0903-57 from earlier studies. The values of Doppler factor for other flaring BL Lacs are found to be in the range of 20 to 40 in most cases. We have used the Doppler factor close to 20 for PKS 0903-57. For Doppler factor 21.5 & redshift 0.695, the variability time is 1.7 ± 0.9 hour and the size of the emission region has an upper limit of 2.3×10^{15} cm. Equation 3.10 gives only an approximate constraint on the size of the emission region, as there are several other factors that may affect this estimate [175].

3.7.4 Modeling the SEDs

Varying the fitting parameters in the code ‘GAMERA’ we have modeled multi-wavelength SEDs. In this case, we have considered constant escape of leptons from the emission region with escape time, $\tau_{\text{esc}} \sim R/c$, where R is the size of the emission region, used in the fitting and c is the speed of light in vacuum.

We have modeled multi-wavelength SEDs of the four phases: Flare-1B, Flare-1A, Flare-1B and Flare-1C, shown in Figure 3.19, Figure 3.20, Figure 3.21, & Figure 3.22 respectively. For all the phases mentioned above, we have plotted simultaneous data in different wavebands (Fermi-LAT γ -ray: circular magenta points; Swift XRT: green triangular points; Swift UV: cyan triangular points; Swift Optical: red-circular points; ATCA Radio: blue inverted-triangle); also we have shown the non-simultaneous data points in the grey square. We have modeled considering one zone emission region. During the modeling we have adjusted the values of different parameters e.g. minimum and maximum Lorentz factor of the injected electrons (γ_{min} & γ_{max}), magnetic field (B), size of the emission region (R), spectral index (α), curvature index (β), Doppler factor (δ). All the values of the fitted parameters for the various phases are given in Table 3.13.

The highest energy photons detected from Flare-1B, Flare-IB & Flare-IC have energy 5.56 GeV, 6.67 GeV & 29.33 GeV respectively. The three highest energy photons have energy 18.23 GeV, 37 GeV and 81 GeV in Flare-IA. The optical depth correction due to EBL (Extragalactic Background Light) at redshift 0.695 is negligible for tens of GeV energy [176] γ -rays; hence there is no significant attenuation in the SEDs. In Flare-IA (see [Figure 3.20](#)), the two highest energy data points show a rising trend in the SED; more observational data points are needed to confirm this trend in future. We have not fitted these two highest energy data points in our model.

We have also calculated the total jet power using the following equation:

$$P_{tot} = \pi R^2 \Gamma^2 c (U'_e + U'_B + U'_p) \quad (3.11)$$

where, P_{tot} is the total jet power; Γ is the bulk Lorentz-factor; U'_e , U'_B and U'_p are the energy density of the electrons (and positrons), magnetic field and cold protons respectively in the co-moving jet frame (prime denotes 'co-moving jet frame'; unprime denotes 'observer frame').

The power carried by the leptons is given by,

$$P_e = \frac{3\Gamma^2 c}{4R} \int_{E_{min}}^{E_{max}} EQ(E) dE \quad (3.12)$$

where, $Q(E)$ is the injected particle spectrum; integration limits are calculated by multiplying the maximum & minimum Lorentz factor with the rest-mass energy of electron.

The power due to magnetic field is calculated by,

$$P_B = R^2 \Gamma^2 c \frac{B^2}{8} \quad (3.13)$$

where, B is the magnetic field, used to model the SED.

The energy density in cold protons U'_p is calculated assuming the number ratio of electron-positron pair to proton is 10:1. We have maintained the charge neutrality condition in the jet. The jet power of protons is computed using the energy density of cold protons.

Subsequently, using [Equation 3.11](#), we have computed the total jet power of each flaring phases, tabulated in [Table 3.14](#). We have not found any paper where the mass or the Eddington luminosity of this source is mentioned. The values of jet power reported in [Table 3.14](#) are lower than the typical Eddington luminosities of BL Lacs like Mrk 501, Mrk 421 and AP Librae which are $(1.1-4.4) \times 10^{47}$ erg/s

[177], $(2.6-12.0) \times 10^{47}$ erg/s [178] and 3.75×10^{46} erg/s [179] respectively.

3.8 Summary and Discussion

PKS 0903-57 is a BL Lac type blazar, listed in Fermi's regularly monitored source-list and monitored continuously since August 2008. Last year i.e. in 2020, high flaring activity from this source has been detected in different telescopes in different wavebands. Such activity was also reported before e.g. in 2015 and 2018; 7-day binned γ -ray light curve (Figure 3.1) over the 12 years does not show any significant activity around 2015. Some flaring states are observed in the γ -ray light curve in 2018 and 2020. We continued our analysis focusing on these activity periods. In Figure 3.1, we have shown 7-day binned γ -ray light curve over 12 years. From Figure 3.1, we have denoted two major flaring activities, denoted as Flare-1 & Flare-2. Further shorter time binning (1-day, 12-hour, 6-hour, 3-hour) reveals sub-structures of these flares. Flare-1 has only one sub-structure whereas Flare-2 has two sub-structures i.e. Flare-I & Flare-II. In shorter time binned γ -ray light curve, we have detected different phases (preflare, flare, postflare) of each sub-structure; even several distinctive peaks of each flare region have been detected. Flare-1 has two phases: Flare-1A & Flare-1B (Figure 3.4). Flare-1A has two peaks: P_1 & P_2 (Figure 3.5) and Flare-1B has only one peak: P_1 (Figure 3.6). The γ -ray SEDs of Flare-1 have been fitted with PL, LP, BPL and PLEC to check which spectral model gives the best fit to the spectral data (Figure 3.14). A similar procedure has been followed for the following flares i.e. on Flare-I & Flare-II. In most cases, it has been found that the γ -ray SEDs of the phases can be well described by the LP model. All the calculations done here is based on 3-hour binned γ -ray light curve. We have calculated the shortest variability time in γ -ray, which is found to be 1.7 ± 0.9 hour. We have also studied the rising time (T_r) and decay time (T_d) of the flaring phases with Equation 3.2, to check whether they follow any trend or not. The rising time and decay time have been calculated for each peak, mentioned in Table 3.3 to Table 3.8. The rising and decay timescale found in our study is the order of hour scale. For comparative study, we have considered a quantity η [166].

$$\eta = \frac{T_d - T_r}{T_d + T_r} \quad (3.14)$$

where, $-1 < \eta < 1$. Depending on the value of the η , there are three scenarios:

- If the rising and decay timescale are nearly equal i.e. $T_r \sim T_d$, symmetric temporal evolution. This can be seen in symmetric flares for which $-0.3 <$

Table 3.13: Results of multi-wavelength SED modeling shown in the [Figure 3.19](#) to [Figure 3.22](#)

Parameters	Symbol	values	Time duration
Flare-1B			
Spectral index of injected electron spectrum (LP)	α	2.1	
Curvature index of injected electron spectrum	β	0.09	
Magnetic field in emission region	B	0.25 G	
Size of the emission region	R	6.6×10^{16} cm	4.4 days
Doppler factor of emission region	δ	21.5	
Min. value of Lorentz factor of injected electrons	γ_{min}	1.5×10^2	
Max. value of Lorentz factor of injected electrons	γ_{max}	3.0×10^4	
Flare-IA			
Spectral index of injected electron spectrum (LP)	α	1.7	
Curvature index of injected electron spectrum	β	0.20	
Magnetic field in emission region	B	0.25 G	
Size of the emission region	R	5.9×10^{16} cm	9.2 Days
Doppler factor of emission region	δ	21.5	
Min. value of Lorentz factor of injected electrons	γ_{min}	2.4×10^2	
Max. value of Lorentz factor of injected electrons	γ_{max}	4.5×10^4	
Flare-IB			
Spectral index of injected electron spectrum (LP)	α	1.7	
Curvature index of injected electron spectrum	β	0.20	
Magnetic field in emission region	B	0.25 G	
Size of the emission region	R	3.0×10^{16} cm	5.3 Days
Doppler factor of emission region	δ	21.5	
Min. value of Lorentz factor of injected electrons	γ_{min}	3.4×10^2	
Max. value of Lorentz factor of injected electrons	γ_{max}	3.9×10^4	
Flare-IC			
Spectral index of injected electron spectrum (LP)	α	1.7	
Curvature index of injected electron spectrum	β	0.17	
Magnetic field in emission region	B	0.19 G	
Size of the emission region	R	8.0×10^{16} cm	10.6 Days
Doppler factor of emission region	δ	21.5	
Min. value of Lorentz factor of injected electrons	γ_{min}	2.0×10^2	
Max. value of Lorentz factor of injected electrons	γ_{max}	5.5×10^4	

Table 3.14: Table for total jet power for each flaring event

Activity	Total Jet Power (erg/s)
Flare-1B	1.3×10^{46}
Flare-IA	2.3×10^{46}
Flare-IB	3.0×10^{46}
Flare-IC	1.2×10^{46}

$\eta < 0.3$.

- If rising timescale is greater than the decay timescale i.e. $T_r > T_d$, when $\eta < 0.3$; then injection rate of the electrons is slower than the cooling rate of the electrons into the emission region.
- If the decay timescale is greater than the rising timescale i.e. $T_d > T_r$, when $\eta > 0.3$. This means the electrons take longer time to cool down into the emission region.

From our analysis, we found that out of total 15 peaks; 6 peaks have $T_d > T_r$, 4 peaks have $T_d < T_r$ and 5 peaks have $T_d \sim T_r$. It is clear that there is no particular pattern in rising and decay timescale for this source. A flaring part is denoted as a 'peak' only when the light curve covered a sufficient number of points; if there are very few points, e.g. 2 or 3, we have not considered them as a 'peak'.

Simultaneous multi-wavelength data are available only for four phases: Flare-1B, Flare-IA, Flare-IB & Flare-IC in Swift XRT, Swift UVOT and ATCA; though the data in UVOT and Radio are very less. We have modeled these four phases with a time-dependent code 'GAMERA'. 'GAMERA' solves the transport equation for electrons; it also considers the energy loss by Synchrotron and Synchrotron Self Compton (SSC) process and escapes from the emission region. We have considered a constant escape from the emission region where the escape timescale is $R/c \sim 10^6$ s. We have modeled with 'single-zone' model. The details of the parameters have been mentioned in [Table 3.13](#). We have divided the total flaring duration into four equal time intervals for each of the four phases and we can see the distinct SEDs corresponding to each time interval. The total time duration of Flare-1B, Flare-IA, Flare-IB and Flare-IC are 4.4 days, 9.2 days, 5.3 days and 10.6 days respectively.

To fit the γ -ray light curve, we have used [Equation 3.2](#); the 'Blazar community' uses this function to model the peaks in γ -ray light curve. The first part of the above-mentioned equation is used to fit the rising part, which gives the rising time. We can estimate the decay timescale by fitting the decaying part of a flare with the second part of the equation. If a flare contains more than one peak, in that case, we have considered a sum of the exponents of the rising & decay time to fit all the detected peaks in that phase. In this case, peak flux (F_0) and peak time (t_0) will be different for different peaks, which is already known from observation. There are several reasons for which the fit may not be good e.g. low TS, fewer data points and large error bars on the data points. In case of rapid flux change, it is difficult to fit all the peaks (even the small peaks) which could be a possible reason behind the poor fitting.

The time binning of the γ -ray light curve has not been chosen arbitrarily. It is done based on the quality of the data i.e. TS value of each data point. For a very bright γ -ray source and very high flux, the data may be of very good quality and we can bin the light curve upto minute timescale [180]. In our analysis, we have scanned the 3-hour binned γ -ray light curve for which $TS \geq 25$, i.e. the data points have 5σ significance. The γ -ray flux error increases as the bin size decreases (if we compare 3-hour & 6-hour time binning, we can easily notice this). Moreover, shorter time binning than 3-hour would be difficult for our analysis. Also, to define a ‘peak’, a fitting curve must cover a sufficient number of points, which is possible if we choose 3-hour time bin instead of 6-hour time bin. The optical depth correction due to EBL is not important in our case as the energy of the observed highest energy photons is only a few GeV.

3.9 Conclusion

We have analyzed 12 years (From 4th August 2008 to 6th Jan 2021) γ -ray light curve of PKS 0903-57, from which we have detected two flaring activities in 2018 & 2020. The γ -ray flux was the highest in 2020. We have identified two flares: Flare 1 and Flare 2. Flare-1 has one sub-structure, which has two phases: Flare-1A & Flare-1B. Flare 2 has two sub-structures: Flare I and Flare II, which have several phases. Flare-I has five phases: Preflare-I, Flare-IA, Flare-IB, Flare-IC & Postflare-I. Flare-II has three phases: Preflare-II, Flare-II & Postflare-II. We have fitted Flare-1A, Flare-1B, Flare-IA, Flare-IB, Flare-IC & Flare-II with [Equation 3.2](#) and calculated the rising and decay time of the peaks of the flaring phases. We have computed the γ -ray variability time of this source, which is found to be 1.7 ± 0.9 hour. The different phases of the γ -ray SEDs have been fitted with PL, LP, BPL & PLEC to find the best-fitted spectral model. Flare-1B, Flare-IA, Flare-IB & Flare-IC have simultaneous multi-wavelength data, and for these phases LP is found to be the best-fitted model. The multi-wavelength SEDs of these four phases have been modeled with a time-dependent code, ‘GAMERA’. Due to insufficient multi-wavelength data, further multi-wavelength analysis is not possible for this source. We have assumed the emissions are happening from a single-zone. The total jet power required during the flaring phases is estimated to be a few times 10^{46} erg/sec.

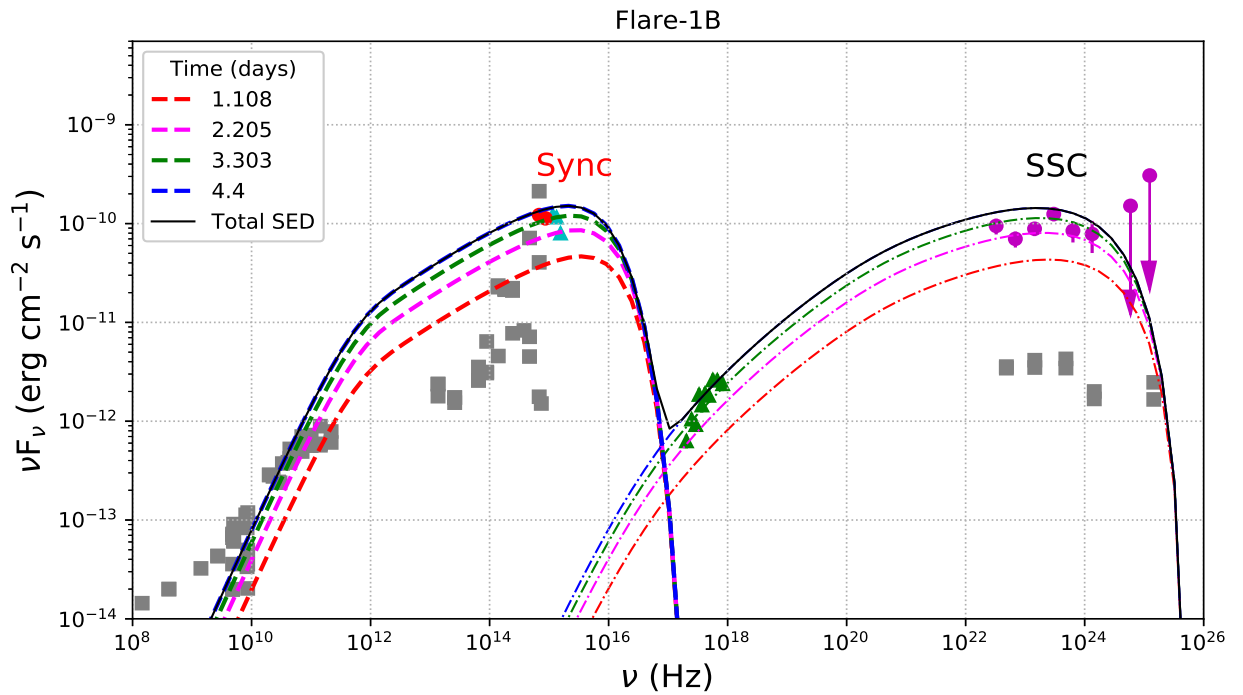


Figure 3.19. Multi-Wavelength SED of Flare-1B. Following are the color codes: ‘Grey Square’= Archival data points/ Non-simultaneous data points; ‘Red Solid Circle’= Optical (Swift); ‘Cyan Triangle’= Ultra-Violet (Swift); ‘Green Triangle’= X-ray (Swift); ‘Magenta Solid Circle’= γ -Ray (Fermi-LAT).

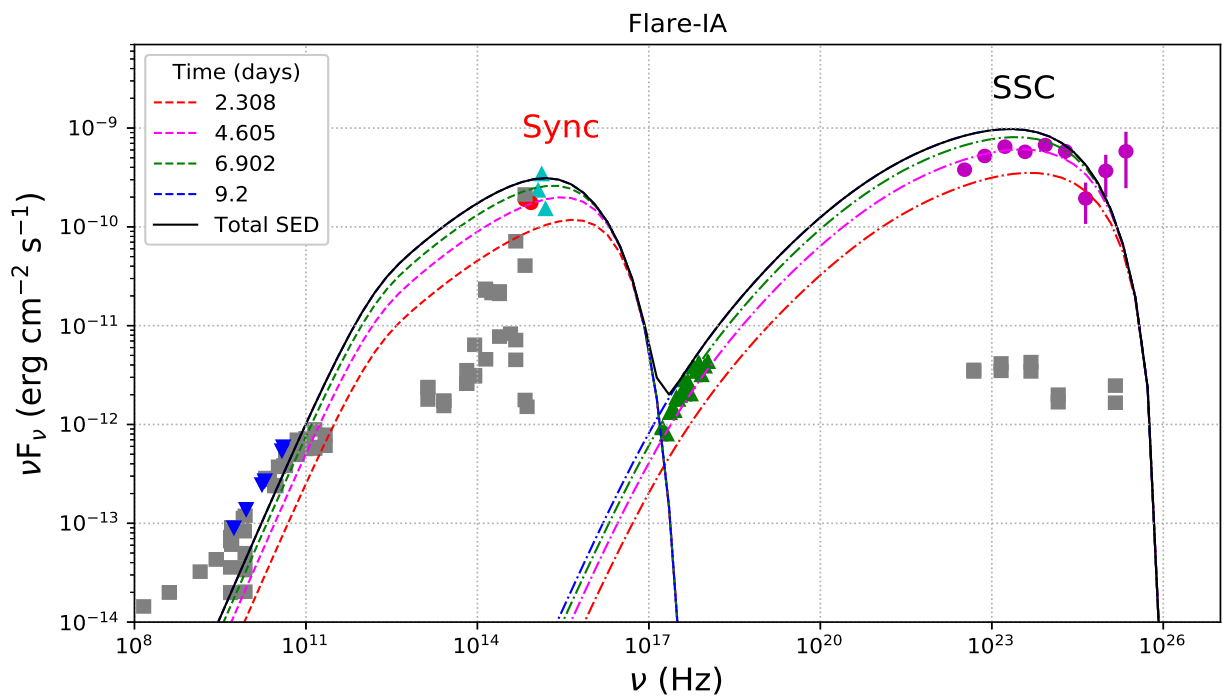


Figure 3.20. Multi-Wavelength SED of Flare-1A. The color codes are similar to [Figure 3.19](#), radio data points denoted by ‘Blue inverted-Triangle’ (ATCA).

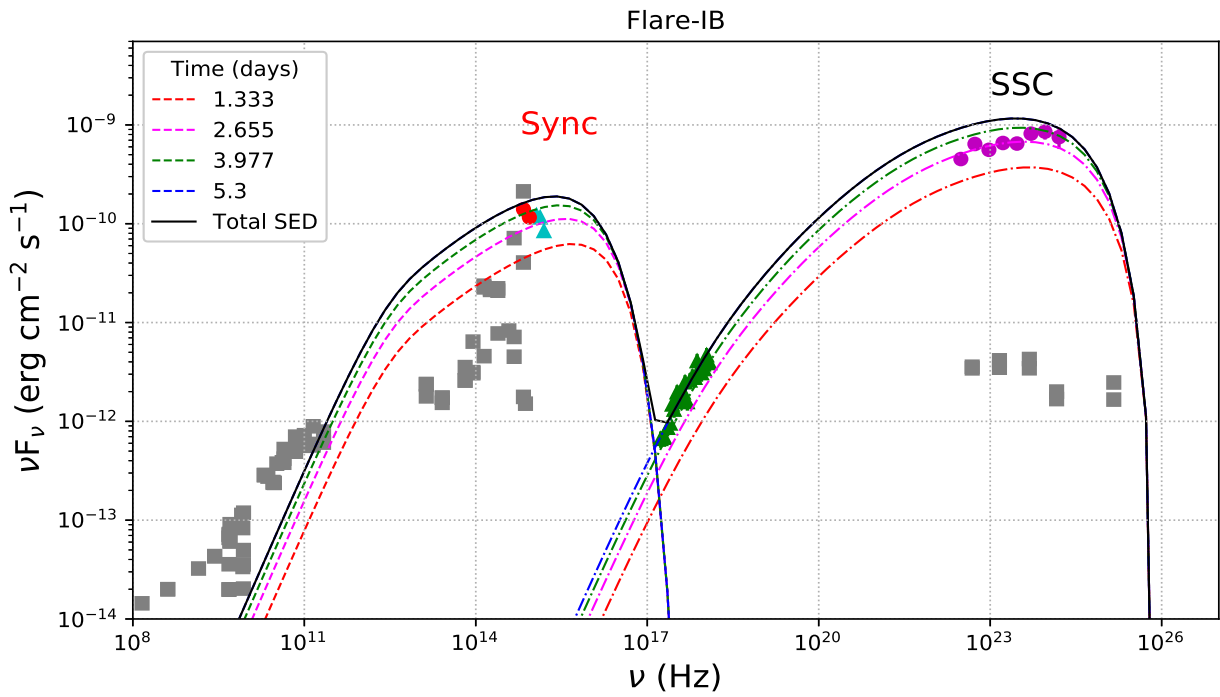


Figure 3.21. Multi-Wavelength SED of Flare-IB. The color codes are same as Figure 3.19.

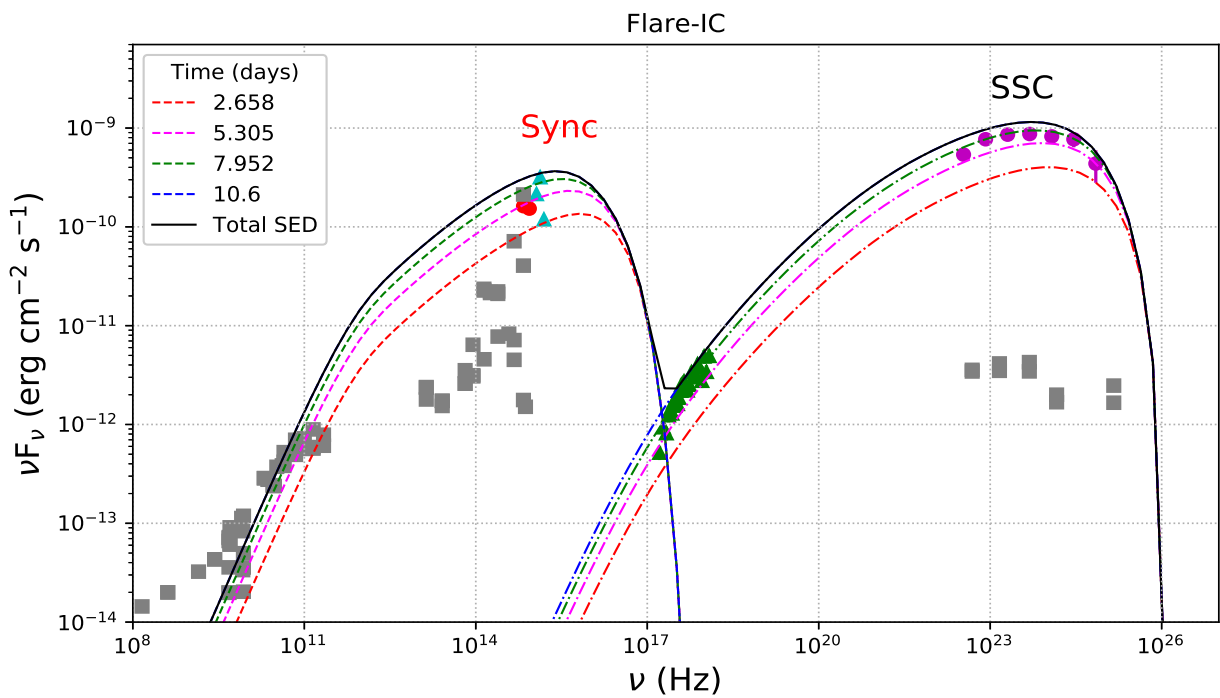


Figure 3.22. Multi-Wavelength SED of Flare-IC. The color codes are same as Figure 3.19.

Exploring the Emission Mechanisms of Mrk 180 with long term X-ray and γ -ray data

4.1 Introduction

The central emission core of active galaxies is powered by accretion onto a supermassive black hole (SMBH). This leads to the formation of a collimated jet of outflow, along the angular momentum direction, that outshines the entire galaxy [1]. Active Galactic Nuclei (AGNs) are one of the most prominent sources of high energy γ -rays. The jet transports energy and momentum over large distances. In the case of blazars, the jet points along the observer's line of sight and provides a unique testbed to study the acceleration of cosmic rays [see 5, for a review].

The broadband SED of a blazar covers the entire electromagnetic spectrum, ranging from radio to very high-energy (VHE, $E \gtrsim 30$ GeV) γ -rays. It exhibits two peak emission frequencies. The low-energy peak occurs between radio to soft X-ray energies and can be attributed to synchrotron radiation of relativistic electron and positron population. The high-energy peak between X-ray to VHE γ -ray energies can arise from various processes. The most prevalent explanation is the inverse-Compton scattering of synchrotron photons (synchrotron self-Compton, SSC) or external photons (EC) originating from the broad-line region (BLR), dusty torus (DT), or the accretion disk (AD). In addition, the VHE γ -rays can also come from photohadronic ($p\gamma$) or hadronuclear (pp) interactions of accelerated cosmic rays with the ambient radiation or matter in the emission region of the jet or proton synchrotron radiation [4–6].

Mrk 180 was discovered by Swiss-origin astronomer Fritz Zwicky and later identified as a BL Lac object in 1976 by spectral analysis. It is a high-synchrotron peaked BL Lac (HBL) object embedded at the center of an elliptical galaxy [181], located at redshift, $z=0.0458$ [182] with R.A.= 174.11008 deg, Decl.= 70.1575 deg. This source was detected for the first time in X-rays by HEAO-1 [183], since then it has been monitored by several telescopes e.g. Fermi-LAT, Swift, Major Atmospheric Gamma Imaging Cherenkov Telescope (MAGIC), XMM-Newton, Monitoring of jets in Active Galactic Nuclei with VLBA Experiments (MOJAVE), KVA, ASM. In March 2006, VHE γ -ray emission was detected for the first time [184] from this source, triggered by an optical burst. Rügamer *et al.* [185, 186] did

multi-wavelength study on this source. Mrk 180 was also monitored for a long period (2002- 2012) in the optical waveband and its light curve was analyzed by Nilsson *et al.* [187].

The Telescope Array experiment, located in Utah, United States, is a state-of-the-art detector observing ultra-high-energy cosmic rays (UHECRs; $E \gtrsim 10^{17}$ eV) in the northern hemisphere. Based on an intermediate-scale anisotropy search using 5 years of data, the TA collaboration earlier reported a cluster of events at RA=146°.7 and Dec=43°.2, found by oversampling in 20° radius circles [188]. 72 UHECR events were detected in this direction at $E > 57$ EeV, where TA has 100% detection efficiency. The hotspot had a Li-Ma significance of 5.1σ . He *et al.* [7] identified Mrk 180 as a possible source of UHECRs in the context of explaining the origin of the TA hotspot [188–190]. Motivated by the earlier studies, we carry out a comprehensive study of Mrk 180 to ascertain the underlying mechanism of high-energy γ -ray emission and whether it can be the source of UHECRs beyond 57 EeV contributing to the TA hotspot.

We have analyzed the Fermi-LAT data collected over a period of 12.8 years, the Swift XRT and UVOT data, and in addition to these the XMM-Newton X-ray data to construct the broadband SED of this source. We have discussed the data analysis method in section 4.2. We have also searched for fluctuations in the γ -ray flux in the Fermi-LAT light curve, as discussed in section 4.3. Subsequently, we build the long-term multi-wavelength SED. We discuss the theoretical framework for SED modeling in section 4.4. We present our results in section 4.5 and discuss them in section 4.6. Finally, we draw our conclusions in section 4.7.

4.2 Data Analysis

4.2.1 Fermi-LAT Data Analysis

The Pass 8 Fermi-LAT γ -ray data of Mrk 180 was extracted from Fermi Science Support Center (FSSC) data server [156] for a period of more than 12.8 years (August 2008 to May 2021). We have used Fermipy v1.0.1 [191], an open-source python package to analyze Fermi-LAT γ -ray data. Moreover, we have used Fermi-LAT Fourth Source Catalog Data Release 2 (4FGL-DR2; gll_psc_v27.fits) [192]. We have modeled the Galactic diffuse emission by the latest model template (gll_iem_v07; [193]) and for the extra-galactic isotropic diffuse emission model, we have considered iso_P8R3_SOURCE_V2_v1.txt. We followed Fermipy’s documentation for further analysis [194] and extracted the light curve and SED of Mrk 180.

For analyzing the data, two files are required first one is a configuration file (.yaml file) and another one is a analysis script (.py file). In the configuration file, we provided the following details: event type, event class, ROI size, minimum &

maximum energy, maximum zenith-angle cut selection, target source name, IRF file name etc.

Same as before (subsection 3.2.1), we have chosen `evclass=128` and `evtype=3`. We extracted the Fermi-LAT γ -Ray data from FSSC data server considering a search radius of 30° around the source Mrk 180. During the data preparation, we selected a ROI of 10° , and the maximum zenith angle of 90° was chosen to avoid earth limb contamination in our analysis. We restricted our analysis to an energy range of 100 MeV to 500 GeV. All these information were provided in the configuration file (.yaml file).

Thereafter we prepared the analysis script using ‘GTAnalysis’. ‘GTAnalysis’ serves as a wrapper over the pyLikelihood classes and perform all the event selection, data binning, exposure map creation, like mentioned previously (subsection 3.2.1). Following rest of the analysis procedure, we have obtained the γ -ray light curve shown in Figure 4.1 and the SED, which is used to construct the multi-wavelength SEDs shown in Figure 4.2, Figure 4.4, and Figure 4.5.

4.2.2 SWIFT XRT and UVOT Data Analysis

We collected all the XRT and UVOT data over the period August 2008 to May 2021, available for Mrk 180. We have analyzed 44 observations. The standard data reduction procedure [121] has been followed to extract the source and background region.

In Swift-XRT data, we have used clean event files corresponding to Photon-Count mode (PC mode), which we have obtained using a task ‘xrtpipeline’ version 0.13.5. The calibration file (CALDB), version 20190910, and other standard screening criteria have been applied to the cleaned data. A radius of interest of 20-30 pixels has been considered to mark the source region, the radius of the background region is also the same, but it is far away from the source region. With the help of ‘xselect’ tool, we have selected the source region and background region and saved the spectrum files of the corresponding regions. Then ‘xrtmkarf’ and ‘grppha’ tools have been used to generate ancillary response files (arfs) and group the spectrum files with the corresponding response matrix file (rmf); thereafter ‘addspec’ and ‘mathpha’ have been used. Thus we have obtained the spectrum. Thereafter, the spectrum has been modeled with xspec [162] (Version 12.11.0) tools. We have included the absorption by neutral hydrogen having column density, $N_{\text{H}} = 1.37 \times 10^{20} \text{ cm}^{-2}$ [163, 195]. The final X-ray SED obtained in this way has been shown in Figure 4.2, Figure 4.4, and Figure 4.5.

Mrk 180 was also monitored by Swift UVOT in all six filters: U(3465 Å), V (5468 Å), B (4392 Å), UVW1 (2600 Å), UVM2 (2246 Å) and UVW2 (1928 Å). The source region has been extracted from a region of 5" around the source, keeping the

source at the center of the circle. The background region has been taken ~ 3 times larger than the source region and it is far away from the source region. Using ‘uvotsource’ tool, we have extracted the source magnitude. This magnitude does not include the galactic absorption, so it has been corrected. A python module ‘extinction’ [129] has been used to get the extinction values corresponding to all the Swift-UVOT filters. We have considered Fitzpatrick [164] dust extinction function for $R_V=3.1$, where R_V is a dimensionless quantity, which is the slope of the extinction curve. For diffused interstellar medium (ISM) the mean value of R_V is 3.1 [196–198]. Following are the values of the extinction coefficients of different Swift-UVOT wavebands which we have used in this work; U: 0.05584, V: 0.03460, B: 0.04603, UVW1: 0.07462, UVM2: 0.10383, UVW2: 0.09176.

4.2.3 XMM-Newton X-ray Data Analysis

From the data archive of XMM-Newton [199], we found two observations for Mrk 180: 0094170101 and 0094170301 of 20 ks and 8 ks respectively. We have followed standard data reduction procedure [137] to extract the SED. We have extracted SED points from MOS1 and MOS2; combined them and finally, we got SED points from MOS. Also, we extracted SED points from pn detector. Thereafter, we used xspec [162] (Version 12.11.0) to model these spectra. Other than X-ray data, we have also analyzed OM image mode data. Following the same data reduction procedure, we prepared the data; then we used ‘omichain’ for further analysis. We followed omichain [200] instruction for the last step. By the ‘om2pha’ [201] command, we extracted the spectrum file to analyze in xspec. For this step, the required OM response files have been copied from OMResponseFile [202]. The first observation 0094170101, contains single data corresponding to the u-band, which is insufficient for further analysis whereas, the second observation 0094170301 does not contain any image file for further study. So, our multi-wavelength data does not contain any XMM-Newton OM data.

4.2.4 MOJAVE Data

We have collected MOJAVE data for Mrk 180 from the MOJAVE/2cm Survey Data Archive [203]. There are seven observations in the archive. We have used those data to construct the multi-wavelength SED.

4.2.5 MAGIC Data

VHE γ -rays from Mrk 180 were detected during an optical outburst in 2006 [204]. We have used that data from MAGICDataCentre [205] for our study.

4.2.6 Archival Data

We have collected the archival data from SSDC SED builder [206] and shown it with grey squares in the multi-wavelength SED (Figure 4.2, Figure 4.4, and Figure 4.5).

4.3 Fermi-LAT gamma-Ray Light curve Analysis

We analyzed 12.8 years (MJD 54682.65-59355.67) of Fermi-LAT γ -ray data. Figure 4.1 is the 30-day binned Fermi-LAT γ -ray light curve. We have used the Bayesian Block method [165] to detect any fluctuations. We have not found any significant variation in the γ -ray flux. Though there are a few data points with high γ -ray flux, those points have large error bars, so further analysis with a smaller bin size is not feasible in this case. We proceed to build up the SED with the long-term data, as this source does not have any obvious temporal features.

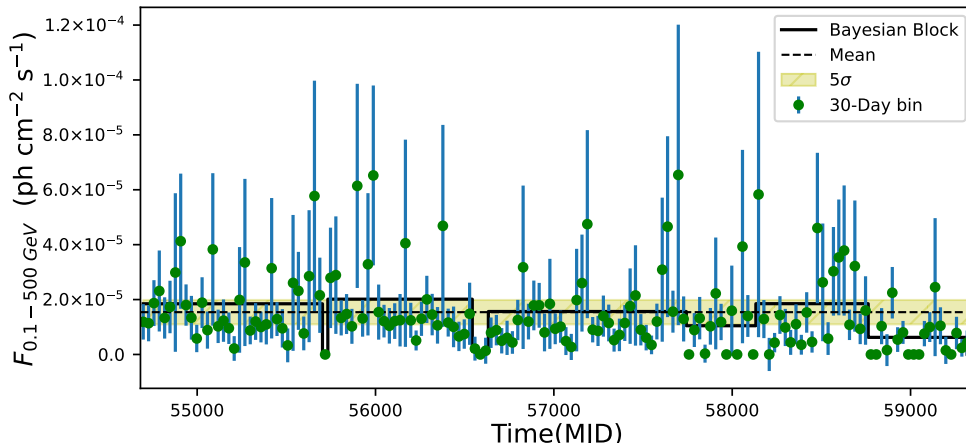


Figure 4.1. Application of Bayesian Block Method on Fermi-LAT γ -Ray Data of Mrk 180 (MJD 54682.65- 59355.67)

4.4 Multi-Wavelength SED Modeling

Fermi-LAT γ -ray, Swift X-ray, ultraviolet & optical data and XMM-Newton X-ray data have been analyzed and archival data from MOJAVE, MAGIC and SSDC have been compiled to plot the SED covering radio to VHE γ -ray frequencies. As discussed previously, Figure 4.2, Figure 4.4 and Figure 4.5 shows the double hump structure of the blazar SEDs. We have modeled the SED using pure leptonic and lepto-hadronic scenarios. For the latter, we consider the the line of sight component of the electromagnetic cascade, initiated by UHECR interactions [207, 208], and also pp interaction as the origin of VHE γ -rays. An external radiation field is required to produce a significant flux of secondary γ -rays in $p\gamma$ interactions, hence we do not include this scenario in this work. In the following subsections,

we discuss about the models used in this work to explain the multi-wavelength SED of Mrk 180.

4.4.1 Leptonic Modeling

We have considered a spherical emission region of radius R within the jet, moving with a Doppler factor δ_D , where relativistic electrons and positrons, accelerated in the jet lose energy through synchrotron radiation in a steady and uniform magnetic field B , and also by SSC emission. From the maximum likelihood analysis of Fermi-LAT data, a log-parabola injection was found to best fit the data. Massaro *et al.* [209] showed that a log-parabolic photon spectrum can be produced from the radiative loss of a log-parabolic electron spectrum. So, we have used the log-parabolic spectrum of the injected electrons in the blob to explain the multi-wavelength SED of Mrk 180, given by the following expression,

$$Q(E) = L_0(E/E_0)^{-(\alpha+\beta \log_{10}(E/E_0))} \quad (4.1)$$

where $Q(E)$ is the log-parabolic distribution, L_0 is the normalization constant, E_0 is the scaling factor or pivot energy which is set to 97 MeV in our modeling and kept fixed, α is the spectral index and β is the curvature index.

We have used the open-source code GAMERA [172] [171] to model the multi-wavelength leptonic emission. It solves the time-dependent transport equation and propagates the particle spectrum $N(E, t)$ for an injected spectrum $Q(E)$ to calculate the synchrotron and SSC emissions including the Klein-Nishina effect. GAMERA solves the following transport equation,

$$\frac{\partial N(E, t)}{\partial t} = Q(E) - \frac{\partial}{\partial E}(b(E, t)N(E, t)) - \frac{N(E, t)}{\tau_{\text{esc}}} \quad (4.2)$$

where, $Q(E)$ is the input particle spectrum, $b(E, t)$ corresponds to the energy loss rate by synchrotron and SSC emission. The term $\tau_{\text{esc}}(E, t)$ denotes the escape time of particles from the emission region. We consider a constant escape of the electrons from the emission region over the dynamical timescale, $\tau_{\text{esc}} \sim R/c$, where c is the speed of light. We find that the time-evolved electron spectrum reaches the steady state after nearly 100 days, and this spectrum has been used in this work.

4.4.2 UHECR interactions

We have assumed a power-law injection of the protons into the interstellar medium (ISM) of the following form

$$N_p(E_p) = \frac{dN}{dE_p} = A_p E_p^{-\alpha_p} \quad (4.3)$$

where A_p is the normalization constant of the injected proton spectrum, α_p is the spectral index, which is the same for electrons and protons as they are accelerated in the same region. We have taken the minimum energy of protons $E_{p,\min} = 0.1$ EeV, and the maximum energy of protons $E_{p,\max} = 100$ EeV.

The ultra-high energy protons escape from the emission region and propagate through the extra-galactic medium interacting with CMB and EBL photons. In this process, electrons, positrons, γ -rays, and neutrinos are produced through Δ -resonance and Bethe-Heitler pair production. Protons interact with the CMB and EBL photons in the following way,

$$p + \gamma_{bg} = p + e^+ + e^- \quad (4.4)$$

$$p + \gamma_{bg} \rightarrow \Delta^+ \rightarrow \begin{cases} n + \pi^+ \\ p + \pi^0 \end{cases} \quad (4.5)$$

The neutral pions decay to gamma photons ($\pi^0 \rightarrow \gamma\gamma$) and the charged pions decay to neutrino ($\pi^+ \rightarrow \mu^+ + \nu_\mu \rightarrow e^+ + \nu_e + \bar{\nu}_\mu + \nu_\mu$). The resulting cosmogenic neutrinos propagate undeflected by magnetic fields and unattenuated by interaction with other particles.

The secondary e^\pm , γ -rays initiate electromagnetic (EM) cascade by undergoing pair production, inverse-Compton upscattering of the background photons, and synchrotron radiation in the extragalactic magnetic field (EGMF). The resulting spectrum extends down to GeV energies and depends more on the propagation distance and background photon model than the injection parameters. We use the semi-analytical EBL model given in Gilmore *et al.* [210] for the propagation of UHECR and the attenuation of secondary EM particles, and also the primary γ -rays coming from leptonic emission inside the source. UHECRs also interact with the universal radio background [211] which is important at energies higher than the Greisen-Zatsepin-Kuzmin (GZK) cutoff energy for Δ -resonance with the CMB photons. The EGMF causes a spreading of the UHECR beam and also the EM particles. We consider the contribution from the line of sight resolved component of the cascade spectrum to the observed SED (cf. [section 4.5](#)).

We have used the publicly available simulation framework, CRPROPA 3 [212–214] to propagate UHECR protons from their source to the observer. The secondary EM particles are propagated in the CRProPa simulation chain, using a value of EM thinning $\eta = 0.6$.

4.4.3 pp interactions

An alternative scenario is when the relativistic protons have much lower energy than UHECRs and they interact with the cold protons within the emission region as they are trapped in the magnetic field of the emission region. The proton-proton interactions result in the production of neutral and charged pions. These pions decay into secondary particles e.g. electrons/ positrons, neutrinos and γ -rays. The proton-proton interaction channels can be shown in the following manner:

$$p + p \rightarrow \begin{cases} \pi^0 \rightarrow \gamma + \gamma \\ \pi^+ \rightarrow \nu_\mu + \mu^+ \rightarrow \nu_\mu + e^+ + \nu_e + \bar{\nu}_\mu \\ \pi^- \rightarrow \bar{\nu}_\mu + \mu^- \rightarrow \bar{\nu}_\mu + e^- + \bar{\nu}_e + \nu_\mu \end{cases} \quad (4.6)$$

We have considered a power-law proton injection spectrum within the emission region, with a spectral index α_p and minimum $E_{p,\min}$ and maximum energy $E_{p,\max}$. We have used the publicly available code GAMERA [172] [171] for the time-independent pp modeling. It uses the formalism given in Kafexhiu *et al.* [215]. There are four hadronic interaction models that are included in this code, and for our work, we have used the one given by PYTHIA 8.18 [216].

We have balanced the total charge in the emission region to determine the total number of protons. The γ -ray spectrum produced in pp interactions has been corrected for internal absorption by the lower energy photons inside the blob, and also for absorption by the EBL.

4.4.4 Jet Power

We have calculated the kinematic jet power using the following equation

$$P_{\text{tot}}^k = P_e + P_B + P_p = \pi R^2 \Gamma^2 c (u'_e + u'_p + u'_B) \quad (4.7)$$

where P_{tot}^k is the kinematic jet power, Γ is the bulk Lorentz factor; u'_e , u'_p and u'_B are the energy densities of the relativistic electrons (and positrons) and protons and magnetic field respectively in the comoving jet frame [217, 218]. The primed and unprimed notations denote quantities in the comoving jet frame and the AGN frame, respectively. We have maintained the charge neutrality condition in the jet. If we add the jet power of cold protons the luminosity budget in proton-proton

interaction model exceeds the Eddington luminosity as discussed in Banik and Bhadra [217], Banik *et al.* [218]. A sub-Eddington jet power in proton-proton interaction model is possible in the scenario discussed in a recent paper Xue *et al.* [219] after including the jet power in cold protons. However, we compare only the kinematic jet power to the Eddington luminosity as it has been done in earlier papers.

Here, we have considered, the bulk Lorentz factor (Γ) and Doppler factor (δ_D) are equal. We have presented the jet powers of individual components and the total kinematic jet power in Table 4.1.

The mass of the black hole of Mrk 180 as reported in earlier papers has been used to calculate the Eddington luminosity. According to Treves *et al.* [220], the value of $\log_{10}(M_{\text{BH}}/M_{\odot})$ is 8.59 and according to Falomo *et al.* [221], the value of $\log_{10}(M_{\text{BH}}/M_{\odot})$ is 8.70; where M_{BH} is the mass of the black hole and M_{\odot} is the solar mass. Using these values, we have calculated the Eddington luminosity (L_{Edd}) of Mrk 180, which are 5.06×10^{46} erg/s and 6.51×10^{46} erg/s respectively. The total kinematic jet powers obtained in our models are less than the Eddington luminosity of Mrk 180.

4.5 Results

Mrk 180/ Mkn 180/ TeV J1136+701 or 4FGL J1136.4+7009 is an HBL type blazar at a redshift of 0.045. This source is monitored by several telescopes viz. Fermi-LAT, Swift, XMM-Newton, MOJAVE, MAGIC, KVA, ASM, RATAN-600, Metsähovi, Effelsberg, IRAM throughout the year, and it was closely monitored during the high state in optical waveband in 2006.

12.8 years (MJD 54682.65- 59335.67) of Fermi-LAT γ -ray data of Mrk 180 has been analyzed in this work. Besides Fermi-LAT γ -ray data, we also collected data in other wavebands e.g. Swift, XMM-Newton, MOJAVE, and MAGIC. Figure 4.1 is the long-term Fermi-LAT γ -ray light curve in 30-day binning. As can be seen from section 4.3, this long-term light curve does not show any significant flaring throughout this time, also the error bars of the high-energy γ -ray data points are large, hence a more detailed analysis of the light curve cannot give us any useful information. To know about the physical processes which can explain the observed spectrum, we studied the long-term SED of Mrk 180; where we have used multi-wavelength data from different telescopes. The multi-wavelength SED shows the double hump structure, which has been modeled with GAMERA [172]; considering a simple one-zone spherical emission region within the jet. In Figure 4.2, Figure 4.4 and Figure 4.5, we have shown the multi-wavelength SEDs fitted with different models, e.g. pure leptonic, lepto-hadronic. Also, we

have shown the residual (Data-Model/error) plot corresponding to the fit to each model in [Figure 4.2](#), [Figure 4.4](#) and [Figure 4.5](#).

First, we consider a pure leptonic model ([Figure 4.2](#)), where the first hump is produced due to the synchrotron radiation of the relativistic electrons, and the second hump is produced due to the up-scattering of the synchrotron photons by the relativistic electrons. As discussed in [subsection 4.4.1](#), we consider a spherical emission region or blob of radius R within the blazar jet. Leptons are injected within the blob following an injection spectrum ([Equation 4.1](#)). The best-fitted parameter values corresponding to this modeling, e.g. spectral index (α), curvature index (β) are listed in the first column of [Table 4.1](#). We have mentioned the jet power of different components, e.g. relativistic leptons (P_e), magnetic field (P_B), and relativistic protons (P_p) in [Table 4.1](#), also the total kinematic jet power (P_{tot}^k) which is the sum of the jet power of all the components of a model.

The pure leptonic model is found to be insufficient to explain the multi-wavelength SED, as the highest energy γ -ray data point cannot be fitted with this model. Moreover, the slope of the observed X-ray spectrum does not match the slope of the synchrotron spectrum obtained in our model. To improve the fit to the multi-wavelength SED, particularly at the VHE γ -ray regime, we check the fit with lepto-hadronic models. As discussed earlier, we have considered two kinds of hadronic processes, viz., the UHECR interaction with the background photons and the pp interaction within the blob.

In the case of UHECRs (for simplicity we consider only protons), the escape of protons from the blazar jet can dominate over the energy loss inside the blazar jet. We consider a power-law injection of protons into the interstellar medium (ISM) following [Equation 4.3](#). We have considered proton injection into ISM between $E_{p,\text{min}} = 0.1$ EeV and $E_{p,\text{max}} = 100$ EeV. The injection spectral index $\alpha_p = 2.2$ is the same as for leptons. In the UHECR interaction model, we consider the three-dimensional propagation of UHECRs to calculate the fraction of them that survives within 0.1° degrees of initial emission direction and denote it by ξ_B . Protons are propagated from the source at a comoving distance ~ 200 Mpc and collected over a spherical region of radius 1 Mpc. We consider a random turbulent EGMF given by a Kolmogorov power spectrum and an RMS field strength of $B_{\text{rms}} \approx 10^{-5}$ nG and a coherence length of 0.5 Mpc using wave modes between 80 kpc and 2.25 Mpc. The distribution of survival fraction with deflection angle is shown in [Figure 4.3](#). We multiply the flux of cosmogenic γ -ray spectrum by ξ_B to take into account the γ -rays reaching the observer from the direction of the blazar. The Fermi-LAT resolution to a single photon above 10 GeV is $\sim 0.15^\circ$.

[Figure 4.4](#) is the resulting fit corresponding to this model. The green curve

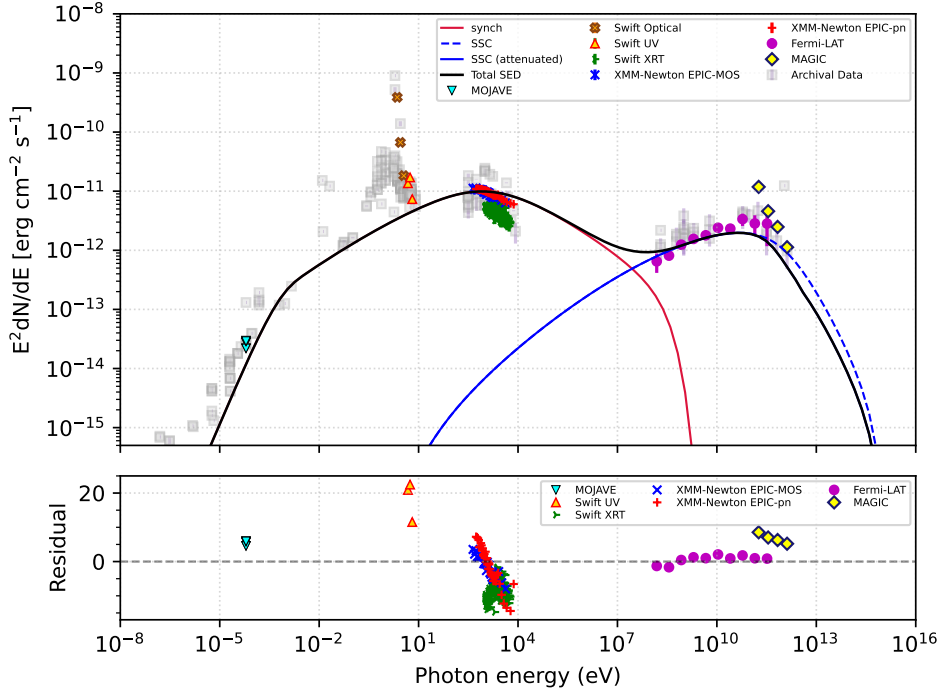


Figure 4.2. Pure leptonic modeling of the multiwavelength SED of Mrk 180 and residual plot corresponding to this modeling. The data color codes are mentioned in the plots.

indicates the spectrum of cosmogenic photons. The required power in UHECR protons is calculated in the following manner [170],

$$P_{\text{UHECR}} = \frac{2\pi d_L^2 (1 - \cos \theta_{\text{jet}})}{\xi_B f_{\text{CR}}} \int_{\epsilon_{\gamma, \text{min}}}^{\epsilon_{\gamma, \text{max}}} \epsilon_{\gamma} \frac{dN}{d\epsilon_{\gamma} dAdt} d\epsilon_{\gamma} \quad (4.8)$$

where d_L is the luminosity distance of Mrk 180, θ_{jet} is jet opening angle, ξ_B is the survival rate of UHECR within 0.1° of the direction of propagation to the observer. The quantity f_{CR} is the fraction of UHECR luminosity that goes into cosmogenic γ -rays and depends on the propagation distance. The integration is done over the cosmogenic photon spectrum allowed by the observed SED, d_L is 207 Mpc, θ_{jet} is 0.1 radians (we have considered typical value of θ_{jet} or jet opening angle) [142, 222], and $\Gamma=20$. For the chosen parameters, $\xi_B = 0.85$ and $f_{\text{CR}} = 0.03$. Putting these values in Equation 4.8, P_{UHECR} has been calculated. Finally, we add up the total kinematic jet power of the relativistic leptons, magnetic field and UHECRs denoted by P_{UHECR} to get the total kinematic jet power for this model to be 2.9×10^{43} erg/s, which is less than the Eddington luminosity of Mrk 180 by several orders of magnitude. The best-fitted values of this model are tabulated in the second column of Table 4.1. In this case, the highest energy MAGIC data point can be fitted, but the fit to the X-ray data points has not improved.

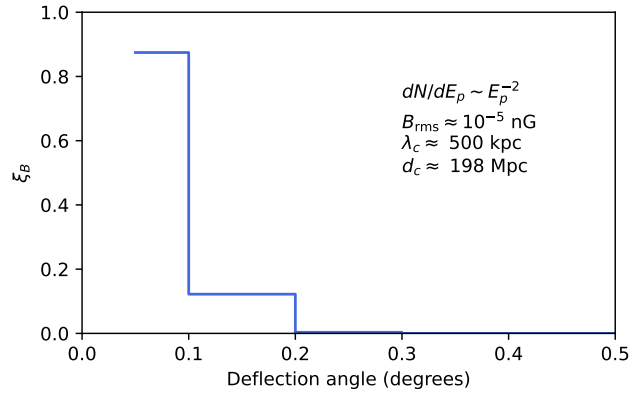


Figure 4.3. Distribution of propagated UHECRs as a function of deflection angle in a random turbulent magnetic field.

We subsequently consider the pp interactions within the jet. As explained in [subsection 4.4.3](#), the relativistically accelerated protons interact with cold protons and produced neutral and charged pions which decay into photons, leptons, and neutrinos. A power-law proton spectrum is injected within the blob with a spectral index $\alpha_p=2.2$, minimum ($E_{p,\min}$) and maximum energy ($E_{p,\max}$) 10 GeV and 10^4 GeV respectively and the cold proton density is assumed to be $n_H=1.2\times 10^6$ cm^{-3} . These parameter values have been presented in the third column of [Table 4.1](#). Previously, Banik and Bhadra [217] showed pp interaction model can explain the observed high-energy γ -rays from the blazar TXS 0506+056 for $n_H = 1.68 \times 10^6$ cm^{-3} . Aharonian [223] showed that high-energy γ -ray production in an AGN jet via pp interaction demands high cold proton density. To interpret the reported TeV flares of Markarian 501 by pp interactions, they showed n_H should exceed 10^6 cm^{-3} .

From [Figure 4.2](#) we can see that the SED from the pure leptonic model cannot fit the Swift UV data points. The slope of the observed X-ray and the γ -ray data points cannot be explained with the slope of the theoretical SED, also it poorly fits the γ -ray data points. The residual plot corresponding to the pure leptonic model shows this model poorly fits the Swift UV data, X-ray, and MAGIC data.

From [Figure 4.4](#) it can be seen that UHECR interactions make the fit better for the MAGIC data points but the slope of the SED from this model does not match the slope of the X-ray data. Moreover, the Swift UV data cannot be fitted well with this model. The residual plot corresponding to this model looks almost the same as that of the pure leptonic model between 10^{-5} - 10^{11} eV, except for the MAGIC data points.

[Figure 4.5](#) shows improvement in both SED and the residuals. The SED fits the Swift UV data points, and matches the slope of the X-ray data and the γ -ray data. The residual plot corresponding to this model shows that the residuals for

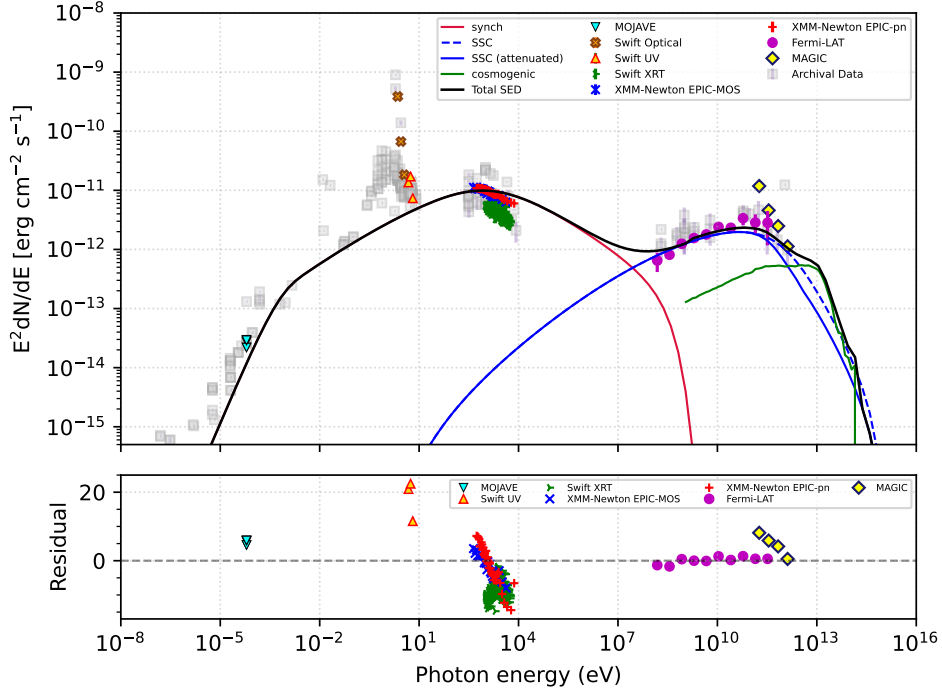


Figure 4.4. Leptonic+hadronic (UHECR) modeling of the multiwavelength SED of Mrk 180 and residual plot corresponding to this modeling.

the Swift UV data points lie in between $\sim \pm 10$, whereas they lie in between +10 to +20 in [Figure 4.2](#) and [Figure 4.4](#). In [Figure 4.5](#), the residuals for the Swift XRT & XMM-Newton EPIC-MOS data lie within ± 10 and the XMM-Newton EPIC-pn data lie out of +10. In the previous two plots i.e. [Figure 4.2](#) and [Figure 4.4](#), all the residuals for the X-ray data points lie within +10 to -20. It is clear from the residual plot that the SED is not very well fitted which is why we are getting large values of the residuals. We have not shown the residuals for the Swift Optical data points, as they cannot be fitted with any of these models. Most of the γ -ray data points can be fitted in this model. The total kinematic jet power corresponding to each model is less than the Eddington luminosity of Mrk 180, which has been mentioned in [Table 4.1](#).

4.5.1 UHECRs from Mrk 180

It has been proposed earlier [7] that Mrk 180 may be a source contributing to the UHECR hotspot observed by the Telescope Array (TA) collaboration above 57 EeV. We propagate UHECRs from the source to the Earth in a random turbulent magnetic field given by the Kolmogorov power spectrum. We consider three different combinations of the RMS value of the EGMF (B_{rms}) and composition at the source as shown in [Figure 4.6](#). The turbulence correlation length of the

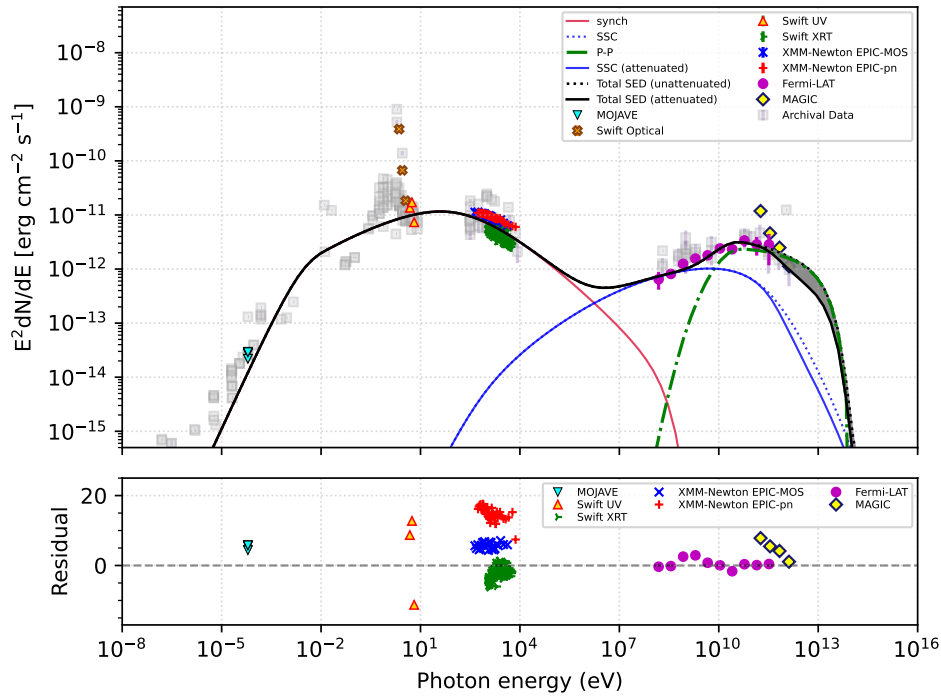


Figure 4.5. Leptonic+hadronic (pp) modeling of the multiwavelength SED of Mrk 180 and residual plot corresponding to this modeling; the gray shaded region denotes the difference between the attenuated and unattenuated regions of the total SED.

EGMF is taken to be 0.5 Mpc. The Galactic magnetic field model (GMF) is considered to be the one given in Jansson and Farrar [224]. We inject cosmic rays with a generic power-law spectrum given by $dN/dE \sim E^{-2}$ and perform three-dimensional simulations including both GMF and EGMF in CRPROPA 3 [212, 213]. We consider two cases of composition with extreme masses, viz., ^1H and ^{56}Fe . For pure proton injection, the magnetic rigidity is higher and the resulting deflection is low.

We show the case of $B_{\text{rms}} \sim 10^{-3}$ nG and 10^{-5} nG in the left and middle panel of Figure 4.6 for proton injection. For the same injected luminosity, the number of detected events in the former case is 35, while that for the latter increases by almost three orders of magnitude. It can be seen that even with Fe injection (cf. right panel in Figure 4.6), the angular width of the source observed through UHECRs doesn't show a significant change; although, the observed energy spectrum is different. Due to the photo-disintegration of the nuclei traversing a comoving distance of ~ 200 Mpc, the observed events at Earth for the energy range considered are all protons. Thus, it can be seen that for optimistic magnetic field values considered, the contribution of this source to the TA hotspot is disfavored, unless, very high magnetic fields $\mathcal{O} \sim 1$ nG or higher are considered. Although a higher spread in

Table 4.1: Results of multi-wavelength SED modeling shown in the [Figure 4.2](#), [Figure 4.4](#), and [Figure 4.5](#)

Parameters	Pure-leptonic model	Leptonic+ hadronic (UHECR) model	Leptonic+ hadronic (pp) model
Spectral index of injected electron spectrum (α)	2.2	2.2	2.2
Curvature index of injected electron spectrum (β)	0.06	0.06	0.10
Magnetic field in emission region (B)	0.10 G	0.10 G	0.10 G
Size of the emission region (R)	8.0×10^{15} cm	8.0×10^{15} cm	1.8×10^{16} cm
Doppler factor (δ_D)	20	20	20
Min. Lorentz factor (γ_{\min})	1.0×10^2	1.0×10^2	2.5×10^2
Max. Lorentz factor (γ_{\max})	9.0×10^7	9.0×10^7	9.0×10^7
Spectral index of relativistic proton spectrum (α_p)	–	2.2	2.2
Min. energy of relativistic protons ($E_{p,\min}$)	–	0.1 EeV	10 GeV
Max. energy of relativistic protons ($E_{p,\max}$)	–	100 EeV	10^4 GeV
Jet power of relativistic leptons (P_e)	2.6×10^{43} erg/s	2.6×10^{43} erg/s	2.2×10^{43} erg/s
Jet power of magnetic field (P_B)	9.6×10^{41} erg/s	9.6×10^{41} erg/s	4.9×10^{42} erg/s
Jet power of relativistic protons (P_p)	–	1.9×10^{42} erg/s	9.8×10^{44} erg/s
Kinematic jet power (P_{tot}^k)	2.7×10^{43} erg/s	2.9×10^{43} erg/s	1.0×10^{45} erg/s

the arrival direction is expected if the detection threshold is lowered, the Galactic magnetic field shadows the directional signatures. Thus, Mrk 180 may not be a plausible UHECR source for explaining the TA hotspot.

4.6 Discussions

Being at a redshift of 0.045, Mrk 180 is an interesting source to study the radiative mechanisms producing TeV γ -rays. VHE γ -ray emission from this source was detected by MAGIC in 2006 [184] followed by an enhanced optical state. This source has been monitored by several telescopes viz. Fermi-LAT, Swift, XMM-Newton, MOJAVE, MAGIC, KVA, ASM, RATAN-600, Metsähovi, Effelsberg, IRAM throughout the year. Previously, Rügamer *et al.* [185, 186] studied this source using multi-wavelength data. They have discussed about the results of the multi-wavelength campaign in 2008 covering radio to TeV γ -ray observations. At that time Mrk 180 was known to be a TeV γ -ray source detected by MAGIC only a

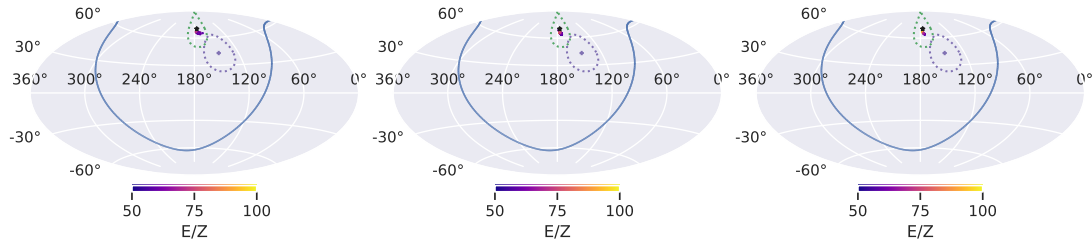


Figure 4.6. Arrival direction of UHECRs at $E > 57$ EeV from Mrk 180 to Earth. The blue line shows the Galactic plane. The purple point and the purple dotted curve show the TA hotspot center and the 20° region around it. Similarly, the green dotted curve shows the 20° region around Mrk 180. The color bar indicates the energy per nucleon (E/z) of the observed events. From left, the figures correspond to (a) pure proton injection and $B_{\text{rms}} \approx 10^{-3}$ nG; (b) pure proton injection and $B_{\text{rms}} \approx 10^{-5}$ nG; (c) Fe injection and $B_{\text{rms}} \approx 10^{-5}$ nG

couple of years back. Their study reported the first multi-wavelength campaign on Mrk 180. Optical observation was carried out by KVA telescope simultaneously with TeV γ -ray observation with MAGIC. The radio observation was carried out with RATAN-600, Metsähovi, Effelsburg, and IRAM. Swift XRT detected flux variability in X-rays. In the same observation window of Swift XRT, Metsähovi and AGILE could not detect this source. Fermi-LAT light curve showed enhancement in γ -ray flux during the second flare.

They tried to explain the simultaneous multi-wavelength SED of Mrk 180 by two models: (1) a one-zone SSC model (2) a self-consistent two-zone SSC model; they considered the injected electron spectrum as a broken power-law distribution. It can be seen in Rügamer *et al.* [185] that during the high state both the models cannot explain the multi-wavelength data properly. The steep X-ray spectrum and high optical flux could not be explained simultaneously assuming they were produced in the same zone. Moreover, in the two-zone SSC model the required value of the Doppler factor δ is very high. During the low X-ray state both the models can explain the SED for moderate values of parameters. Nilsson *et al.* [187] studied R-band long-term optical data (over a span of ~ 10 years) of 31 northern blazars and Mrk 180 is one of them. They could not find any significant periodicity for this source. The earlier multi-wavelength studies on Mrk 180 have been complemented in this work with more data analysis and theoretical modeling of the SED over a long period of observations.

For the temporal study, we analyzed 12.8 years (MJD 54682.65- 59355.67) of Fermi-LAT γ -ray data. Figure 4.1 is the long-term Fermi-LAT γ -ray light curve in 30-day bin. No γ -ray flux enhancement has been found from this long-term light curve, also the error bars of the high-energy γ -ray data points are large to carry on a detailed temporal study on this source. To know about the physical processes

we studied the long-term SED of Mrk 180. For this study, we have used multi-wavelength data from MOJAVE, MAGIC, Swift, XMM-Newton, and Fermi-LAT. The SED shows typically the double hump structure. We have modeled this multi-wavelength SED with GAMERA [172]. We have considered a simple one-zone spherical emission region within the jet. In [Figure 4.2](#), [Figure 4.4](#), and [Figure 4.5](#) we have shown the modeled multi-wavelength SEDs with different models, e.g. pure leptonic, lepto-hadronic. Also, we have shown the residual plots of each model, attached just below that particular SED. The results of the multi-wavelength SED modeling with different models have already been discussed in [section 4.5](#). The leptonic modeling is not sufficient to explain the multi-wavelength SED of Mrk 180. We have considered two lepto-hadronic models to improve the fit to the observed data points. The first model involves interactions of UHECRs injected by Mrk 180 with the radiation backgrounds, and in the second model, we have considered interactions of relativistic protons in the jet with the cold protons. The latter gives a slightly better fit to the data, however, more observational data is necessary to explain the radiation mechanisms in Mrk 180, as our results show large values of residuals in all the cases. We look forward to future multi-wavelength campaigns to cover all the frequencies over a long time period to monitor this source more closely.

He *et al.* [7] calculated the probability associated with some sources to be the contributors to the TA hotspot, Mrk 180 is one of them. It is important to know the role of Mrk 180 as a UHECR accelerator, and whether it can generate events above 57 EeV. In our study for conservative values of EGMF, Mrk 180 is disfavoured as a source of the UHECR events contributing to the TA hotspot. In future, with more observational data it would be interesting to study the association of Mrk 180 with the TA hotspot.

4.7 Conclusion

The HBL Mrk 180, at a redshift of 0.045, is an interesting source to study the emission covering radio to VHE γ -ray frequency. We have analyzed the Fermi-LAT γ -ray data detected from this source over a period of 12.8 years. The light curve analysis does not show any significant variation in flux. We have studied the long-term multi-wavelength SED of this source to understand the physical processes which can explain the HBL nature of this source. We modeled the multi-wavelength SED with a time-dependent code 'GAMERA' [172]. It is found that a single-zone pure leptonic model cannot explain the multi-wavelength spectrum of Mrk 180 properly. We considered single-zone lepto-hadronic models to obtain better fits to the data. The residuals of the three models are compared and the

pp interaction model is found to give a better fit to the multi-wavelength data compared to the other two models. More observational data covering the radio to VHE γ -ray frequency would be useful to explore the emission mechanisms of Mrk 180 and to give a definitive conclusion. The possible association of Mrk 180 with the TA hotspot events above 57 EeV has also been examined using the simulation framework CRPROP3 [212, 213]. In this study we do not find any UHECR event from Mrk 180 contributing to the TA hotspot, hence, we conclude that for conservative values of EGMF, Mrk 180 is disfavoured as a source contributing to the TA hotspot, however, in future with more UHECR data it would be possible to investigate further on their association.

Summary & Future Prospect

5.1 Summary & Future Prospect

5.1.1 Thesis Summary

In this thesis, I discussed about our study on the two BL Lac sources: PKS 0903-57 & Markarian 180 (Mrk 180). We conducted a detailed spectral and temporal studies on these two sources and modeling of the data to understand the underlying physics.

In [chapter 3](#), I mentioned the details of our study on the BL Lac, PKS 0903-57. We analysed ~ 12.4 years (From 4th August 2008 to 6th Jan 2021) Fermi-LAT gamma-ray data of PKS 0903-57. From the 7-Day binned Fermi-LAT gamma-ray lightcurve, we detected two flaring activities in the year 2018 & 2020 and the gamma-ray flux reached in its peak in 2020. We named those two flares as Flare-1 & Flare-2. From further analysis of the smaller binned Fermi-LAT gamma-ray lightcurve and applying the Bayesian block method, we identified multiple sub-structures and phases within the two flaring phases. Flare-1 has one sub-structure, which has two phases: Flare-1A & Flare-1B. Flare 2 has two sub-structures: Flare-I and Flare-II, which have several phases. Flare-I has five phases: Preflare-I, Flare-IA, Flare-IB, Flare-IC & Postflare-I. Flare-II has three phases: Preflare-II, Flare-II & Postflare-II.

We have fitted Flare-1A, Flare-1B, Flare-IA, Flare-IB, Flare-IC & Flare-II with an exponential functional form and calculated the rising and decay time of the peaks of each of the six ‘flares’. We computed the gamma-ray variability time of this source, which we found to be 1.7 ± 0.9 hour. No particular pattern in rise and decay was found in our study.

For spectral analysis, first we extracted the Fermi-LAT gamma-ray SEDs of different phases and fitted with PL (PowerLaw), LP (LogParabola), BPL (Broken-PowerLaw) & PLEC (PowerLaw with Exponential Cutoff) to find which functional form gives a good fit to the observational data. From the maximum likelihood analysis of the Fermi-LAT gamma-ray data, we found the best-fitted model corresponding to each phase. For the multi-wavelength study, we checked the publicly available multi-wavelength data. Other than Fermi-LAT, we found only Swift XRT, Swift UVOT, and ATCA have simultaneous data corresponding to the four phases

of our interest. We analysed Swift XRT & UVOT data and compiled the ATCA data, which was available during Flare-1B. We constructed the multi-wavelength SEDs of Flare-1B, Flare-1A, Flare-1B & Flare-1C, and for these phases, LP was found to be the best-fitted model. The multi-wavelength SEDs of these four phases have been modeled with a time-dependent open code, 'GAMERA' [171, 172]. We modeled those SEDs considering a single-zone pure leptonic model. We tabulated the fitted parameters, e.g. magnetic field (B), Doppler factor (δ), spectral index (α), curvature index (β), size of the emission region (R) etc. and estimated the total jet power of the four phases which we found to be a few times 10^{46} erg/sec. We maintained the charge neutrality condition of the blazar jet. Also, during the modeling, we considered a few assumptions, e.g., the spherical shape of the emission region and the constant escape rate of the leptons from the emission blob. From our study, we found that more simultaneous multi-wavelength data would be helpful to understand the underlying physical mechanism of this source. The highlights of our study on PKS 0903-57 are listed below.

- The Fermi LAT γ -ray lightcurve shows two flares in 2018 and in 2020, named as Flare-1 & Flare-2 respectively.
- Flare-1 has one sub-structure which has two phases.
- Flare-2 has two sub-structures. Each of them has multiple phases.
- The gamma-ray variability time of this source is found to be 1.7 ± 0.9 hour.
- No particular pattern of rise and decay of the flares was found.
- Fermi-LAT and HESS detected very-high-energy gamma-rays from PKS 0903-57; due to its low redshift EBL absorption of gamma-rays is negligible.
- Very-high-energy gamma rays are detected during flares.
- Currently no estimate is available for the black hole mass of this source.
- The jet power of each flare is of the order of 10^{46} erg/sec, which is lower than the most commonly expected Eddington luminosity for this class of objects.

In [chapter 4](#), I discussed the details of our study on the HBL, Mrk 180. We analyzed the Fermi-LAT gamma-ray data of Mrk 180 over a period of 12.8 years. The long-term light curve analysis does not show any significant variation in the Fermi-LAT gamma-ray flux.

To understand the physical processes which can explain the multi-wavelength emission of this source, we studied the long-term multi-wavelength SED of Mrk 180. We modeled the multi-wavelength SED with a time-dependent code ‘GAMERA’ [171, 172]. The MWSED has been modeled with one-zone pure leptonic and lepto-hadronic scenarios. The pure leptonic model and the two lepto-hadronic models, viz., (i) line-of-sight interactions of UHECRs with the cosmic background radiation and (ii) the interactions of relativistic protons with the cold protons in the jet, have been compared in this work. It was found that a single-zone pure leptonic model cannot properly explain the multi-wavelength spectrum of Mrk 180. We considered single-zone lepto-hadronic models to obtain better fits to the data. The residuals of the three models are compared, and the pp interaction model is found to be a better fit for the multi-wavelength data than the other two models. However, we found that more observational data covering the radio to VHE gamma-ray frequency would be useful in exploring the emission mechanisms of Mrk 180 to give a definitive conclusion.

Moreover, an earlier study has associated Mrk 180 with the Telescope Array (TA) hotspot of UHECRs at energy more than 57 EeV [225]. This speculation motivates us to check whether ultrahigh energy protons and iron nuclei can reach the earth from Mrk 180, using the simulation framework CRPROPA 3 [226, 227]. After comparing the results of our simulation with the current observational data, we do not find any UHECR event from Mrk 180 contributing to the TA hotspot, hence, we concluded that for conservative values of EGMF, Mrk 180 is disfavoured as a source contributing to the TA hotspot, however, in future with more UHECR data it would be possible to investigate further on their association. Here are the highlights of our study on Mrk 180.

- Mrk 180 is less studied and earlier associated with UHECR event.
- The long-term Fermi-LAT gamma-ray lightcurve did not show any significant flux enhancement which was feasible for further detail temporal study.
- Multi-wavelength data is explained with lepto-hadronic model, single zone pure leptonic model cannot explain all the data.
- Single zone leptonic model combined with pp interaction model gives the most satisfactory fit to the data.
- Our study disfavours Mrk 180 as a source of TA hotspot events for conservative values of EGMF.

5.1.2 Future Prospect

BL Lacs belong to a special class of AGNs, having distinctive features, e.g. rapid and large-amplitude flux variability and high degree of optical polarization. Even after 50 years of their discovery, many aspects of these sources have remained unclear, e.g., their jet magnetic field structure, the cause of variability in multi-wavelength jet emission in different timescales, particle acceleration mechanism, jet launching mechanism etc. The scientific community is closely observing these sources with many detectors. For a better understanding of these sources, simultaneous multi-wavelength data is required. Telescopes with better sensitivity over a broad range in energy and response to temporal variation in photon flux covering a large portion of the sky would be ideal for detecting any small amount of flux variation in any waveband in a short time.

Fermi-LAT can detect gamma rays in the range of 20 MeV to 300 GeV [228]. Beyond several hundreds of GeV, very-high-energy (VHE) gamma-rays are detected by Major Atmospheric Gamma Imaging Cherenkov (MAGIC), High Energy Stereoscopic System (H.E.S.S.), and Very Energetic Radiation Imaging Telescope Array System (VERITAS; [229]). There is another observatory, High-Altitude Water Cherenkov Gamma-Ray Observatory (HAWC; [230, 231]), which mainly detects VHE gamma-rays and cosmic rays. All these telescopes have some observational limitations, e.g., limitations in sensitivity, limitations in energy range and sky-coverage. The already functioning Large High Altitude Air Shower Observatory (LHAASO; [232]) and upcoming Cherenkov Telescope Array (CTA; [233]) have been designed (cf. [Figure 5.1a](#)) to perform much better compared to the other VHE gamma-ray telescopes mentioned above. Once CTA is fully operational, it will undoubtedly enrich our knowledge in the regime of VHE gamma-ray astronomy.

As mentioned before, multi-wavelength observation is very important for studying the AGNs. Currently, there are several telescopes operating in other frequencies, e.g., SWIFT, XMM-Newton, Chandra and NuSTAR in X-ray frequencies, SMARTS in optical and infrared and OVRO in radio frequencies. There is 'Blazar Monitoring Program' ([Major Blazar Monitoring Programs](#)) in which different observatories are collecting data in different frequency ranges. They monitor a few blazars out of the thousands of blazars [236] distributed all over the sky. Moreover, the important job is to establish a faster communication channel between different observatories and astronomical facilities to enable a real-time coincidence search from a particular source. This will help us to locate the position of the source and follow-up on that event by different observatories or telescopes to identify its counterparts. This trigger and follow-up alert-generate

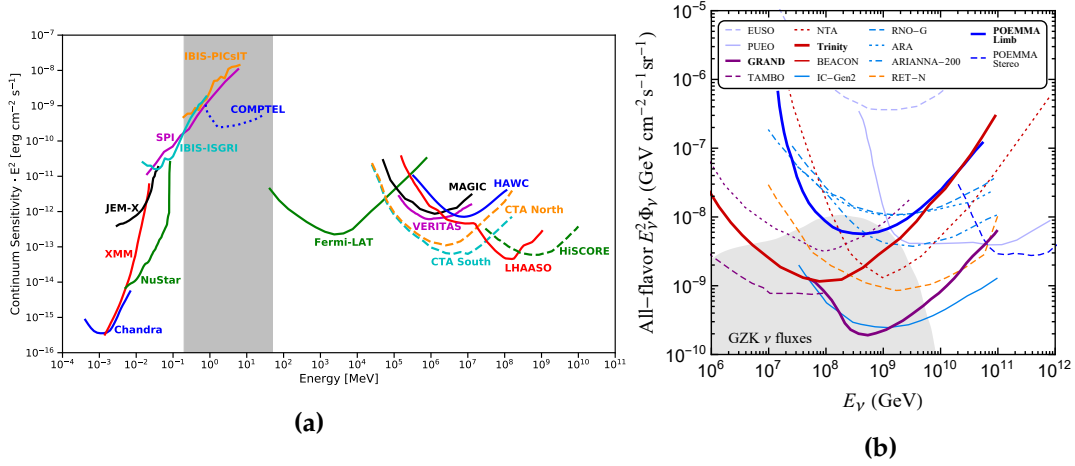


Figure 5.1. (5.1a) Sensitivity plot of different X-ray and gamma-ray instruments (Image Credit: Lucchetta *et al.* [234]). (5.1b) Projected sensitivities of future neutrino telescopes (All-flavor cosmogenic neutrino flux above PeV energies.) (Image Credit: Huang *et al.* [235]).

system is an important part of the communication channel. Currently, there are a few such channels, e.g., ‘General Coordinate Network’ (GCN), ‘Astrophysical Multimessenger Observatory Network’ AMON [237, 238], the ‘Astronomer’s Telegram’ *Astronomer’s Telegram*, ‘Astro-Colibri’ (*Astro-Colibri*) through which we can receive immediate alert messages upon the detection of any transient phenomenon and subsequent updates on any follow-up observation, conducted by the same or other observatories or astronomical facilities.

In 2017, 22nd September, IceCube detected a very-high-energy neutrino ($E \sim 290$ TeV) which was coincident spatially and temporally with a gamma-ray flaring blazar TXS 0506+056 [239], suggesting that the blazar might be a source of high-energy neutrinos. After IceCube reported the detection of such a very-high-energy neutrino event, an extensive multi-wavelength campaign was carried out [240] by several astronomical facilities (Figure 5.2). Subsequently, more high-energy neutrino events were found to be spatially coincident with different blazars, and sometimes these events were temporally coincident with the high-flux state of the sources.

- (i) IC211208A was found to be in spatial and temporal coincidence with the high state of PKS 0735+178 in optical, UV, X-ray and GeV gamma-ray band [241].
- (ii) Similarly, PKS 1502+106 was found to be in spatial coincidence with an IceCube neutrino event IC190730A [242]. However, during the time of the neutrino event, the source did not exhibit flaring activity in the gamma-ray waveband. Though, multi-wavelength study and modeling suggest that PKS

1502+106 could be considered as a neutrino emitter [243–245].

- (iii) 3HSP J095507.1+355100, an extreme and high-synchrotron peaked BL Lac, was found to be in spatial and temporal association with a neutrino event IC200107A during its X-ray flaring state [246, 247].
- (iv) A study for searching an excess of clustered astrophysical neutrino events from pointlike sources ($E \gtrsim 1$ TeV) was carried out using 10 years of IceCube neutrino data. It was found that other than the above three sources, there are two more BL Lacs, viz., PKS 1424+240 and GB6 J1542+6129, which exhibited significant neutrino excess [248].

All these neutrino-blazar associations supported the speculation of hadronic interactions within the blazar jets. Besides neutrino, blazars are considered to be sites of UHECR acceleration [249, 250]. In [chapter 2](#), I mentioned, He *et al.* [225] found the possibility that the BL Lac, Mrk 180 is a UHECR accelerator contributing to the TA hotspot array. A previous study by Tinyakov and Tkachev [251] mentioned the possibility of the BL Lac objects as source of UHECRs. To investigate the association of high-energy or VHE neutrino or UHECRs, multi-messenger follow-up is required.

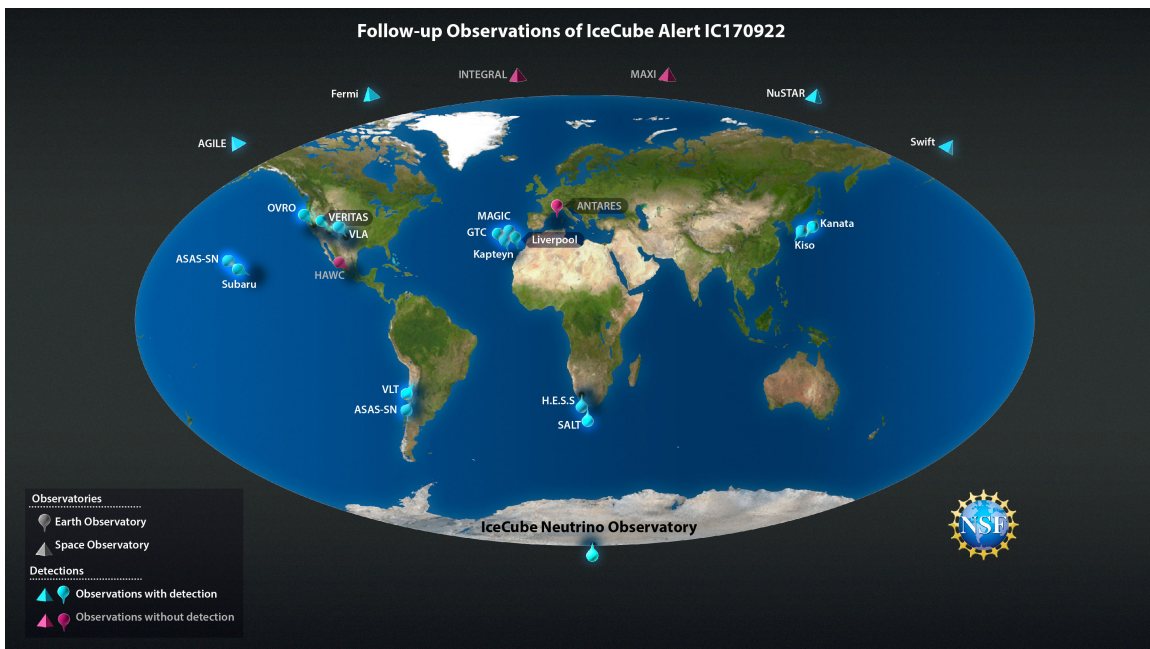


Figure 5.2. Follow-up observation of IceCube alert IC170922. (Image Courtesy: National Science Foundation ([link](#)))

With the development of science, mysteries unfold. And the same thing we can expect to happen with the upgradation of the astronomical facilities and observatories. Once telescopes, viz., CTA, IceCube-Gen2 [252, 253] ([Figure 5.1b](#)),

Radio Neutrino Observatory Greenland (RNO-G; [254]), and Giant Radio Array for Neutrino Detection (GRAND; [255]) start their function fully; sooner or later, all those unanswered questions will be answered.

References

- [1] C. M. Urry and P. Padovani, [Publications of the Astronomical Society of the Pacific](#) **107**, 803 (1995).
- [2] F. Aharonian, A. G. Akhperjanian, A. R. Bazer-Bachi, B. Behera, M. Beilicke, W. Benbow, D. Berge, K. Bernlöhr, C. Boisson, O. Bolz, V. Borrel, T. Bouteiller, I. Braun, E. Brion, A. M. Brown, R. Bühler, I. Büsching, T. Bulik, S. Carigan, P. M. Chadwick, A. C. Clapson, L. M. Chounet, G. Coignet, R. Cornils, L. Costamante, B. Degrange, H. J. Dickinson, A. Djannati-Ataï, W. Domainko, L. O. Drury, G. Dubus, J. Dyks, K. Egberts, D. Emmanoulopoulos, P. Espigat, C. Farnier, F. Feinstein, A. Fiasson, A. Förster, G. Fontaine, S. Funk, S. Funk, M. Fülling, Y. A. Gallant, B. Giebels, J. F. Glicenstein, B. Glück, P. Goret, C. Hadjichristidis, D. Hauser, M. Hauser, G. Heinzlmann, G. Henri, G. Hermann, J. A. Hinton, A. Hoffmann, W. Hofmann, M. Holleran, S. Hoppe, D. Horns, A. Jacholkowska, O. C. de Jager, E. Kendziorra, M. Kerschhaggl, B. Khélifi, N. Komin, K. Kosack, G. Lamanna, I. J. Latham, R. Le Gallou, A. Lemièrre, M. Lemoine-Goumard, J. P. Lenain, T. Lohse, J. M. Martin, O. Martineau-Huynh, A. Marcowith, C. Masterson, G. Maurin, T. J. L. McComb, R. Moderski, E. Moulin, M. de Naurois, D. Nedbal, S. J. Nolan, J. P. Olive, K. J. Orford, J. L. Osborne, M. Ostrowski, M. Panter, G. Pedalletti, G. Pelletier, P. O. Petrucci, S. Pita, G. Pühlhofer, M. Punch, S. Ranchon, B. C. Raubenheimer, M. Raue, S. M. Rayner, M. Renaud, J. Ripken, L. Rob, L. Rolland, S. Rosier-Lees, G. Rowell, B. Rudak, J. Ruppel, V. Sahakian, A. Santangelo, L. Saugé, S. Schlenker, R. Schlickeiser, R. Schröder, U. Schwanke, S. Schwarzbarg, S. Schwemmer, A. Shalchi, H. Sol, D. Spangler, Ł. Stawarz, R. Steenkamp, C. Stegmann, G. Superina, P. H. Tam, J. P. Tavernet, R. Terrier, C. van Eldik, G. Vasileiadis, C. Venter, J. P. Vialle, P. Vincent, M. Vivier, H. J. Völk, F. Volpe, S. J. Wagner, M. Ward, and A. A. Zdziarski, [Astrophysical Journal Letters](#) **664**, L71 (2007), [arXiv:0706.0797 \[astro-ph\]](#).
- [3] C. M. Raiteri, M. Villata, F. D’Ammando, V. M. Larionov, M. A. Gurwell, D. O. Mirzaqulov, P. S. Smith, J. A. Acosta-Pulido, I. Agudo, M. J. Arévalo, R. Bachev, E. Benítez, A. Berdyugin, D. A. Blinov, G. A. Borman, M. Böttcher, V. Bozhilov, M. I. Carnerero, D. Carosati, C. Casadio, W. P. Chen, V. T. Doroshenko, Y. S. Efimov, N. V. Efimova, S. A. Ehgamberdiev, J. L. Gómez, P. A. González-Morales, D. Hiriart, S. Ibryamov, Y. Jadhav, S. G. Jorstad, M. Joshi, V. Kadenius, S. A. Klimanov, M. Kohli, T. S. Konstantinova, E. N. Kopatskaya, E. Koptelova, G. Kimeridze, O. M. Kurtanidze, E. G. Larionova, L. V. Larionova, R. Ligustri, E. Lindfors, A. P. Marscher, B. McBreen, I. M. McHardy, Y. Metodiev, S. N. Molina, D. A. Morozova, S. V. Nazarov, M. G. Nikolashvili, K. Nilsson, D. N. Okhmat, E. Ovcharov, N. Panwar, M. Pasanen, S. Peneva, J. Phipps, N. G. Pulatova, R. Reinthal, J. A. Ros, A. C. Sadun, R. D. Schwartz, E. Semkov, S. G. Sergeev, L. A. Sigua, A. Sillanpää, N. Smith, K. Stoyanov, A. Strigachev, L. O. Takalo, B. Taylor, C. Thum, I. S. Troitsky, A. Valcheva, A. E. Wehrle, and H. Wiesemeyer, [Monthly Notices of the Royal Astronomical Society](#) **436**, 1530 (2013), [arXiv:1309.1282 \[astro-ph.HE\]](#).
- [4] C. Tchernin, J. A. Aguilar, A. Neronov, and T. Montaruli, [Nuclear Instruments and Methods in Physics Research A](#) **742**, 191 (2014).
- [5] R. Blandford, D. Meier, and A. Readhead, [Ann. Rev. Astron. Astrophys.](#) **57**, 467 (2019), [arXiv:1812.06025 \[astro-ph.HE\]](#).
- [6] M. Cerruti, [Galaxies](#) **8**, 72 (2020), [arXiv:2012.13302 \[astro-ph.HE\]](#).
- [7] H.-N. He, A. Kusenko, S. Nagataki, B.-B. Zhang, R.-Z. Yang, and Y.-Z. Fan, [Phys. Rev. D](#) **93**, 043011 (2016).
- [8] G. di Sciascio and Lhaaso Collaboration, [Nuclear and Particle Physics Proceedings](#) **279-281**, 166 (2016), [arXiv:1602.07600 \[astro-ph.HE\]](#).
- [9] M. Agostini *et al.* (P-ONE), [Nature Astron.](#) **4**, 913 (2020), [arXiv:2005.09493 \[astro-ph.HE\]](#).
- [10] W. History, “Astrolabe,”.
- [11] E. A. Fath, [Lick Observatory Bulletin](#) **149**,

- 71 (1909).
- [12] H. Curtis, “Curious straight ray,” .
- [13] C. K. Seyfert, *Astrophysical Journal* **97**, 28 (1943).
- [14] C. Hazard, M. B. Mackey, and A. J. Shimmins, *Nature* **197**, 1037 (1963).
- [15] E. R. Waluska, *Journal of Astronomical History and Heritage* **10**, 79 (2007).
- [16] R. A. Sramek and D. W. Weedman, *The Astrophysical Journal* **238**, 435 (1980).
- [17] K. I. Kellermann, R. Sramek, M. Schmidt, D. B. Shaffer, and R. Green, *The Astronomical Journal* **98**, 1195 (1989).
- [18] J. T. Stocke, S. L. Morris, R. J. Weymann, and C. B. Foltz, *The Astrophysical Journal* **396**, 487 (1992).
- [19] C. Tadhunter, *New Astronomy Reviews* **52**, 227 (2008), active Galactic Nuclei at the Highest Angular Resolution: Theory and Observations.
- [20] B. M. Peterson, *An Introduction to Active Galactic Nuclei* (Cambridge, 1997).
- [21] M. M. Phillips and D. E. Osterbrock, *Publications of the Astronomical Society of the Pacific* **87**, 949 (1975).
- [22] D. E. Osterbrock, A. T. Koski, and M. M. Phillips, *The Astrophysical Journal* **206**, 898 (1976).
- [23] A. Capetti, F. Massaro, and R. D. Baldi, *Astronomy & Astrophysics* **598**, A49 (2017).
- [24] B. L. Fanaroff and J. M. Riley, *Monthly Notices of the Royal Astronomical Society* **167**, 31P (1974), <https://academic.oup.com/mnras/article-pdf/167/1/31P/8079923/mnras167-031P.pdf> .
- [25] R. D. Blandford and M. J. Rees, *Physica Scripta* **17**, 265 (1978).
- [26] A. P. Marscher and S. G. Jorstad, *Universe* **8**, 644 (2022).
- [27] K. K. Singh and P. J. Meintjes, *Astron. Nachr.* **341**, 713 (2020), [arXiv:2006.05166 \[astro-ph.HE\]](https://arxiv.org/abs/2006.05166) .
- [28] G. Ghisellini, F. Tavecchio, L. Foschini, and G. Ghirlanda, *Monthly Notices of the Royal Astronomical Society* **414**, 2674 (2011), <https://academic.oup.com/mnras/article-pdf/414/3/2674/3545675/mnras0414-2674.pdf> .
- [29] R. M. Sambruna, *The Astrophysical Journal* **487**, 536 (1997).
- [30] F. Panessa, R. D. Baldi, A. Laor, P. Padovani, E. Behar, and I. McHardy, *Nature Astronomy* **3**, 387 (2019), [arXiv:1902.05917 \[astro-ph.GA\]](https://arxiv.org/abs/1902.05917) .
- [31] J. F. Radcliffe, P. Barthel, M. Garrett, R. Beswick, A. Thomson, and T. Muxlow, *Astronomy & Astrophysics* **649**, L9 (2021).
- [32] A. S. Wilson and E. J. M. Colbert, *The Astrophysical Journal* **438**, 62 (1995).
- [33] M. Schmidt and R. F. Green, *The Astrophysical Journal* **269**, 352 (1983).
- [34] E. E. Khachikian and D. W. Weedman, *Astrofizika* **7**, 389 (1971).
- [35] E. Y. Khachikian and D. W. Weedman, *The Astrophysical Journal* **192**, 581 (1974).
- [36] D. E. Osterbrock, *The Astrophysical Journal* **215**, 733 (1977).
- [37] D. E. Osterbrock, *The Astrophysical Journal* **249**, 462 (1981).
- [38] T. M. Heckman, *Astronomy and Astrophysics* **87**, 142 (1980).
- [39] L. C. Ho, A. V. Filippenko, and W. L. Sargent, *The Astrophysical Journal Supplement* **98**, 477 (1995).
- [40] A. Krabbe, C. Jr, I. Zinchenko, J. Hernandez-Jimenez, O. Dors Junior, G. Hagele, M. Cardaci, and N. Telles, *Monthly Notices of the Royal Astronomical Society* **505** (2021), [10.1093/mnras/stab1346](https://doi.org/10.1093/mnras/stab1346).
- [41] I. Márquez, J. Masegosa, O. González-Martin, L. Hernández-García, M. Pović, H. Netzer, S. Cazzoli, and A. del Olmo, *Frontiers in Astronomy and Space Sciences* **4**, 34 (2017).
- [42] J. Frank, A. King, and D. Raine, *Accretion Power in Astrophysics*, 3rd ed. (Cambridge University Press, 2002).
- [43] I. Robson, *Active galactic nuclei* (Wiley-Praxis Series in Astronomy and Astrophysics, 1996).
- [44] N. I. Shakura and R. A. Sunyaev, *Astronomy and Astrophysics* **24**, 337 (1973).
- [45] A. Koratkar and O. Blaes, *Publications of the Astronomical Society of the Pacific* **111**, 1 (1999).
- [46] B. Czerny, in *AGN Variability from X-Rays to Radio Waves*, Astronomical Society of the Pacific Conference Series, Vol. 360, edited by C. M. Gaskell, I. M. McHardy, B. M. Peterson, and S. G. Sergeev (2006) p. 265.
- [47] B. M. Peterson, in *Physics of Active Galactic Nuclei at all Scales*, Vol. 693, edited by D. Alloin (Physics of Active Galactic Nuclei at all Scales, 2006) p. 77.
- [48] L. Popović, *Open Astronomy* **29**, 1 (2020).
- [49] O. Doré *et al.* (SPHEREx), *arXiv preprint arXiv:1606.07039* (2016), [1606.07039 \[astro-ph.CO\]](https://arxiv.org/abs/1606.07039) .
- [50] P. Padovani, *Frontiers in Astronomy and Space Sciences* **4**, 35 (2017).
- [51] M. Stalevski, C. Ricci, Y. Ueda,

- P. Lira, J. Fritz, and M. Baes, *Monthly Notices of the Royal Astronomical Society* **458**, 2288 (2016), <https://academic.oup.com/mnras/article-pdf/458/3/2288/8005569/stw444.pdf> .
- [52] M. Nenkova, M. M. Sirocky, Ž. Ivezić, and M. Elitzur, *The Astrophysical Journal* **685**, 147 (2008), arXiv:0806.0511 [astro-ph] .
- [53] M. A. Dopita, C. Heisler, S. Lumsden, and J. Bailey, *The Astrophysical Journal* **498**, 570 (1998).
- [54] M.-Y. Zhuang, L. C. Ho, and J. Shang-guan, *Astrophys. J.* **862**, 118 (2018), arXiv:1806.03783 [astro-ph.GA] .
- [55] A. Mizuta, S. Yamada, and H. Takabe, *Journal of Korean Astronomical Society* **34**, 329 (2001).
- [56] F. Yuan and R. Narayan, *Ann. Rev. Astron. Astrophys.* **52**, 529 (2014), arXiv:1401.0586 [astro-ph.HE] .
- [57] R. D. Blandford and A. König, *Astrophys. J.* **232**, 34 (1979).
- [58] J. Magorrian, S. Tremaine, D. Richstone, R. Bender, G. Bower, A. Dressler, S. Faber, K. Gebhardt, R. Green, C. Grillmair, *et al.*, *The Astronomical Journal* **115**, 2285 (1998).
- [59] J. Silk and M. J. Rees, *Astron. Astrophys.* **331**, L1 (1998), arXiv:astro-ph/9801013 .
- [60] R. Antonucci, *Ann. Rev. Astron. Astrophys.* **31**, 473 (1993).
- [61] D. E. Arredondo, O. G. Martín, D. Dultzin, J. Masegosa, C. R. Almeida, I. G. Bernete, J. Fritz, and N. O. Clavijo, arXiv preprint arXiv:2104.11263 (2021).
- [62] C. Hoffmeister, *Astronomische Nachrichten* **236**, 233 (1929).
- [63] J. M. McLeod, J. Swenson, G. M., K. S. Yang, and J. R. Dickel, *The Astrophysical Journal* **70**, 756 (1965).
- [64] J. L. SCHMITT, *Nature* **218**, 663 (1968).
- [65] B. H. ANDREW, J. M. MACLEOD, J. L. LOCKE, W. J. MEDD, and C. R. PURTON, *Nature* **223**, 598 (1969).
- [66] W. A. Stein, S. L. O'Dell, and P. A. Strittmatter, *Annual Review of Astronomy and Astrophysics* **14**, 173 (1976).
- [67] A. G. Markowitz *et al.*, *Mon. Not. Roy. Astron. Soc.* **513**, 1662 (2022), arXiv:2206.03874 [astro-ph.HE] .
- [68] B.-K. Zhang, S. Wang, X.-Y. Zhao, B.-Z. Dai, and M. Zha, *Monthly Notices of the Royal Astronomical Society* **428**, 3630 (2012), <https://academic.oup.com/mnras/article-pdf/428/4/3630/18451352/sts296.pdf> .
- [69] A. Goyal, *Galaxies* **6** (2018), 10.3390/galaxies6010034.
- [70] A. Pandey and C. S. Stalin, *Astron. Astrophys.* **668**, A152 (2022), arXiv:2210.00799 [astro-ph.HE] .
- [71] V. Chitnis, A. Shukla, K. P. Singh, J. Roy, S. Bhattacharyya, S. Chandra, and G. Stewart, *Galaxies* **8** (2020), 10.3390/galaxies8030063.
- [72] P. Padovani and P. Giommi, *The Astrophysical Journal* **444**, 567 (1995), arXiv:astro-ph/9412073 [astro-ph] .
- [73] P. Padovani and P. Giommi, *Monthly Notices of the Royal Astronomical Society* **277**, 1477 (1995), <https://academic.oup.com/mnras/article-pdf/277/4/1477/4301538/mnras277-1477.pdf> .
- [74] L. Costamante, G. Ghisellini, P. Giommi, G. Tagliaferri, A. Celotti, M. Chiantera, G. Fossati, L. Maraschi, F. Tavecchio, A. Treves, *et al.*, *Astronomy & Astrophysics* **371**, 512 (2001).
- [75] R. D. Blandford and A. König, *The Astrophysical Journal* **232**, 34 (1979).
- [76] G. B. Rybicki and A. P. Lightman, *Radiative processes in astrophysics* (Wiley, 1979).
- [77] J. Zhang, E.-W. Liang, S.-N. Zhang, and J. M. Bai, *The Astrophysical Journal* **752**, 157 (2012).
- [78] B. Rani, T. P. Krichbaum, A. P. Marscher, J. A. Hodgson, L. Fuhrmann, E. Angelakis, S. Britzen, and J. A. Zensus, *Astronomy and Astrophysics* **578**, A123 (2015), arXiv:1503.04218 [astro-ph.HE] .
- [79] C. M. Raiteri, M. Villata, J. A. Acosta-Pulido, I. Agudo, A. A. Arkharov, R. Bachev, G. V. Baida, E. Benítez, G. A. Borman, W. Boschin, V. Bozhilov, M. S. Butuzova, P. Calciolone, M. I. Carnerero, D. Carosati, C. Casadio, N. Castro-Segura, W. P. Chen, G. Damjanovic, F. D'Ammando, A. di Paola, J. Echevarría, N. V. Efimova, S. A. Ehgamberdiev, C. Espinosa, A. Fuentes, A. Giunta, J. L. Gómez, T. S. Grishina, M. A. Gurwell, D. Hiriart, H. Jermak, B. Jordan, S. G. Jorstad, M. Joshi, E. N. Kopatskaya, K. Kuratov, O. M. Kurtanidze, S. O. Kurtanidze, A. Lähteenmäki, V. M. Larionov, E. G. Larionova, L. V. Larionova, C. Lázaro, C. S. Lin, M. P. Malmrose, A. P. Marscher, K. Matsumoto, B. McBreen, R. Michel, B. Mihov, M. Mineev, D. O. Mirzaqulov, A. A. Mokrushina, S. N. Molina, J. W. Moody, D. A. Morozova, S. V. Nazarov, M. G. Nikolashvili, J. M. Ohlert, D. N. Okhmat,

- E. Ovcharov, F. Pinna, T. A. Polakis, C. Protasio, T. Pursimo, F. J. Redondo-Lorenzo, N. Rizzi, G. Rodriguez-Coira, K. Sadakane, A. C. Sadun, M. R. Samal, S. S. Savchenko, E. Semkov, B. A. Skiff, L. Slavcheva-Mihova, P. S. Smith, I. A. Steele, A. Strigachev, J. Tammi, C. Thum, M. Tornikoski, Y. V. Troitskaya, I. S. Troitsky, A. A. Vasilyev, and O. Vince, *Nature* **552**, 374 (2017), [arXiv:1712.02098](https://arxiv.org/abs/1712.02098) [astro-ph.HE].
- [80] R. J. Protheroe, *Publications of the Astronomical Society of Australia* **19**, 486 (2002).
- [81] L. D. Gesu, I. Donnarumma, F. Tavecchio, I. Agudo, T. Barnounin, N. Cibrario, N. D. Lalla, A. D. Marco, J. Escudero, M. Errando, S. G. Jorstad, D. E. Kim, P. M. Kouch, I. Liodakis, E. Lindfors, G. Madejski, H. L. Marshall, A. P. Marscher, R. Middei, F. Muleri, I. Myserlis, M. Negro, N. Omodei, L. Pacciani, A. Paggi, M. Perri, S. Puccetti, L. A. Antonelli, M. Bachetti, L. Baldini, W. H. Baumgartner, R. Bellazzini, S. Bianchi, S. D. Bongiorno, R. Bonino, A. Brez, N. Bucciantini, F. Capitanio, S. Castellano, E. Cavazzuti, S. Ciprini, E. Costa, A. D. Rosa, E. D. Monte, V. Doroshenko, M. Dovčiak, S. R. Ehlert, T. Enoto, Y. Evangelista, S. Fabiani, R. Ferrazzoli, J. A. Garcia, S. Gunji, K. Hayashida, J. Heyl, W. Iwakiri, V. Karas, T. Kitaguchi, J. J. Kolodziejczak, H. Krawczynski, F. L. Monaca, L. Latronico, S. Maldera, A. Manfreda, F. Marin, A. Marinucci, F. Massaro, G. Matt, I. Mitsuishi, T. Mizuno, C.-Y. Ng, S. L. O'Dell, C. Oppedisano, A. Papitto, G. G. Pavlov, A. L. Peirson, M. Pesce-Rollins, P.-O. Petrucci, M. Pilia, A. Possenti, J. Poutanen, B. D. Ramsey, J. Rankin, A. Ratheesh, R. W. Romani, C. Sgrò, P. Slane, P. Soffitta, G. Spandre, T. Tamagawa, R. Taverna, Y. Tawara, A. F. Tennant, N. E. Thomas, F. Tombesi, A. Trois, S. Tsygankov, R. Turolla, J. Vink, M. C. Weisskopf, K. Wu, F. Xie, and S. Zane, *The Astrophysical Journal Letters* **938**, L7 (2022).
- [82] P. S. Smith, G. G. Williams, G. D. Schmidt, A. M. Diamond-Stanic, and D. L. Means, *The Astrophysical Journal* **663**, 118 (2007).
- [83] T. Hovatta, E. Lindfors, D. Blinov, V. Pavlidou, K. Nilsson, S. Kiehlmann, E. Angelakis, V. Fallah Ramazani, I. Liodakis, I. Myserlis, G. V. Panopoulou, and T. Pursimo, *Astronomy & Astrophysics* **596**, A78 (2016), [arXiv:1608.08440](https://arxiv.org/abs/1608.08440) [astro-ph.HE].
- [84] F. Tavecchio, M. Landoni, L. Sironi, and P. Coppi, *Monthly Notices of the Royal Astronomical Society* **480**, 2872 (2018), <https://academic.oup.com/mnras/article-pdf/480/3/2872/25500460/sty1491.pdf>.
- [85] A. H. Compton, *Phys. Rev.* **21**, 483 (1923).
- [86] G. R. BLUMENTHAL and R. J. GOULD, *Rev. Mod. Phys.* **42**, 237 (1970).
- [87] E. Prandini and G. Ghisellini, *Galaxies* **10** (2022), 10.3390/galaxies10010035.
- [88] S. K. Mondal, S. Das, and N. Gupta, *Astrophys. J.* **948**, 75 (2023), [arXiv:2212.07331](https://arxiv.org/abs/2212.07331) [astro-ph.HE].
- [89] K. Mannheim, *Science* **279**, 684 (1998), [arXiv:astro-ph/9803241](https://arxiv.org/abs/astro-ph/9803241) [astro-ph].
- [90] C. Tchernin, J. Aguilar, A. Neronov, and T. Montaruli, *Nuclear Instruments and Methods in Physics Research Section A: Accelerators, Spectrometers, Detectors and Associated Equipment* **742**, 191 (2014), 4th Roma International Conference on Astroparticle Physics.
- [91] R. Blandford, D. Meier, and A. Readhead, *Annual Review of Astronomy and Astrophysics* **57**, 467 (2019), <https://doi.org/10.1146/annurev-astro-081817-051948>.
- [92] M. Cerruti, *Galaxies* **8** (2020), 10.3390/galaxies8040072.
- [93] A. Neronov, D. V. Semikoz, and K. Ptitsyna, *Astron. Astrophys.* **603**, A135 (2017), [arXiv:1611.06338](https://arxiv.org/abs/1611.06338) [astro-ph.HE].
- [94] A. Zech, M. Cerruti, and D. Mazin, *Astronomy & Astrophysics* **602**, A25 (2017).
- [95] C. M. Raiteri and M. Villata (WEBT), *Nature* **552**, 374 (2017), [arXiv:1712.02098](https://arxiv.org/abs/1712.02098) [astro-ph.HE].
- [96] D. Bhattacharya, R. Misra, A. R. Rao, and P. Sreekumar, *Mon. Not. Roy. Astron. Soc.* **431**, 1618 (2013), [arXiv:1303.6160](https://arxiv.org/abs/1303.6160) [astro-ph.CO].
- [97] M. G. Aartsen *et al.* (IceCube), *Science* **361**, 147 (2018), [arXiv:1807.08794](https://arxiv.org/abs/1807.08794) [astro-ph.HE].
- [98] A. Keivani *et al.*, *Astrophys. J.* **864**, 84 (2018), [arXiv:1807.04537](https://arxiv.org/abs/1807.04537) [astro-ph.HE].
- [99] M. Cerruti, A. Zech, C. Boisson, G. Emery, S. Inoue, and J. P. Lenain, *Mon. Not. Roy. Astron. Soc.* **483**, L12 (2019), [Erratum: *Mon. Not. Roy. Astron. Soc.* **502**, L21–L22 (2021)], [arXiv:1807.04335](https://arxiv.org/abs/1807.04335) [astro-ph.HE].
- [100] R. Xue, R.-Y. Liu, M. Petropoulou, F. Oikonomou, Z.-R. Wang, K. Wang, and X.-Y. Wang, *The Astrophysical Journal* **886**, 23 (2019).
- [101] R. U. Abbasi *et al.* (Telescope Array), *Science* **382**, abo5095 (2023),

- [arXiv:2311.14231 \[astro-ph.HE\]](#) .
- [102] K. Murase, C. D. Dermer, H. Takami, and G. Migliori, *The Astrophysical Journal* **749**, 63 (2012).
- [103] M. W. Toomey, F. Oikonomou, and K. Murase, *Mon. Not. Roy. Astron. Soc.* **497**, 2455 (2020), [arXiv:2005.11581 \[astro-ph.HE\]](#) .
- [104] B. Carpenter and R. Ojha, *The Astronomer's Telegram* **7704**, 1 (2015).
- [105] S. Ciprini, *The Astronomer's Telegram* **11644**, 1 (2018).
- [106] I. Mereu, *The Astronomer's Telegram* **13599**, 1 (2020).
- [107] I. Mereu, *The Astronomer's Telegram* **13599**, 1 (2020).
- [108] F. Lucarelli, C. Pittori, F. Verrecchia, M. Tavani, M. Cardillo, C. Casentini, G. Piano, A. Ursi, A. Bulgarelli, V. Fioretti, N. Parmiggiani, A. Addis, L. Baroncelli, I. Donnarumma, S. Vercellone, F. Gianotti, M. Trifoglio, A. Giuliani, S. Mereghetti, P. Caraveo, F. Perotti, A. Chen, A. Argan, E. Costa, E. Del Monte, Y. Evangelista, M. Feroci, F. Lazzarotto, I. Lapshov, L. Pacciani, P. Soffitta, V. Vittorini, G. Di Cocco, F. Fuschino, M. Galli, C. Labanti, M. Marisaldi, A. Pellizzoni, M. Pilia, A. Trois, G. Barbiellini, E. Valazza, F. Longo, A. Morselli, P. Picozza, M. Prest, P. Lipari, D. Zanello, P. W. Cattaneo, A. Rappoldi, A. Ferrari, F. Paoletti, L. A. Antonelli, P. Giommi, L. Salotti, G. Valentini, and F. D'Amico, *The Astronomer's Telegram* **13602**, 1 (2020).
- [109] Z. Shah, V. Jithesh, S. Sahayanathan, and N. Iqbal, *Mon. Not. Roy. Astron. Soc.* **504**, 416 (2021), [arXiv:2103.13657 \[astro-ph.HE\]](#) .
- [110] H.-N. He, A. Kusenko, S. Nagataki, B.-B. Zhang, R.-Z. Yang, and Y.-Z. Fan, *Physical Review D* **93**, 043011 (2016).
- [111] D. A. Luebke, *Conceptual Design Gamma-Ray Large Area Space Telescope (GLAST) Tower Structure [Thesis]*, Ph.D. thesis, Stanford University (1996).
- [112] R. Rando and S. Buson, *Nuovo Cimento Rivista Serie* **38**, 209 (2015).
- [113] W. B. Atwood *et al.* (Fermi-LAT), *Astrophys. J.* **697**, 1071 (2009), [arXiv:0902.1089 \[astro-ph.IM\]](#) .
- [114] L. collaboration *et al.*, [arXiv preprint arXiv:1902.10045](#) (2019).
- [115] NASA, "Fgst," (2018).
- [116] NASA, "Fermi-lat all-sky weekly files," (2019).
- [117] D. N. Burrows, J. E. Hill, J. A. Nousek, J. A. Kennea, A. Wells, J. P. Osborne, A. F. Abbey, A. Beardmore, K. Mukerjee, A. D. T. Short, G. Chincarini, S. Campana, O. Citterio, A. Moretti, C. Pagani, G. Tagliaferri, P. Giommi, M. Capalbi, F. Tamburelli, L. Angelini, G. Cusumano, H. W. Bräuninger, W. Burkert, and G. D. Hartner, *Space Science Reviews* **120**, 165 (2005), [arXiv:astro-ph/0508071 \[astro-ph\]](#) .
- [118] N. Gehrels, G. Chincarini, P. Giommi, K. Mason, J. Nousek, A. Wells, N. White, S. Barthelmy, D. N. Burrows, L. R. Cominsky, *et al.*, *The Astrophysical Journal* **611**, 1005 (2004).
- [119] S. D. Barthelmy, L. M. Barbier, J. R. Cummings, E. E. Fenimore, N. Gehrels, D. Hullinger, H. A. Krimm, C. B. Markwardt, D. M. Palmer, A. Parsons, *et al.*, *Space Science Reviews* **120**, 143 (2005).
- [120] Swift, "Swift xrtpipeline," (2023).
- [121] Swift, "Swift data analysis guide," (2011).
- [122] J. Ingham, K. A. Arnaud, and M. F. Corcoran, "The xselect user's guide," (2022).
- [123] NASA, "xrtmkarf," (2015).
- [124] R. Yusaf, "grppha," (1994).
- [125] I. M. George, "addspec," (1995).
- [126] I. M. George, "mathpha," (1999).
- [127] K. A. Arnaud, in *Astronomical Data Analysis Software and Systems V*, *Astronomical Society of the Pacific Conference Series*, Vol. 101, edited by G. H. Jacoby and J. Barnes (1996) p. 17.
- [128] Swift, "uvotsource," (2022).
- [129] K. Barbary, J. Lusk, and K. Boone, *extinction* (2016).
- [130] E. L. Fitzpatrick, *Publications of the Astronomical Society of the Pacific* **111**, 63 (1999), [arXiv:astro-ph/9809387 \[astro-ph\]](#) .
- [131] G. V. Schultz and W. Wiemer, *Astronomy and Astrophysics* **43**, 133 (1975).
- [132] G. H. Rieke and M. J. Lebofsky, *The Astrophysical Journal* **288**, 618 (1985).
- [133] D. C. B. Whittet and I. G. van Breda, *Monthly Notices of the Royal Astronomical Society* **192**, 467 (1980).
- [134] A. Breeveld, W. Landsman, S. Holland, P. Roming, N. Kuin, and M. Page, *AIP Conference Proceedings* **1358**, 373 (2011).
- [135] V. M. Larionov, M. Villata, C. M. Raiteri, S. G. Jorstad, A. P. Marscher, I. Agudo, P. S. Smith, J. A. Acosta-Pulido, M. J. Árévalo, A. A. Arkharov, R. Bachev, D. A. Blinov, G. Borisov, G. A. Borman, V. Bozhilov, A. Bueno, M. I. Carnerero, D. Carosati, C. Casadio, W. P. Chen, D. P. Clemens, A. Di Paola, S. A. Ehgambardiev, J. L. Gómez, P. A. González-

- Morales, A. Griñón-Marín, T. S. Grishina, V. A. Hagen-Thorn, S. Ibryamov, R. Itoh, M. Joshi, E. N. Kopatskaya, E. Koptelova, C. Lázaro, E. G. Larionova, L. V. Larionova, A. Manilla-Robles, Y. Metodieva, Y. V. Milanova, D. O. Mirzaqulov, S. N. Molina, D. A. Morozova, S. V. Nazarov, E. Ovcharov, S. Peneva, J. A. Ros, A. C. Sadun, S. S. Savchenko, E. Semkov, S. G. Sergeev, A. Strigachev, Y. V. Troitskaya, and I. S. Troitsky, *Monthly Notices of the Royal Astronomical Society* **461**, 3047 (2016), [arXiv:1606.07836 \[astro-ph.HE\]](https://arxiv.org/abs/1606.07836).
- [136] Swift, “*uvotimsum*,” (2023).
- [137] ESA, “*Sas data analysis thread*,”.
- [138] E. Lorenz and M. Martinez, *Astronomy and Geophysics* **46**, 6.21 (2005).
- [139] M. Doro, D. Bastieri, A. Biland, F. Dazzi, L. Font, M. Garczarczyk, M. Ghigo, E. Giro, F. Goebel, R. Kosyra, E. Lorenz, M. Mariotti, R. Mirzoyan, L. Peruzzo, G. Pareschi, and J. Zapatero, *Nuclear Instruments and Methods in Physics Research A* **595**, 200 (2008).
- [140] MOJAVE, “*Mojave*,”.
- [141] ATCA, “*Atca*,” (2021).
- [142] Lefaucheur, Julien and Pita, Santiago, *A&A* **602**, A86 (2017).
- [143] D. J. Thompson, S. Djorgovski, and R. de Carvalho, *Publications of the Astronomical Society of the Pacific* **102**, 1235 (1990).
- [144] A. L. Fey, R. Ojha, J. E. Reynolds, S. P. Ellingsen, P. M. McCulloch, D. L. Jauncey, and K. J. Johnston, *The Astronomical Journal* **128**, 2593 (2004).
- [145] G. L. White, M. J. Batty, J. D. Bunton, D. R. Brown, and J. B. Corben, *Monthly Notices of the Royal Astronomical Society* **227**, 705 (1987), <https://academic.oup.com/mnras/article-pdf/227/3/705/9404926/mnras227-0705.pdf>.
- [146] L. Collaboration, “Fermi large area telescope third source catalog,” (2015), [arXiv:1501.02003 \[astro-ph.HE\]](https://arxiv.org/abs/1501.02003).
- [147] S. Abdollahi, F. Acero, M. Ackermann, M. Ajello, W. B. Atwood, M. Axelsson, L. Baldini, J. Ballet, G. Barbiellini, D. Bastieri, J. B. Gonzalez, R. Bellazzini, A. Berretta, E. Bissaldi, R. D. Blandford, E. D. Bloom, R. Bonino, E. Bottacini, T. J. Brandt, J. Bregeon, P. Bruel, R. Buehler, T. H. Burnett, S. Buson, R. A. Cameron, R. Caputo, P. A. Caraveo, J. M. Casandjian, D. Castro, E. Cavazzuti, E. Charles, S. Chaty, S. Chen, C. C. Cheung, G. Chiaro, S. Ciprini, J. Cohen-Tanugi, L. R. Cominsky, J. Coronado-Blázquez, D. Costantin, A. Cuoco, S. Cuttini, F. D’Ammando, M. DeKlotz, P. de la Torre Luque, F. de Palma, A. Desai, S. W. Digel, N. D. Lalla, M. D. Mauro, L. D. Venere, A. Domínguez, D. Dumora, F. F. Dirirsa, S. J. Fegan, E. C. Ferrara, A. Franckowiak, Y. Fukazawa, S. Funk, P. Fusco, F. Gargano, D. Gasparrini, N. Giglietto, P. Giommi, F. Giordano, M. Giroletti, T. Glanzman, D. Green, I. A. Grenier, S. Griffin, M.-H. Grondin, J. E. Grove, S. Guiriec, A. K. Harding, K. Hayashi, E. Hays, J. W. Hewitt, D. Horan, G. Jóhannesson, T. J. Johnson, T. Kamae, M. Kerr, D. Kocevski, M. Kovac’evic’, M. Kuss, D. Landriu, S. Larsson, L. Latronico, M. Lemoine-Goumard, J. Li, I. Lioudakis, F. Longo, F. Loparco, B. Lott, M. N. Lovellette, P. Lubrano, G. M. Madejski, S. Maldera, D. Malyshev, A. Manfreda, E. J. Marchesini, L. Marcotulli, G. Martí-Devesa, P. Martin, F. Massaro, M. N. Mazziotta, J. E. McEnery, I. Mereu, M. Meyer, P. F. Michelson, N. Mirabal, T. Mizuno, M. E. Monzani, A. Morselli, I. V. Moskalenko, M. Negro, E. Nuss, R. Ojha, N. Omodei, M. Orienti, E. Orlando, J. F. Ormes, M. Palatiello, V. S. Paliya, D. Paneque, Z. Pei, H. Peña-Herazo, J. S. Perkins, M. Persic, M. Pesce-Rollins, V. Petrosian, L. Petrov, F. Piron, H. Poon, T. A. Porter, G. Principe, S. Rainò, R. Rando, M. Razzano, S. Razzaque, A. Reimer, O. Reimer, Q. Remy, T. Reposeur, R. W. Romani, P. M. S. Parkinson, F. K. Schinzel, D. Serini, C. Sgrò, E. J. Siskind, D. A. Smith, G. Spandre, P. Spinelli, A. W. Strong, D. J. Suson, H. Tajima, M. N. Takahashi, D. Tak, J. B. Thayer, D. J. Thompson, L. Tibaldo, D. F. Torres, E. Torresi, J. Valverde, B. V. Klavieren, P. van Zyl, K. Wood, M. Yassine, and G. Zaharijas, *The Astrophysical Journal Supplement Series* **247**, 33 (2020).
- [148] B. Carpenter and R. Ojha, *The Astronomer’s Telegram* **7704**, 1 (2015).
- [149] S. Ciprini, *The Astronomer’s Telegram* **11644**, 1 (2018).
- [150] F. Lucarelli, C. Pittori, F. Verrecchia, M. Tavani, M. Cardillo, C. Casentini, G. Piano, A. Ursi, A. Bulgarelli, V. Fioretti, N. Parmiggiani, A. Addis, L. Baroncelli, I. Donnarumma, S. Vercellone, F. Gianotti, M. Trifoglio, A. Giuliani, S. Mereghetti, P. Caraveo, F. Perotti, A. Chen, A. Argan, E. Costa, E. Del Monte, Y. Evangelista, M. Feroci, F. Lazzarotto,

- I. Lapshov, L. Pacciani, P. Soffitta, V. Vittorini, G. Di Cocco, F. Fuschino, M. Galli, C. Labanti, M. Marisaldi, A. Pellizzoni, M. Pilia, A. Trois, G. Barbiellini, E. Vallazza, F. Longo, A. Morselli, P. Picozza, M. Prest, P. Lipari, D. Zanella, P. W. Cattaneo, A. Rappoldi, A. Ferrari, F. Paoletti, L. A. Antonelli, P. Giommi, L. Salotti, G. Valentini, and F. D'Amico, *The Astronomer's Telegram* **13602**, 1 (2020).
- [151] S. Buson, *The Astronomer's Telegram* **13604**, 1 (2020).
- [152] S. J. Wagner, *The Astronomer's Telegram* **13632**, 1 (2020).
- [153] J. Stevens, P. G. Edwards, R. Ojha, and M. Kadler, *The Astronomer's Telegram* **13638**, 1 (2020).
- [154] K.-K. Duan, W. Jiang, F. Gargano, S.-J. Lei, X. Li, Y.-F. Liang, N.-H. Liao, M. N. Mazziotta, M. M. Salinas, Z.-Q. Shen, M. Su, Z.-L. Xu, Q. Yuan, Y.-Z. Fan, and J. Chang, *The Astronomer's Telegram* **13643**, 1 (2020).
- [155] FSSC, "Pks 0903-57 lc," (2024).
- [156] Fermi-LAT_Data_Server, "Fermi-LAT Collaboration," (2022).
- [157] FTools, "Fermi-LAT Collaboration," (2018).
- [158] P. Bruel, T. H. Burnett, S. W. Digel, G. Johannesson, N. Omodei, and M. Wood, "Fermi-lat improved pass 8 event selection," (2018), [arXiv:1810.11394](https://arxiv.org/abs/1810.11394) [astro-ph.IM].
- [159] Fermi, "Fermi-lat ciceron," (2018).
- [160] Fermi, "Fermi data preparation," (2022).
- [161] T. Johnson, "Fermi science tools spectral plots generator for lat sources," (2011).
- [162] K. A. Arnaud, in *Astronomical Data Analysis Software and Systems V*, Astronomical Society of the Pacific Conference Series, Vol. 101, edited by G. H. Jacoby and J. Barnes (1996) p. 17.
- [163] L. Angelini and E. J. Sabol, "n_H density calculator," .
- [164] E. L. Fitzpatrick, *Publications of the Astronomical Society of the Pacific* **111**, 63–75 (1999).
- [165] J. D. Scargle, J. P. Norris, B. Jackson, and J. Chiang, "The bayesian block algorithm," (2013), [arXiv:1304.2818](https://arxiv.org/abs/1304.2818) [astro-ph.IM].
- [166] A. A. Abdo, M. Ackermann, M. Ajello, E. Antolini, L. Baldini, J. Ballet, G. Barbiellini, D. Bastieri, K. Bechtol, R. Bellazzini, and et al., *The Astrophysical Journal* **722**, 520–542 (2010).
- [167] R. Prince, P. Majumdar, and N. Gupta, *The Astrophysical Journal* **844**, 62 (2017).
- [168] J. R. Mattox, D. L. Bertsch, J. Chiang, B. L. Dingus, S. W. Digel, J. A. Esposito, J. M. Fierro, R. C. Hartman, S. D. Hunter, G. Kanbach, D. A. Kniffen, Y. C. Lin, D. J. Macomb, H. A. Mayer-Hasselwander, P. F. Michelson, C. von Montigny, R. Mukherjee, P. L. Nolan, P. V. Ramanamurthy, E. Schneid, P. Sreekumar, D. J. Thompson, and T. D. Willis, *The Astrophysical Journal* **461**, 396 (1996).
- [169] R. J. Britto, E. Bottacini, B. Lott, S. Razzaque, and S. Buson, *The Astrophysical Journal* **830**, 162 (2016).
- [170] S. Das, N. Gupta, and S. Razzaque, *The Astrophysical Journal* **889**, 149 (2020).
- [171] J. Hahn, *PoS ICRC2015*, 917 (2016).
- [172] GAMERA, "GAMERA," (2016).
- [173] E. Massaro, M. Perri, P. Giommi, and R. Nesci, *Astronomy and Astrophysics* **413**, 489 (2004), [arXiv:astro-ph/0312260](https://arxiv.org/abs/astro-ph/0312260) [astro-ph].
- [174] G. R. BLUMENTHAL and R. J. GOULD, *Rev. Mod. Phys.* **42**, 237 (1970).
- [175] R. J. Protheroe, *Publications of the Astronomical Society of Australia* **19**, 486–498 (2002).
- [176] R. C. Gilmore, R. S. Somerville, J. R. Primack, and A. Domínguez, *Monthly Notices of the Royal Astronomical Society* **422**, 3189 (2012), <https://academic.oup.com/mnras/article-pdf/422/4/3189/18601416/mnras0422-3189.pdf>.
- [177] A. A. Abdo, M. Ackermann, M. Ajello, A. Allafort, L. Baldini, J. Ballet, G. Barbiellini, M. G. Baring, D. Bastieri, K. Bechtol, and et al., *The Astrophysical Journal* **727**, 129 (2011).
- [178] A. A. Abdo, M. Ackermann, M. Ajello, L. Baldini, J. Ballet, G. Barbiellini, D. Bastieri, K. Bechtol, R. Bellazzini, B. Berenji, and et al., *The Astrophysical Journal* **736**, 131 (2011).
- [179] M. Zacharias and S. J. Wagner, *Astronomy & Astrophysics* **588**, A110 (2016).
- [180] A. Shukla, K. Mannheim, S. R. Patel, J. Roy, V. R. Chitnis, D. Dorner, A. R. Rao, G. C. Anupama, and C. Wendel, *The Astrophysical Journal Letters* **854**, L26 (2018).
- [181] S. L. Mufson and D. J. Hutter, *Astrophysical Journal Letters* **248**, L61 (1981).
- [182] M. H. Ulrich, *Astrophysical Journal Letters* **222**, L3 (1978).
- [183] D. J. Hutter and S. L. Mufson, *The Astronomical Journal* **86**, 1585 (1981).
- [184] J. Albert, E. Aliu, H. Anderhub, P. Antoranz, A. Armada, M. Asensio, C. Baix-

- eras, J. A. Barrio, H. Bartko, D. Bastieri, J. Becker, W. Bednarek, K. Berger, C. Bigongiari, A. Biland, E. Bisesi, R. K. Bock, P. Bordas, V. Bosch-Ramon, T. Bretz, I. Britvitch, M. Camara, E. Carmona, A. Chilingarian, S. Ciprini, J. A. Coarasa, S. Commichau, J. L. Contreras, J. Cortina, V. Curtef, V. Danielyan, F. Dazzi, A. D. Angelis, R. de los Reyes, B. D. Lotto, E. Domingo-Santamaría, D. Dorner, M. Doro, M. Errando, M. Fagiolini, D. Ferenc, E. Fernández, R. Firpo, J. Flix, M. V. Fonseca, L. Font, M. Fuchs, N. Galante, M. Garczarczyk, M. Gaug, M. Giller, F. Goebel, D. Hakobyan, M. Hayashida, T. Hengstebeck, D. Höhne, J. Hose, C. C. Hsu, P. Jacon, O. Kalekin, R. Kosyra, D. Kranich, M. Laatiaoui, A. Laille, T. Lenisa, P. Liebing, E. Lindfors, S. Lombardi, F. Longo, J. López, M. López, E. Lorenz, P. Majumdar, G. Maneva, K. Mannheim, O. Mansutti, M. Mariotti, M. Martínez, D. Mazin, C. Merck, M. Meucci, M. Meyer, J. M. Miranda, R. Mirzoyan, S. Mizobuchi, A. Moralejo, K. Nilsson, J. Ninkovic, E. Oña-Wilhelmi, R. Orduña, N. Otte, I. Oya, D. Paneque, R. Paoletti, J. M. Paredes, M. Pasanen, D. Pascoli, F. Pauss, R. Pegna, M. Persic, L. Peruzzo, A. Piccioli, M. Poller, E. Prandini, A. Raymers, W. Rhode, M. Ribó, J. Rico, B. Riegel, M. Rissi, A. Robert, S. Rügamer, A. Saggion, A. Sánchez, P. Sartori, V. Scalzotto, V. Scapin, R. Schmitt, T. Schweizer, M. Shayduk, K. Shinozaki, S. N. Shore, N. Sidro, A. Sillanpää, D. Sobczynska, A. Stamerra, L. S. Stark, L. Takalo, P. Temnikov, D. Tesaro, M. Teshima, N. Tonello, A. Torres, D. F. Torres, N. Turini, H. Vankov, V. Vitale, R. M. Wagner, T. Wibig, W. Wittek, R. Zanin, and J. Zapatero, *The Astrophysical Journal* **648**, L105 (2006).
- [185] S. Rügamer, E. Angelakis, D. Bastieri, D. Dorner, Y. Y. Kovalev, A. Lähteenmäki, E. Lindfors, C. Pittori, R. Reinthal, K. V. Sokolovsky, A. Stamerra, and H. Ungerechts, “[Magic and multi-wavelength observations of three hbls in 2008,](#)” (2011).
- [186] S. Rügamer, E. Angelakis, D. Bastieri, D. Dorner, L. Fuhrmann, Y. A. Kovalev, Y. Y. Kovalev, A. Lähteenmäki, E. Lindfors, F. Longo, F. Lucarelli, C. Pittori, R. Reinthal, C. Sbarra, K. Sokolovsky, A. Stamerra, and H. Ungerechts, “[Magic and multi-wavelength observations of mrk 180 and 1es 2344+514 in 2008,](#)” (2011).
- [187] K. Nilsson *et al.*, *Astron. Astrophys.* **620**, A185 (2018), [arXiv:1810.01751 \[astro-ph.HE\]](#).
- [188] R. U. Abbasi *et al.* (Telescope Array), *Astrophys. J. Lett.* **790**, L21 (2014), [arXiv:1404.5890 \[astro-ph.HE\]](#).
- [189] K. Kawata, M. Fukushima, D. Ikeda, D. Ivanov, E. Kido, J. N. Matthews, S. Nagataki, T. Nonaka, T. Okuda, G. Rubtsov, H. Sagawa, N. Sakurai, B. T. Stokes, M. Takeda, R. Takeishi, A. Taketa, G. Thomson, P. Tinyakov, I. Tkachev, and H. Tokuno, in *34th International Cosmic Ray Conference (ICRC2015)*, International Cosmic Ray Conference, Vol. 34 (2015) p. 276.
- [190] K. Kawata, A. di Matteo, T. Fujii, D. Ikeda, D. Ivanov, C. C. H. Jui, E. Kido, J. P. Lundquist, J. N. Matthews, S. Nagataki, T. Nonaka, S. Ogio, T. Okuda, G. Rubtsov, H. Sagawa, T. K. Sako, N. Sakurai, M. Takeda, R. Takeishi, A. Taketa, G. B. Thomson, P. Tinyakov, I. Tkachev, S. Troitsky, and Telescope Array Collaboration, in *36th International Cosmic Ray Conference (ICRC2019)*, International Cosmic Ray Conference, Vol. 36 (2019) p. 310.
- [191] M. Wood, R. Caputo, E. Charles, M. Di Mauro, J. Magill, J. S. Perkins, and Fermi-LAT Collaboration, in *35th International Cosmic Ray Conference (ICRC2017)*, International Cosmic Ray Conference, Vol. 301 (2017) p. 824, [arXiv:1707.09551 \[astro-ph.IM\]](#).
- [192] J. Ballet, T. H. Burnett, S. W. Digel, and B. Lott, “[Fermi large area telescope fourth source catalog data release 2,](#)” (2020).
- [193] F. Acero, M. Ackermann, M. Ajello, A. Albert, L. Baldini, J. Ballet, G. Barbiellini, D. Bastieri, R. Bellazzini, E. Bissaldi, *et al.*, *The Astrophysical Journal Supplement Series* **223**, 26 (2016).
- [194] FermipyDocument, “[Fermipy,](#)” (2022).
- [195] HI4PI Collaboration, N. Ben Bekhti, L. Flöer, R. Keller, J. Kerp, D. Lenz, B. Winkel, J. Bailin, M. R. Calabretta, L. Dedes, H. A. Ford, B. K. Gibson, U. Haud, S. Janowiecki, P. M. W. Kalberla, F. J. Lockman, N. M. McClure-Griffiths, T. Murphy, H. Nakanishi, D. J. Pisano, and L. Staveley-Smith, *Astronomy and Astrophysics* **594**, A116 (2016), [arXiv:1610.06175 \[astro-ph.GA\]](#).
- [196] G. V. Schultz and W. Wiemer, *Astronomy and Astrophysics* **43**, 133 (1975).
- [197] G. H. Rieke and M. J. Lebofsky, *The Astro-*

- physical Journal *Physical Review D* **288**, 618 (1985).
- [198] D. C. B. Whittet and I. G. van Breda, *Monthly Notices of the Royal Astronomical Society* **192**, 467 (1980).
- [199] ESA, “Xmm-newton science archive,” (2024).
- [200] omichain, “omichain,” (2018).
- [201] om2pha, “om2pha,” (2016).
- [202] OMResponseFile, “OMResponseFile,” (2008).
- [203] MOJAVE_Source_Page, “MOJAVE Source Page,” (2016).
- [204] J. Albert, E. Aliu, H. Anderhub, P. Antoranz, A. Armada, M. Asensio, C. Baixeras, J. A. Barrio, H. Bartko, D. Bastieri, J. Becker, W. Bednarek, K. Berger, C. Bigongiari, A. Biland, E. Bisesi, R. K. Bock, P. Bordas, V. Bosch-Ramon, T. Bretz, I. Britvitch, M. Camara, E. Carmona, A. Chilingarian, S. Ciprini, J. A. Coarasa, S. Commichau, J. L. Contreras, J. Cortina, V. Curtef, V. Danielyan, F. Dazzi, A. De Angelis, R. de los Reyes, B. De Lotto, E. Domingo-Santamaría, D. Dorner, M. Doro, M. Errando, M. Fagiolini, D. Ferenc, E. Fernández, R. Firpo, J. Flix, M. V. Fonseca, L. Font, M. Fuchs, N. Galante, M. Garczarczyk, M. Gaug, M. Giller, F. Goebel, D. Hakobyan, M. Hayashida, T. Hengstebeck, D. Höhne, J. Hose, C. C. Hsu, P. Jacon, O. Kalekin, R. Kosyra, D. Kranich, M. Laatiaoui, A. Laille, T. Lenisa, P. Liebing, E. Lindfors, S. Lombardi, F. Longo, J. López, M. López, E. Lorenz, P. Majumdar, G. Maneva, K. Mannheim, O. Mansutti, M. Mariotti, M. Martínez, D. Mazin, C. Merck, M. Meucci, M. Meyer, J. M. Miranda, R. Mirzoyan, S. Mizobuchi, A. Moralejo, K. Nilsson, J. Ninkovic, E. Oña-Wilhelmi, R. Orduña, N. Otte, I. Oya, D. Paneque, R. Paoletti, J. M. Paredes, M. Pasanen, D. Pascoli, F. Paus, R. Pegna, M. Persic, L. Peruzzo, A. Piccioli, M. Poller, E. Prandini, A. Raymers, W. Rhode, M. Ribó, J. Rico, B. Riegel, M. Rissi, A. Robert, S. Rügamer, A. Saggion, A. Sánchez, P. Sartori, V. Scalzotto, V. Scapin, R. Schmitt, T. Schweizer, M. Shayduk, K. Shinozaki, S. N. Shore, N. Sidro, A. Sillanpää, D. Sobczynska, A. Stamerra, L. S. Stark, L. Takalo, P. Temnikov, D. Tescaro, M. Teshima, N. Tonello, A. Torres, D. F. Torres, N. Turini, H. Vankov, V. Vitale, R. M. Wagner, T. Wibig, W. Wittek, R. Zanin, and J. Zapatero, *Astrophysical Journal Letters* **648**, L105 (2006), arXiv:astro-ph/0606630 [astro-ph].
- [205] MAGICDataCentre, “MAGIC,” (2006).
- [206] I. S. A. SSCD, “SSDC,” (2000).
- [207] W. Essey and A. Kusenko, *Astroparticle Physics* **33**, 81 (2010), arXiv:0905.1162 [astro-ph.HE].
- [208] W. Essey, O. E. Kalashev, A. Kusenko, and J. F. Beacom, *Phys. Rev. Lett.* **104**, 141102 (2010).
- [209] E. Massaro, M. Perri, P. Giommi, and R. Nesci, *Astron. Astrophys.* **413**, 489 (2004), arXiv:astro-ph/0312260.
- [210] R. C. Gilmore, R. S. Somerville, J. R. Primack, and A. Dominguez, *Mon. Not. Roy. Astron. Soc.* **422**, 3189 (2012), arXiv:1104.0671 [astro-ph.CO].
- [211] R. J. Protheroe and P. L. Biermann, *Astropart. Phys.* **6**, 45 (1996), [Erratum: *Astropart. Phys.* **7**, 181 (1997)], arXiv:astro-ph/9605119.
- [212] R. Alves Batista, A. Dundovic, M. Erdmann, K.-H. Kampert, D. Kuempel, G. Müller, G. Sigl, A. van Vliet, D. Walz, and T. Winchen, *JCAP* **05**, 038 (2016), arXiv:1603.07142 [astro-ph.IM].
- [213] R. Alves Batista *et al.*, *JCAP* **09**, 035 (2022), arXiv:2208.00107 [astro-ph.HE].
- [214] C. Heiter, D. Kuempel, D. Walz, and M. Erdmann, *Astroparticle Physics* **102**, 39 (2018), arXiv:1710.11406 [astro-ph.IM].
- [215] E. Kafexhiu, F. Aharonian, A. M. Taylor, and G. S. Vila, *Physical Review D* **90**, 123014 (2014), arXiv:1406.7369 [astro-ph.HE].
- [216] T. Sjöstrand, S. Mrenna, and P. Skands, *Computer Physics Communications* **178**, 852 (2008).
- [217] P. Banik and A. Bhadra, *Phys. Rev. D* **99**, 103006 (2019).
- [218] P. Banik, A. Bhadra, M. Pandey, and D. Majumdar, *Phys. Rev. D* **101**, 063024 (2020).
- [219] R. Xue, Z.-R. Wang, and W.-J. Li, *Physical Review D* **106**, 103021 (2022), arXiv:2210.09797 [astro-ph.HE].
- [220] A. Treves, N. Carangelo, R. Falomo, and J. Kotilainen, in *Active Galactic Nuclei: From Central Engine to Host Galaxy*, Astronomical Society of the Pacific Conference Series, Vol. 290, edited by S. Collin, F. Combes, and I. Shlosman (2003) p. 621, arXiv:astro-ph/0211045 [astro-ph].
- [221] R. Falomo, J. Kotilainen, and A. Treves, in *The Mass of Galaxies at Low and High Redshift*, edited by R. Bender and A. Renzini (2003) p. 109, arXiv:astro-ph/0112423

- [astro-ph].
- [222] J. D. Finke, *The Astrophysical Journal* **870**, 28 (2019).
- [223] F. Aharonian, *New Astronomy* **5**, 377 (2000).
- [224] R. Jansson and G. R. Farrar, *Astrophys. J.* **757**, 14 (2012), arXiv:1204.3662 [astro-ph.GA].
- [225] H.-N. He, A. Kusenko, S. Nagataki, B.-B. Zhang, R.-Z. Yang, and Y.-Z. Fan, *Phys. Rev. D* **93**, 043011 (2016), arXiv:1411.5273 [astro-ph.HE].
- [226] R. Alves Batista *et al.*, *JCAP* **09**, 035 (2022), arXiv:2208.00107 [astro-ph.HE].
- [227] S. Aerdker *et al.*, *PoS ICRC2023*, 1471 (2023), arXiv:2308.09532 [astro-ph.HE].
- [228] W. B. Atwood *et al.* (Fermi-LAT), *The Astrophysical Journal* **697**, 1071 (2009), arXiv:0902.1089 [astro-ph.IM].
- [229] T. C. Weekes *et al.*, *Astropart. Phys.* **17**, 221 (2002), arXiv:astro-ph/0108478.
- [230] A. J. Smith (HAWC), *J. Phys. Conf. Ser.* **60**, 131 (2007).
- [231] B. L. Dingus and H. Collaboration, *AIP Conference Proceedings* **921**, 438 (2007), https://pubs.aip.org/aip/acp/article-pdf/921/1/438/11818639/438_1_online.pdf.
- [232] G. Di Sciascio (LHAASO), *Nucl. Part. Phys. Proc.* **279-281**, 166 (2016), arXiv:1602.07600 [astro-ph.HE].
- [233] M. Actis *et al.* (CTA Consortium), *Exper. Astron.* **32**, 193 (2011), arXiv:1008.3703 [astro-ph.IM].
- [234] G. Lucchetta, M. Ackermann, D. Berge, and R. Bühler, *Journal of Cosmology and Astroparticle Physics* **2022**, 013 (2022).
- [235] G.-y. Huang, S. Jana, M. Lindner, and W. Rodejohann, *JCAP* **02**, 038 (2022), arXiv:2112.09476 [hep-ph].
- [236] J. Ballet, P. Bruel, T. H. Burnett, and B. Lott (Fermi-LAT), arXiv preprint arXiv:2307.12546 (2023), arXiv:2307.12546 [astro-ph.HE].
- [237] M. W. E. Smith *et al.*, *Astropart. Phys.* **45**, 56 (2013), arXiv:1211.5602 [astro-ph.HE].
- [238] H. A. Ayala Solares, S. Coutu, D. Cowen, J. J. DeLaunay, D. B. Fox, A. Keivani, M. Mostafá, K. Murase, F. Oikonomou, M. Seglar-Arroyo, G. Tešić, and C. F. Turley, *Astroparticle Physics* **114**, 68 (2020).
- [239] M. G. Aartsen *et al.* (IceCube), *Science* **361**, 147 (2018), arXiv:1807.08794 [astro-ph.HE].
- [240] M. G. Aartsen *et al.* (IceCube, Fermi-LAT, MAGIC, AGILE, ASAS-SN, HAWC, H.E.S.S., INTEGRAL, Kanata, Kiso, Kapteyn, Liverpool Telescope, Subaru, Swift NuSTAR, VERITAS, VLA/17B-403), *Science* **361**, eaat1378 (2018), arXiv:1807.08816 [astro-ph.HE].
- [241] A. Acharyya *et al.* (VERITAS, H.E.S.S.), *Astrophys. J.* **954**, 70 (2023), arXiv:2306.17819 [astro-ph.HE].
- [242] S. Garrappa, S. Buson, and D. Gasparini, *The Astronomer's Telegram* **12972**, 1 (2019).
- [243] A. Franckowiak, S. Garrappa, V. Paliya, B. Shappee, R. Stein, N. Strotjohann, M. Kowalski, S. Buson, S. Kiehlmann, W. Max-Moerbeck, *et al.*, *The Astrophysical Journal* **893**, 162 (2020).
- [244] X. Rodrigues, S. Garrappa, S. Gao, V. S. Paliya, A. Franckowiak, and W. Winter, *The Astrophysical Journal* **912**, 54 (2021).
- [245] F. Oikonomou, M. Petropoulou, K. Murase, A. Tohuvavohu, G. Vasilopoulos, S. Buson, and M. Santander, *Journal of Cosmology and Astroparticle Physics* **2021**, 082 (2021).
- [246] S. Paiano, R. Falomo, A. Treves, P. Padovani, P. Giommi, A. Gargiulo, and A. Rossi, *The Astronomer's Telegram* **13457**, 1 (2020).
- [247] P. Giommi, P. Padovani, F. Oikonomou, T. Glauch, S. Paiano, and E. Resconi, *Astron. Astrophys.* **640**, L4 (2020), arXiv:2003.06405 [astro-ph.HE].
- [248] M. G. Aartsen *et al.* (IceCube), *Phys. Rev. Lett.* **124**, 051103 (2020), arXiv:1910.08488 [astro-ph.HE].
- [249] K. Murase, C. D. Dermer, H. Takami, and G. Migliori, *Astrophys. J.* **749**, 63 (2012), arXiv:1107.5576 [astro-ph.HE].
- [250] E. Resconi, S. Coenders, P. Padovani, P. Giommi, and L. Caccianiga, *Mon. Not. Roy. Astron. Soc.* **468**, 597 (2017), arXiv:1611.06022 [astro-ph.HE].
- [251] P. G. Tinyakov and I. I. Tkachev, *Nucl. Phys. B Proc. Suppl.* **110**, 501 (2002).
- [252] M. G. Aartsen *et al.* (IceCube), arXiv preprint arXiv:1412.5106 (2014), arXiv:1412.5106 [astro-ph.HE].
- [253] D. F. G. Fiorillo, M. Bustamante, and V. B. Valera, *JCAP* **03**, 026 (2023), arXiv:2205.15985 [astro-ph.HE].
- [254] J. A. Aguilar *et al.* (RNO-G), *JINST* **16**, P03025 (2021), [Erratum: *JINST* **18**, E03001 (2023)], arXiv:2010.12279 [astro-ph.IM].
- [255] K. Fang *et al.*, *PoS ICRC2017*, 996 (2018), arXiv:1708.05128 [astro-ph.IM].